LMU LUDWIG-MAXIMILIANS-UNIVERSITÄT MÜNCHEN

Structure, Fluidity and Phase Behavior of Supported Lipid Membranes: An Investigation by X-ray Reflectivity and Fluorescence Microscopy

Christian Reich

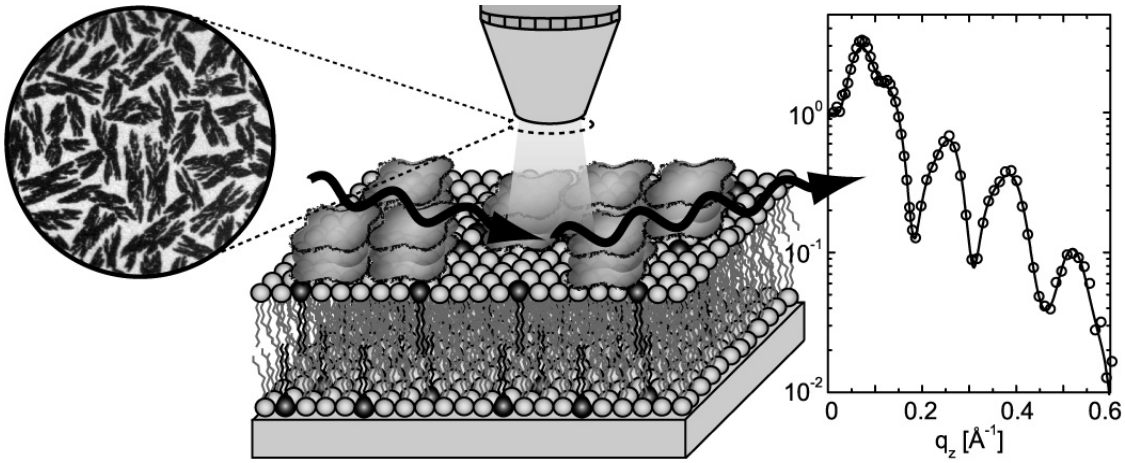

Department für Physik
Ludwig-Maximilians-Universität

München, Mai 2007

LMU LUDWIG-MAXIMILIANS-UNIVERSITÄT MÜNCHEN

Structure, Fluidity and Phase Behavior of Supported Lipid Membranes: An Investigation by X-ray Reflectivity and Fluorescence Microscopy

---

Dissertation

der Fakultät für Physik

der Ludwig-Maximilians-Universität

vorgelegt von

Christian Reich

aus Kronstadt in Siebenbürgen / Rumänien

München, 29. Mai 2007

ERSTGUTACHTER: PROF. DR. JOACHIM O. RÄDLER

ZWEITGUTACHTER: PROF. DR. THOMAS BEIN

TAG DER MÜNDLICHEN PRÜFUNG: 31. JULI 2007

Contents

Zusammenfassung

Die Zellmembranen von Säugetieren haben eine hochgradig heterogene Struktur und bestehen aus einer Vielzahl von Lipidmolekülen und Proteinen, die in der zellulären Lipiddoppelschicht angeordnet sind. Ein Verständnis von Membranprozessen, wie z.B. Lipid-Protein Wechselwirkungen, erfordert einen Einblick in die molekulare Struktur der Zellmembran. Solche Ångstrøm-Auflösung wird ermöglicht durch Röntgenstreutechniken, die auf die Elektronendichteverteilung in Makromolekülen sensitiv sind. Modell-Lipidmembranen imitieren die Zusammensetzung von natürlichen Zellmembranen und werden für Forschungszwecke benutzt. Eine besondere Klasse von biomimetischen Lipidmembranen sind substratgestützte Lipiddoppelschichten, die mit oberflächensensitiver Röntgenreflektivität studiert werden können. Hochgradig brilliante Röntgenstrahlen von modernen Synchrotronquellen ermöglichen detaillierte Strukturuntersuchungen auf Ångstrøm-Skala von Lipiddoppelschichten an fest-flüssig Grenzflächen.
Für diese Doktorarbeit wurde ein neuartiger Aufbau zur Studie von einzelnen biomimetischen Lipidmembranen an fest-flüssig Grenzflächen anhand von Reflektivität mit Röntgenstrahlen entwickelt. Der Aufbau ist ausserdem für quantitative Fluoreszenzmikroskopie ausgerichtet und erlaubt es, die Strukturforschungen mit Mikroskopiestudien zur Lipiddynamik in der Lipiddoppelschicht zu komplettieren. Dieses Konzept wendet zwei experimentelle Charakterisierungstechniquen auf eine einzelne Probe an und erlaubt einen ganzheitlichen Blick auf die biophysikalischen Eigenschaften von biomimetischen Lipidmembranen, wie molekulare Struktur, Lipidfluidität und Phasenzustand der Lipiddoppelschicht.
Zunächst wurden Lipiddoppelschichten auf verschiedenen Substraten charakterisiert, um die Eignung solcher Membran-Grenzflächen-Systeme für biologische und biotechnologische Anwendungen bewerten zu können. Die Oberflächenchemie eines zugrundeliegenden Substrats kann die strukturellen und dynamischen Eigenschaften einer Lipidmembran beträchtlich beeinflussen. Die Materialeigenschaften des thermoplastischen Kunststoffs 2-norbornene ethylene (Topas), wie optische Transparenz, hohe chemische Beständigkeit und Möglichkeiten für laterale Strukturierung, machen diese Verbindung zu einem interessanten Substrat für Lipidmembranen. Lipiddoppelschichten auf Topas zeigten eine hohe Homogenität, aber auch eine reduzierte Lipidfluidität ($\sim$50 %) im Vergleich zu Lipiddoppelschichten auf hydrophilem Siliziumoxid. Auf Topas wurde eine um 20 % reduzierte Doppelschichtdicke gemessen, welche auf eine Doppelschichtkonformation mit entweder aufgewickelten oder ineinander verflochtenen Alkylketten zurückgeführt werden kann. Eine weitere Vorlage für biosensorische Anwendungen sind Multischichten aus Polyelektrolyten, welche als Dielektrikum zwischen Lipidmembranen und Halbleitersubstraten fungieren können, wie z.B. silicon-on-insulator Baugruppen (SOI). Homogene Lipiddoppelschichten auf alternierenden Polyanion- und Polykation Schichten wurden untersucht und die Welligkeit der Doppelschicht in

Abhängigkeit von der Anzahl der unterliegenden Polyelektrolytschichten charakterisiert.
Des weiteren wurde untersucht wie membrangebundene Proteine und Rezeptormoleküle die Membranstruktur und Lipidfluidität beeinflussen. Die Bindung des Proteins Streptavidin an Biotinmoleküle hat eine starke nichtkovalente Affinität und wird weitreichend in biotechnologischer Forschung angewendet. Die Bildung einer Streptavidin/Avidin Schicht auf einer substratgestützten Lipiddoppelschicht mit biotinylierten Lipiden wurde charakterisiert. Eine wohldefinierte Wasserschicht von 8 Å konnte aufgelöst werden, welche das Protein von der Lipiddoppelschicht separiert; des weiteren wurde kein Einfluss des Proteins auf die Doppelschichtstruktur beobachtet. Die Lipidfluidität wurde anhand kontinuierlichen Bleichens vor und nach der Proteinbindung quantifiziert und eine kleine Minderung der Lipiddiffusionskonstante um 10-15 % nach der Proteinbindung wurde beobachtet. Die separierende Wasserschicht ermöglicht es offenbar der Lipiddoppelschicht ihre laterale Fluidität und strukturelle Integrität zu bewahren.
Zum Abschluss wurden biomimetische Membranen mit komplexen Mixturen untersucht, welche näherungsweise mit der Lipidkomposition von Zellmembranen in Säugetieren übereinstimmen. Bei diesen Lipidmembranen mit vielfachen Komponenten einschliesslich Cholesterin können sich kondensierte und nicht-kondensierte Lipidphasen auftrennen. Kondensierte Lipiddomänen haben eine höhere Ordnung als ihre Umgebung und lokalisieren Membranrezeptoren. Der Membranrezeptor G_{M1} ganglioside wurde in substratgestützten Lipiddoppelschichten mit Cholesterin und ternärer Komposition untersucht; es wurde Membrankondensation beobachtet die durch die Präsenz des Rezeptors ausgelöst wurde. Anhand der hohen strukturellen Auflösung von Synchrotronreflektivität wurde bestimmt, dass diese rezeptorinduzierte Kondensation asymmetrisch sein kann und auf die Lipideinzelschicht beschränkt ist, in welcher G_{M1} anwesend ist. Die Membranfluidität wurde durch die Präsenz von G_{M1} signifikant reduziert ($\sim$50 %) und laterale Segregation in mikroskopische Domänen ($\sim$5 μm) wurde mit Fluoreszenzmikroskopie beobachtet.

In dieser Doktorarbeit wurden komplementäre experimentelle Methoden angewendet um die Struktur von biomimetischen Lipidmembranen auf Ångstrøm-Skala und ihre Diffusionseigenschaften zu untersuchen. Systematische Studien wurden durchgeführt um den Einfluss von der Substratchemie, lipidgebundenen Makromolekülen und der Lipidanordnung auf die Struktur und die Fluidität von Lipiddoppelschichten zu erfassen und zu quantifizieren. Der vorliegende Mikrofluidikaufbau kann verwendet werden um andere komplexe Lipidmembransysteme zu untersuchen, mit dem Ziel unser physikalisches Verständnis von der Lipidmembran-Grenzfläche zu verbessern.

Summary

The structure of mammalian cell membranes is highly heterogeneous and consists of numerous lipid and protein molecules, which are organized into the cellular lipid bilayer. Understanding membrane processes such as lipid-protein interactions requires an insight into the molecular structure of the cell membrane. Such ångstrøm resolution is offered by X-ray diffraction techniques, which are sensitive to the electron density distribution within macromolecules. Model lipid membranes mimic the composition of natural cell membranes and are used for facilitating experimental investigations. A special class of biomimetic lipid membranes are substrate supported lipid bilayers, which can be studied by surface sensitive methods such as X-ray reflectivity. Using highly brilliant X-rays at modern synchrotron sources allows to obtain detailed structural information on lipid bilayers at solid-liquid interfaces.

For this thesis, a novel microfluidic setup for high resolution X-ray reflectivity studies of single biomimetic lipid membranes at solid-liquid interfaces was developed. The setup is also designed for quantitative fluorescence microscopy, which allows us to complement our structural studies with investigations on lipid dynamics within the lipid bilayer. Our approach unifies two experimental characterization techniques on a single sample and offers an integrated view on the biophysical properties of biomimetic lipid membranes, such as molecular structure, lipid fluidity and phase state of the lipid bilayer.

We have characterized lipid bilayers on different solid supports to assess the suitability of these membrane/interface systems for biological and biotechnological applications. The surface chemistry of an underlying substrate may considerably influence the structural and dynamical properties of a lipid membrane. The material properties of the thermoplastic polymer 2-norbornene ethylene (Topas), such as optical transparency, high chemical resistivity and ease for lateral structuring, make this compound an interesting candidate as a substrate for lipid membranes. Model lipid bilayers on Topas showed a high homogeneity, though a reduced lipid fluidity ($\sim$50 %) as compared to lipid bilayers supported on hydrophilic silicon oxide. We also observed on Topas a reduced bilayer thickness of about 20 %, which we ascribe to a bilayer conformation with either coiled or interdigitated acyl chains. Another template for biosensoric applications are polyelectrolyte multilayers, which can act as a dielectric between lipid bilayers and semiconductor substrates, such as silicon-on-insulator devices (SOI). We studied homogeneous lipid bilayers on alternating polyanion/polycation layers and characterized the corrugation of the bilayer depending on the number of underlying polyelectrolyte layers.

Further, we studied how protein and receptor molecules bound to lipid membranes influence their structure and lipid fluidity. The binding of the protein streptavidin to biotin molecules has a strong noncovalent affinity and is widely used in biotechnological research. We characterized the formation of a streptavidin/avidin layer

bound to a supported lipid bilayer containing biotinylated lipids. We resolved a well-defined water layer of 8 Å separating the protein and lipid bilayer and showed that the bilayer structure was not affected by the presence of the protein. The lipid fluidity was quantified using continuous bleaching before and after protein binding and we observed a small reduction of 10-15 % of the lipid diffusion constant after protein binding. We propose that the separating water layer allows the lipid bilayer to retain its lateral fluidity and structural integrity.
Finally, we studied biomimetic membranes with complex mixtures that approximate the lipid composition in mammalian cell membranes. Such lipid membranes with multiple components including cholesterol are capable of phase separation into condensed and non-condensed lipid phases. Condensed lipid domains are more ordered than their environment and localize membrane receptors. We studied the membrane receptor G_{M1} ganglioside in supported lipid bilayers of ternary compositions including cholesterol and observed membrane condensation, which was induced by the presence of the receptor. Using the high structural resolution available with synchrotron reflectivity, we determined that this receptor-induced condensation can be asymmetric and is restricted to the bilayer leaflet in which G_{M1} is present. The membrane fluidity was significantly reduced ($\sim$50 %) by the presence of G_{M1} and we observed lateral segregation into microscopic domains ($\sim$5 μm) with fluorescence microscopy.

In this thesis, complementary experimental techniques were applied to investigate the ångstrøm scale structure and diffusion properties of biomimetic lipid membranes. We systematically studied how substrate chemistry, lipid-bound macromolecules and lipid ordering influence the structure and fluidity of lipid bilayers. The present microfluidic setup can be used to study other complex lipid membrane systems to improve our physical understanding of lipid membrane interfaces.

Chapter 1

Introduction

The plasma membrane of mammalian cells is a heterogeneous and structurally asymmetric lipid bilayer, wherein a variety of proteins are embedded. These molecules are free to diffuse laterally, but remain confined to a two dimensional lipid matrix surrounded by an aqueous environment (Fig. 1.1). This concept was originally established as the 'fluid mosaic model' [6] and is being continuously revised, as molecular interactions confer structural heterogeneity to the membranes, and lipids and proteins can self-organize to form functional domains. These domains alter the physical and biochemical properties of the lipid bilayer and influence the diffusion of molecules [7]. Understanding biological processes at the cell membrane interface, such as protein binding and receptor localization into membrane domains, requires a molecular insight into the membrane structure. The complex architecture of cell membranes often complicates a direct investigation using cells and well-defined and isolated model lipid membranes are necessary for systematic experimental studies. Such biomimetic model lipid bilayers can be engineered with multiple components and lipid asymmetry across the leaflets, mimicking the structure and function of cell membranes. Solid supported lipid bilayers are a special class of biomimetic lipid membranes [9] and allow for the application of surface sensitive techniques, such as atomic force microscopy [10, 11], fluorescence microscopy [12, 13], and X-ray and neutron reflectivity at solid-liquid interfaces [14–16]. The best resolution can be obtained with X-ray diffraction, which is sensitive to the electron density distribution within biomolecules. Modern synchrotron sources provide highly brilliant X-rays which give access to detailed electron density profiles of lipid bilayers with an accuracy of several ångstrøm.

The key motivation for this thesis was to develop a better understanding of lipid-lipid, lipid-protein, and lipid-substrate interactions in single supported lipid bilayers, using high resolution X-ray reflectivity and fluorescence microscopy (Fig. 1.2). Single lipid bilayers are more representative model systems for cell membranes than multilamellar bilayers or lipid monolayers, since surface protein binding and molecular asymmetry across separate bilayer leaflets can be studied. A major challenge

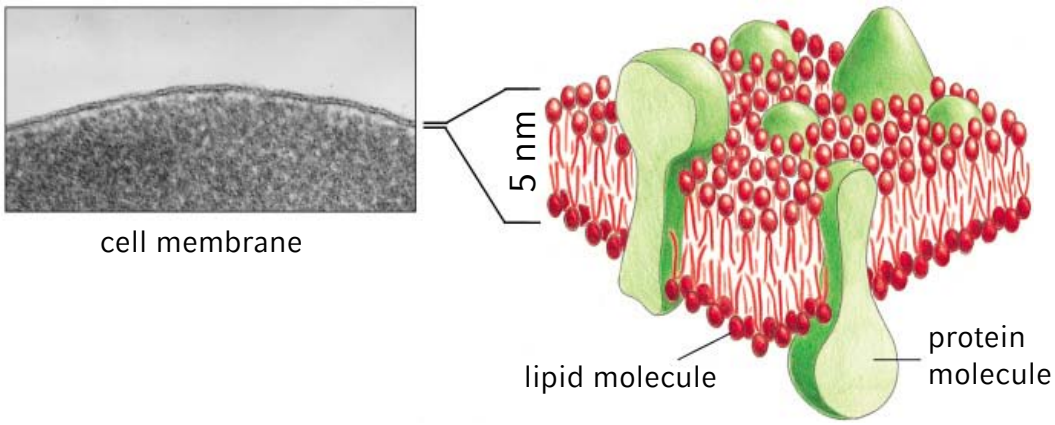

Figure 1.1: Fluid mosaic model of a cell membrane. The membrane is composed of a lipid bilayer and numerous macromolecules, which are embedded in the bilayer either as transmembrane proteins or attached peripherally to the membrane surface. The drawing is adapted from Ref. [8].

is to overcome the limitations of X-ray reflectivity at solid-liquid interfaces, such as background scattering and radiation damage, and to provide sufficient electron density contrast from the interface to precisely resolve molecular structures within the bilayer. Fluorescence microscopy is a standard technique for quantifying molecular diffusion in the lipid bilayer, which is an important parameter for characterizing the phase state of the membrane and thereby complements our structural X-ray studies.

The interaction of a lipid bilayer with the supporting substrate affects its biophysical properties, and an ideal support should allow the model membrane to retain its integrity and lateral lipid fluidity as found in free lipid bilayers. The choice of substrate has technological implications: Lipid bilayers on substrates with defined surface chemistry and dielectric properties allow for possible applications as biosensor templates. Understanding lipid-substrate interactions may also be important for understanding cell membranes; for example, the plasma membranes of mammalian cells are anchored to the cytoskeleton backbone, which has implications on the phase behavior in cell membranes [17].
The phase state of a lipid bilayer is mainly determined by the length and degree of saturation of the lipid acyl chains [18]. In mammalian cell membranes, attractive interactions between cholesterol and lipids with saturated acyl chains can form cholesterol-enriched lipid domains, which represent a liquid-ordered phase [19–21]. This phase is characterized by a tight lipid packing and a reduced lipid fluidity as compared to the surrounding cholesterol-depleted liquid-disordered phase, which contains mainly unsaturated lipids [22]. Membrane-associated receptors can preferentially localize into specific lipid phases, thereby targeting their ligands to certain functional regions in the membrane [23]. The binding of protein ligands to their

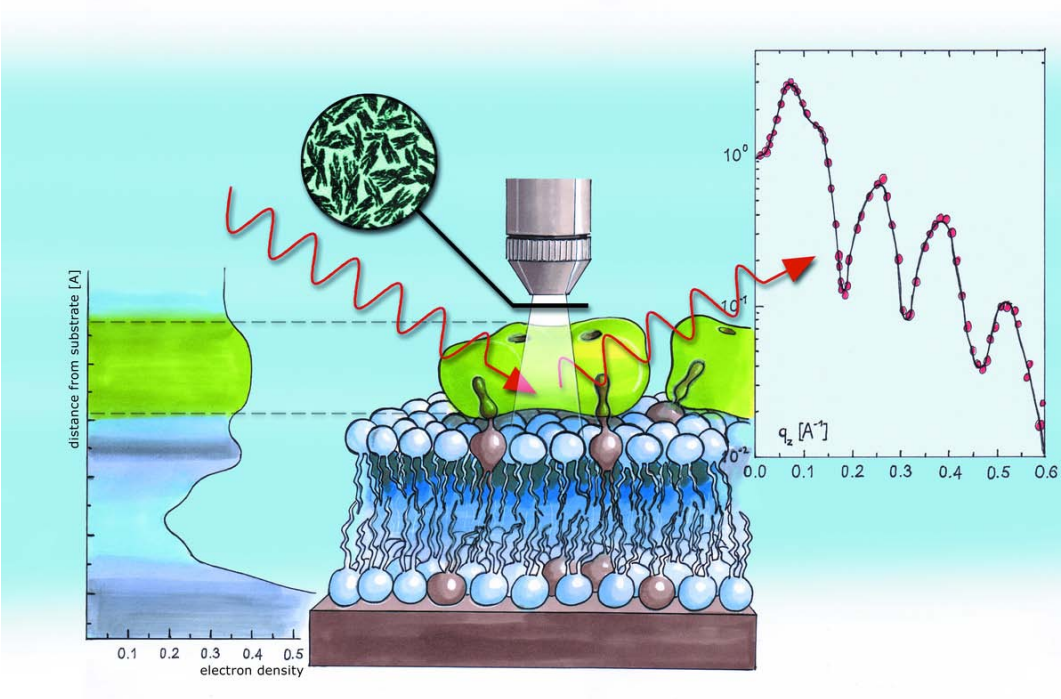

Figure 1.2: Schematic of a supported lipid bilayer with proteins bound to receptor lipids embedded within the membrane. The molecular structure is resolved by the electron density profile obtained with X-ray reflectivity. Lateral structures and diffusion of lipids and protein molecules at the membrane surface are assessed by fluorescence microscopy. The illustration was created by Patrick Bober.

receptors in the cellular membrane can locally rearrange the lipid environment and thereby modify the lipid bilayer structure and fluidity [24].

In order to systematically investigate these different molecular interactions in single model membranes, an experimental setup for X-ray reflectivity and fluorescence microscopy studies was designed as a part of this thesis. We combine the complementary results from these experimental techniques to obtain a comprehensive understanding of specific molecular processes in model lipid membranes.
This thesis is organized as follows: The microfluidic X-ray chamber is introduced in chapter 2, together with a brief description of the synchrotron and fluorescence microscopy measurements, and methods for membrane preparation. In chapter 3, we report our studies of supported lipid bilayers on the thermoplastic polymer 2-norbornene ethylene (Topas) and on a polyelectrolyte system composed of alternating polyanion and polycation layers. The influence of the polymer substrates on the structure and fluidity of the lipid bilayers is investigated in terms of suitability as solid supports for biotechnological applications. In the following chapters, we show how molecules bound to the membrane and within the lipid bilayer can be resolved and characterized with X-ray reflectivity and fluorescence microscopy. In

chapter 4, we model receptor-ligand interactions in cellular membranes by binding the proteins streptavidin and avidin to biotin receptors embedded in supported lipid bilayers. The implications of protein binding on lipid bilayer fluidity and stability are quantified and discussed. In chapter 5, we study the membrane receptor G_{M1} ganglioside in supported lipid bilayers composed of complex mixtures mimicking the approximate compositions of mammalian cell membranes. The phase behavior of separate bilayer leaflets is investigated and the influence of G_{M1} on lipid bilayer condensation and leaflet asymmetry is discussed.

Part of this work has been published or submitted for publication [1–5]. The full text articles are attached in Appendices A.1 to A.5.

Chapter 2

A microfluidic setup for studies of solid-liquid interfaces using X-ray reflectivity and fluorescence microscopy

Part of the work described in this chapter has been published [1]. The full article is attached in Appendix A.1.

Solid-liquid interfaces cannot be easily characterized by X-rays due to strong incoherent interactions with the aqueous environment, which give rise to significant beam attenuation and background scattering. Furthermore, biological interfaces usually consist of 'light' molecules such as carbon and hydrogen with a small atomic number, offering minimal scattering contrast for X-rays.
Due to these limitations, the investigation of solid-liquid interfaces by means of diffraction techniques has traditionally been a domain of neutron reflectivity. Thermal neutrons ($\lambda \sim 1.8$ Å) interact with the atomic cores of molecules according to the specific scattering length of the isotope. This offers the advantage of contrast variation: Neutrons distinguish between isotopes such as hydrogen and deuterium, and substituting hydrogen with deuterium at selected atomic positions within a biomolecule strongly increases scattering contrast. Significant restrictions of this technique are the notoriously low flux available at neutron sources, limiting the depth resolution to several nanometer, and the need for large samples with area dimensions of several cm^2.
A major goal of this thesis was to develop an experimental setup to facilitate the application of X-ray reflectivity for the study of biological interfaces, in particular solid supported membranes. The main motivation is to utilize highly brilliant X-ray beams offered by modern synchrotron sources to potentially achieve subnanometer-resolution with X-ray reflectivity. Furthermore, the experimental setup should con-

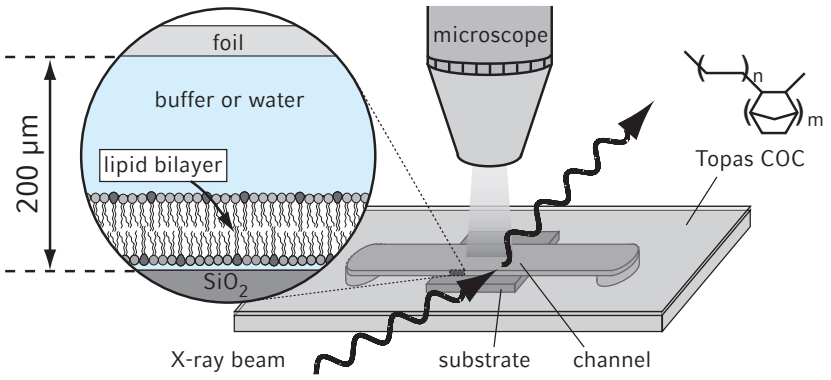

Figure 2.1: Schematic of the microfluidic setup.

sist of a compact sample chamber which additionally allows for the application of fluorescence microscopy. Using this technique, sample homogeneity and lateral structures on the micron scale can be characterized and lipid dynamics within supported lipid bilayers can be quantitatively measured using continuous bleaching.
A rigid thermoplastic polymer (2-norbornene ethylene, or Topas[1] COC) with low mass density (1.02 g/cm^3) was chosen as the chamber material [25]. Topas has a low attenuation for X-rays and its optical transparency makes it well suited for microscopy applications. A schematic of the microfluidic setup is presented in Fig. 2.1. The chamber design is very compact and consists of a microfluidic channel (5 mm $\times$ 50 mm $\times$ 200 μm, width $\times$ length $\times$ height), manufactured by injection molding. Within the plastic chamber, a solid substrate (in most cases a silicon wafer) is embedded and faces the bottom of the microchannel. The channel is sealed on the top by a thin foil of Topas (thickness 200 μm). The thin transparent foil and the small channel height permit optical observation of the substrate using standard microscope objectives. Due to the compact channel dimensions (volume $\sim$ 50 μl), only small amounts of liquid are necessary for sample preparation. A detailed description of the setup is given in Ref. [1].

2.1 X-ray reflectivity

In X-ray reflectivity, a monochromatic beam impinges on a stratified interface with a small grazing angle, typically $\leq 3^\circ$, and is specularly reflected. The reflected signal represents the superposed reflection from different interfaces, which eventually

[1]Topas is a cyclo olefin copolymer (COC) copolymerized from norbornene and ethylene. Topas COC is a trademark of Ticona GmbH, Fankfurt, Germany.

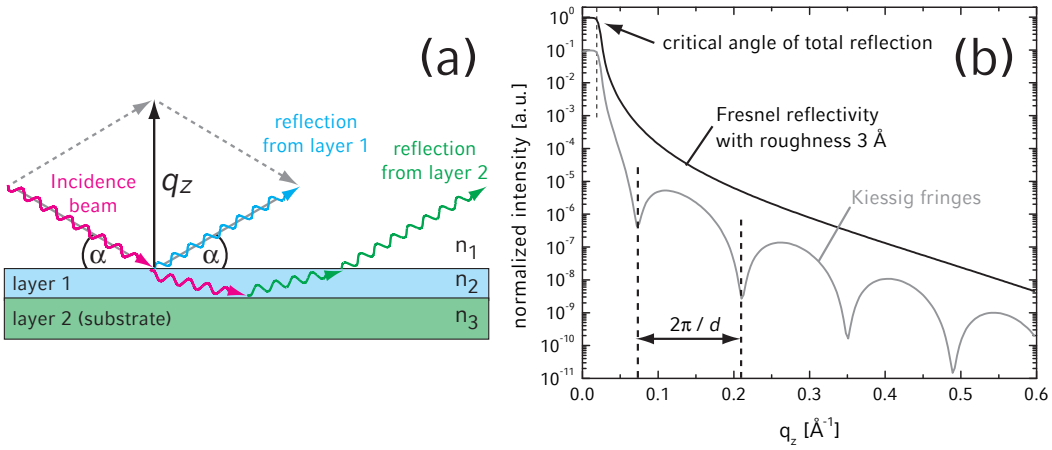

Figure 2.2: (**a**) Schematic of the scattering geometry for a substrate with a single surface layer. An incoming X-ray beam is reflected from the different interfaces depending on their respective refractive indices ($n_{1,2,3}$). The superposition of multiple reflections results in interference in the reflectivity signal [28]. (**b**) Calculated reflectivity for a bare substrate at the silicon-water interface (*dark line*) and for a substrate with a single surface layer of $d = 40$ Å (*gray line*). A uniform interface roughness of 3 Å is included in the calculation. The periodicity of the Kiessig fringes is related to the layer thickness by $\Delta q = 2\pi/d$.

exhibits characteristic oscillations, often termed Kiessig fringes (Fig. 2.2). The first comprehensive theory of reflectivity based on Fresnel optics has been given by L. G. Parratt [26] and extensions to the theory to account for interface roughnesses have been subsequently developed by L. Névot and P. Croce [27]. A detailed and thorough description of the experimental technique and modern approaches for data analysis are given in Ref. [28].

In order to choose a favorable X-ray energy for our experiments, the different contributions to the X-ray cross section were examined (Fig. 2.3). The main processes that govern the material- and energy-dependent interactions of X-rays with matter are (1) coherent elastic scattering, which we consider as the relevant signal from the interface, and then attenuation processes such as (2) photoelectric absorption and (3) incoherent Compton scattering. Increasing the X-ray energy primarily reduces photoelectric absorption and thereby minimizes radiation damage and incoherent background. However, the elastic scattering signal is reduced as well at higher energies and Compton scattering becomes the dominating interaction. Thus, the choice for the optimal energy depends on the chamber material, the chamber dimensions, and the chemical composition of the interface. For the specific case of our compact liquid-filled microfluidic chamber, we have calculated an optimal ratio of coherent to incoherent scattering of 0.12 within an energy range of 20-30 keV. The cross sections presented in Fig. 2.3 were obtained from the

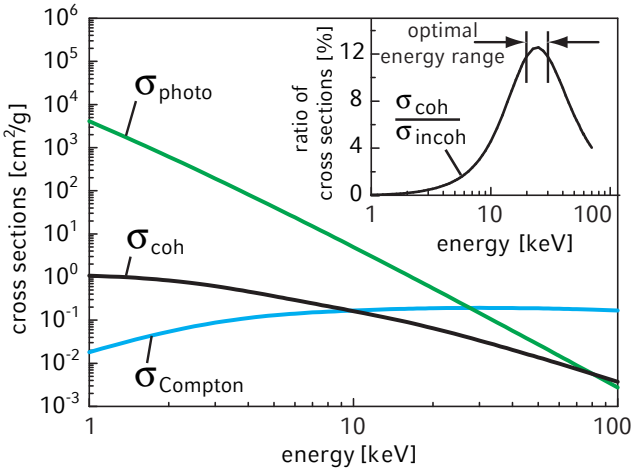

Figure 2.3: Scattering cross sections for an X-ray beam penetrating the microfluidic chamber. The coherent scattering signal from a biological interface is approximated by the elastic scattering cross section of carbon (σ_{coh}). The incoherent cross section (σ_{incoh}) is the sum of the photoelectric absorption (σ_{photo}) and inelastic Compton scattering (σ_{Compton}) along a beam path of 20 mm plastic and 5 mm water, approximating our microfluidic chamber. The calculations are described in Ref. [1]. The inset shows the ratio of coherent to incoherent scattering contributions and indicates the optimal energy range between 20 and 30 keV.

Photon Cross Sections Database[2] (XCOM) at the National Institute of Standards and Technology (NIST), Gaithersburg, Maryland, USA.
Typical laboratory X-ray tubes are operated with anodes of copper or molybdenum, which provide monochromatic X-rays of energy 8 keV (λ =1.54 Å) and 17.4 keV (λ =0.71 Å), respectively. The high energy range (>20 keV) is not accessible with sufficiently high flux for high-resolution studies of solid-liquid interfaces using such standard laboratory tubes. For example, our inhouse small angle X-Ray scattering setup (SAXS) is operated with a molybdenum anode and provides a maximum flux of $\sim 7\times10^{6}$ photons/s; in comparison with an available flux of $\sim 2-5\times10^{10}$ photons/s at the undulator beamline ID01 at the European Synchrotron Radiation Facility (ESRF) in Grenoble, France.
Therefore, first synchrotron experiments with the microfluidic setup were performed at the bending magnet beamline D4.1 at the Hamburger Synchrotronstrahlungslabor (HASYLAB), Germany, at an energy of 19.5 keV, where we could demonstrate that the intensity loss due to beam attenuation within the liquid-filled chamber is ~70 %. This is less than one order of magnitude and consistent with our preceding calculation. The best resolution was achieved at the ESRF, where reflectivity curves could be recorded over a range of 8 orders of magnitude up to

[2] http://physics.nist.gov/PhysRefData/Xcom/Text/XCOM.html

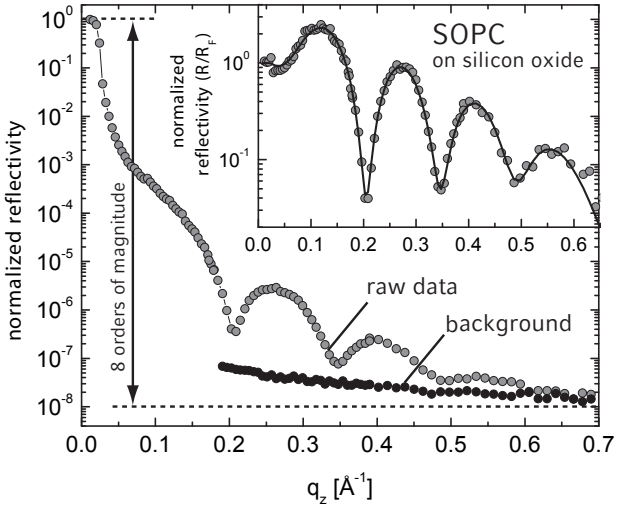

Figure 2.4: Reflectivity scan of a supported lipid bilayer (SOPC) on silicon oxide, taken at the ESRF. Using the present setup, the reflectivity can be recorded over 8 orders of magnitude. The inset shows the background corrected data, normalized by the Fresnel reflectivity, and a fit to the data (*solid line*).

a maximum momentum transfer of $q_z = 0.6$ Å^{-1} (Fig. 2.4). The momentum transfer perpendicular to the interface is defined as a function of the incidence angle α,

$$q_z(\alpha) = \frac{4\pi}{\lambda} \cdot \sin(\alpha), \tag{2.1}$$

where λ denotes the X-ray wavelength. Our accessible spatial resolution is estimated to be $d = \pi/q_z \sim 5$ Å. Throughout this thesis, the software Parratt32 (version 1.6) was used for evaluation of reflectivity data[3]. The software was written by Christian Braun (Hahn-Meitner Institut, Berlin). It calculates electron density profiles according to user-defined slab models and fits the reflectivity based on L. G. Parratts recursive algorithm [26, 27]. The required refractive indices of individual slabs for a given X-ray wavelength were obtained from the Optical Constants Database[4] [29], located at the Center for X-Ray Optics (CXRO) at Lawrence Berkeley Laboratory, California, USA. For many of the data presented in this thesis, the reflectivity (R) is divided by the theoretical Fresnel reflectivity (R_F) of a single, perfectly smooth interface:

$$R_F = \left| \frac{1 - \sqrt{1 - (q_c/q_z)^2}}{1 + \sqrt{1 - (q_c/q_z)^2}} \right|^2 . \tag{2.2}$$

The momentum transfer at the critical angle of total reflection is denoted as q_c. The Fresnel normalization (R/R_F) can help to better pronounce distinct features

[3] http://www.hmi.de/bensc/instrumentation/instrumente/v6/refl/parratt_en.htm
[4] http://henke.lbl.gov/optical_constants/

of the experimental data, especially at high q_z (Fig. 2.4).
First measurements of a lipid bilayer of SOPC[5] supported on silicon oxide showed that the reflectivity signal exhibits clear and pronounced Kiessig fringes (Fig. 2.4). These data confirmed that a single supported lipid bilayer (SLB) at the silicon-water interface produces sufficient electron density contrast to be precisely resolved by high energy X-rays.

2.2 Fluorescence microscopy at the synchrotron

During the experimental visits to HASYLAB and ESRF, a compact and transportable fluorescence microscope (Axiotech vario, Carl Zeiss AG, Oberkochen), equipped with 10× (N.A. 0.3) and long-distance 63× (N.A. 0.75) Plan-Neofluar objectives, was transported to the synchrotron. In a typical synchrotron experiment, the X-ray beam illuminates a surface area of up to 1×1 mm^2 in size, which is comparable to the area usually visualized by standard microscopy objectives. Using the microscope, the samples were thoroughly assessed for homogeneity prior to and after the X-ray reflectivity measurements. For the optical characterization, lipid bilayers were labeled with small amounts of fluorescent dye (typically $\sim$0.5 mol % Texas-Red DPPE[6]). The fluorescence microscope was particularly useful for assessing sample defects introduced by preparation method and radiation damage. Overexposure of the biological interface to high flux X-rays was a major challenge in our first synchrotron experiments. Reflectivity data measured repeatedly on the same spot were not reproducible and significant radiation damage along the X-ray footprint was observed with fluorescence microscopy (Fig. 2.5). We have developed several strategies to limit radiation damage effects: First, an automatic shutter system ensured that the sample is not unnecessarily exposed to the beam during motor movements of the beamline stage. Second, computer controlled beam attenuators in front of the sample limited the imparted incidence intensity, especially for small angles ($<1^\circ$) where the reflectivity signal is sufficiently intense and does not require the full intensity. Third, only the minimum amount of data points necessary for a thorough data evaluation were collected and successive reflectivity measurements on the same spots were avoided. The combination of these procedures has proven successful for suppressing radiation damage, as verified by the exact reproducibility of at least two consecutive reflectivity measurements on a single spot.
The fluorescence microscope was used to monitor sensitive steps in sample preparation such as protein binding to the SLBs, particularly for successive X-ray measurements on a single sample. A comprehensive example for the feasibility of such complementary X-ray reflectivity/fluorescence microscopy studies is given in

[5] 1-stearoyl-2-oleoyl-*sn*-glycero-3-phosphocholine
[6] Texas Red - 1,2-dihexadecanoyl-*sn*-glycero-3-phosphoethanolamine

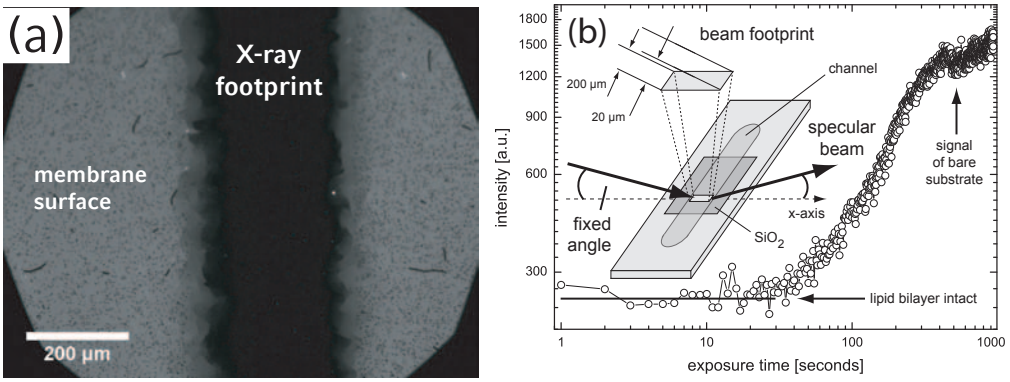

Figure 2.5: (**a**) Observed radiation damage along the X-ray footprint after prolonged exposure (several minutes) to the full beam intensity at the ESRF. The small, circular dark spots on the surface are inhomogeneities in the membrane, introduced during sample preparation. (**b**) The radiation damage to a SOPC bilayer was monitored by recording the temporal degradation of the reflectivity signal at a fixed incidence angle, namely at the position of the first minima in the scan of Fig. 2.4, using the full beam intensity at the ESRF. The absolute intensity remains unaffected for up to ∼30 s; for longer times, the signal starts to increase due to radiation damage and approaches the expected signal of a bare water/silicon oxide interface.

Ref. [4], where we have assessed streptavidin/avidin binding to biotin anchors in a supported lipid bilayer.

2.3 Quantitative fluorescence microscopy: Continuous bleaching

Measuring lateral lipid diffusion in a supported lipid bilayer is important for understanding the influence of the substrate on the lipid mobility and to quantify lipid dynamics [30]. A high mobility is also required for protein binding to lipid bilayers. Most established techniques for measuring lipid diffusion, such as fluorescence recovery after photobleaching (FRAP), require laser bleaching [12]. We have used a standard fluorescence microscope with a mercury lamp to quantify lipid diffusion in SLBs at the synchrotron using continuous bleaching. Despite its versatility, continuous bleaching is still not a standard technique for measuring lipid diffusion. The theoretical background has been originally developed in Ref. [13] and the experimental procedure is thoroughly described in Ref. [4], together with a comprehensive outline for data evaluation. In brief, the mobility of the fluorescent dyes incorporated in the bilayer is monitored by illuminating a roughly circular spot of typically 100−200 μm diameter (Fig. 2.6). It is crucially important for a quantitative data analysis that the entire spot is evenly illuminated. To ensure this, alignment of the mercury lamp prior to each experiment was necessary. For

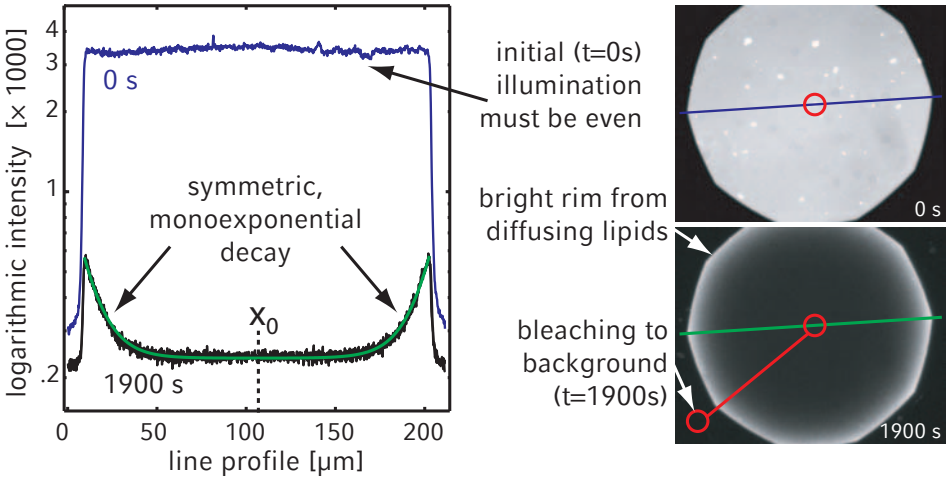

Figure 2.6: Principle of continuous bleaching. A circular spot on the bilayer surface is homogeneously illuminated and the intensity decay in the center is recorded as time-dependent image sequence. While the center area is bleached with time, a bright rim forms at the edge, which is due to unbleached lipids diffusing from the non-illuminated area into the illuminated spot. For prolonged bleaching (here: 1900 s), the center intensity approaches the background level and line profiles through the center of the spot show a symmetric exponential intensity decay at the rim.

a large ensemble of continuously excited dye molecules with a mean fluorescence lifetime, the fluorescence intensity $I(t)$ decays exponentially within the spot as a function of time:

$$I(t) = I_0 \cdot \exp(-B \cdot t). \tag{2.3}$$

The bleach rate B unifies experimental parameters such as luminosity of the mercury lamp, solution conditions, and fluorescent intensity and concentration of the dye. I_0 is the fluorescence for $t = 0$. When the center intensity approaches the background level, the line profiles can be fitted to the spatial intensity decay at the rim:

$$I(x) = I_{\text{rim}} \cdot \cosh\left[\sqrt{B/D} \cdot (x - x_0)\right]. \tag{2.4}$$

I_{rim} is the fluorescence intensity at the rim. The profiles should be symmetric and monoexponential on both sides of the spot. It is important that the center of the sample is bleached to the background level to ensure that no dye molecules are able to cross the spot from one side of the rim to the other, thereby disrupting the data analysis. Using the value for the bleach rate B from Eq. 2.3, the diffusion coefficient D can be extracted from Eq. 2.4. Typical values for diffusion coefficients of supported lipid bilayers vary from 1 to 5 $\mu\text{m}^2/\text{s}$, depending on the substrate properties.

Data analysis for continuous bleaching was done using a self-written MatLab-program. It consists of an intuitive graphical user interface and follows the analysis

procedure described in Ref. [4]. A brief manual is provided in Appendix B.

2.4 Membrane preparation

Lipids are amphiphilic molecules which tend to aggregate in aqueous environments due to hydrophobic interactions [31]. Such aggregates form when the critical micelle concentration (CMC) in aqueous solution is exceeded and they can comprise of a variety of structures, such as micelles and vesicles, depending on the relative sizes of hydrophilic and hydrophobic parts of the lipids (Fig. 2.7). The thermodynamic properties of a lipid bilayer are determined by the length and the degree of saturation of the acyl chains [18, 32]. For example, a lipid bilayer can undergo several phase transitions with varying temperature, ranging from condensed (gel) phases and to non-condensed, fluid phases. Phospholipids forming a fluid phase at room temperature such as DOPC[7] and SOPC have partially unsaturated acyl chains, and therefore low melting temperatures of -20°C and 6°C, respectively. Cholesterol is located within lipid bilayers, where it nests underneath the polar lipid headgroups to avoid water contact. These lipid properties strongly affect the formation of lipid bilayers on solid supports. Common preparation techniques are Langmuir-Blodgett deposition, where two lipid monolayers are subsequently transferred on hydrophilic substrates [33], and fusion of unilamellar lipid vesicles to substrates [34–36], and spin-coating of lipids from organic solvent [37, 38]. In this thesis, the two latter methods were used and modified when necessary for sample preparation.

Vesicle fusion: The adhesion and rupture of unilamellar vesicles on solid supports and the subsequent formation of a continuous supported lipid bilayer (SLB) was first reported two decades ago [34–36]. The complex vesicle-vesicle and vesicle-substrate interactions that govern the process are still not fully understood and an active subject of investigation [39–42]. In principle, the formation of a SLB can be described as a four step process, as depicted in Fig. 2.8. The successful spreading depends critically on membrane composition, substrate material, substrate cleaning procedure, salt concentration, pH, temperature, and size, curvature and bending modulus of the vesicles [10, 43]. Single-component and non-charged vesicles with typical diameters of 50-200 nm have been shown to readily fuse on hydrophilic substrates without external force [10]. We have found an optimal vesicle size of 100 nm for most lipid mixtures used in this thesis. For complex lipid mixtures of cholesterol/brain sphingomyelin/DOPC, as used in Ref. [5], the fusion process was assisted by osmotic stress and thermal activation. These vesicles were prepared in physiological buffer (HEPES) enriched with Na^+, Cl^- and Ca^{2+} ions, providing different ionic strength between the inside and the outside of the vesicle to assist

[7] 1,2-dioleoyl-*sn*-glycero-3-phosphocholine

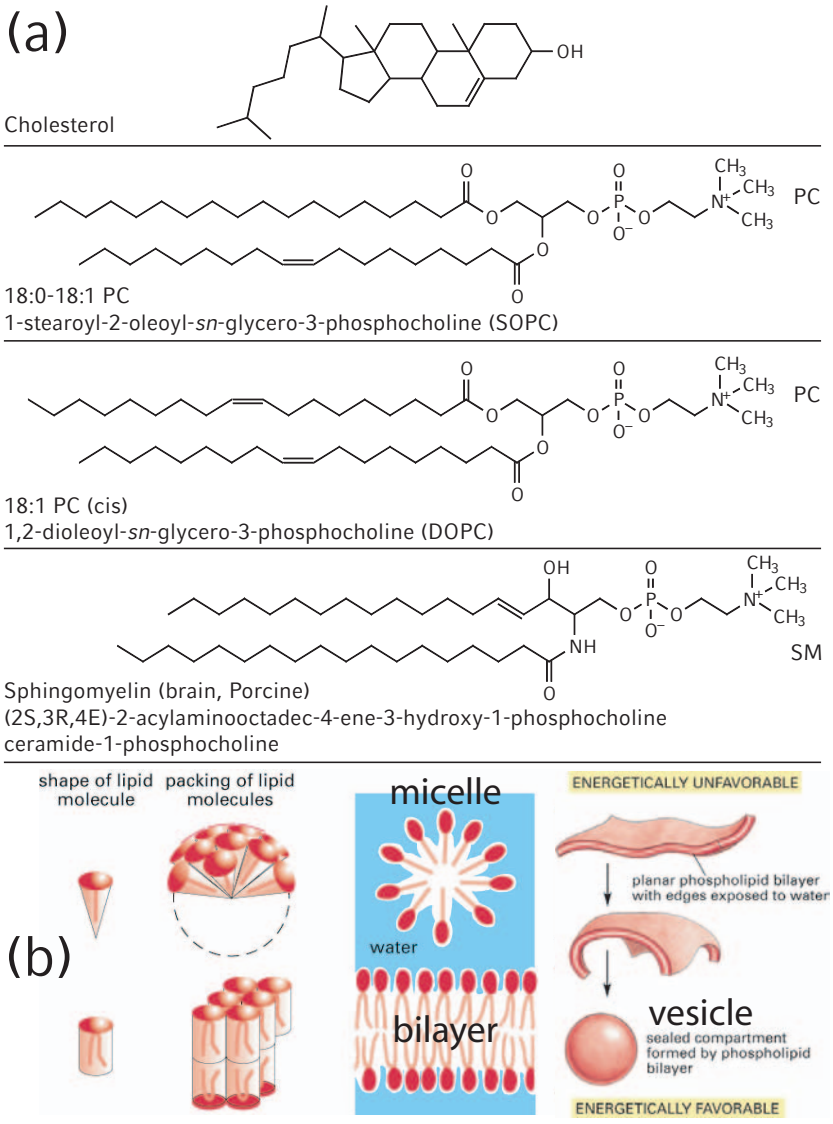

Figure 2.7: (**a**) Chemical structures of the most frequently used lipids in this thesis. Cholesterol has a planar, rigid ring structure and a small polar moiety. Phospholipids (such as DOPC, SOPC) are amphiphilic molecules with two non-polar, hydrophobic fatty acyl chains of varying saturation level. The acyl chains are esterified to the glycerol backbone together with the phosphocholine headgroup, which represents the polar, hydrophilic part. Sphingomyelin consists of a sphingosine and a fatty acid, linked to the phosphocholine by an amide bond. (**b**) For lipids of cylindrical shape, the formation of a vesicle consisting of two lipid monolayers where the hydrophobic acyl chains face each other is energetically favorable. Structural sketches are adapted from Ref. [7] and Ref. [8].

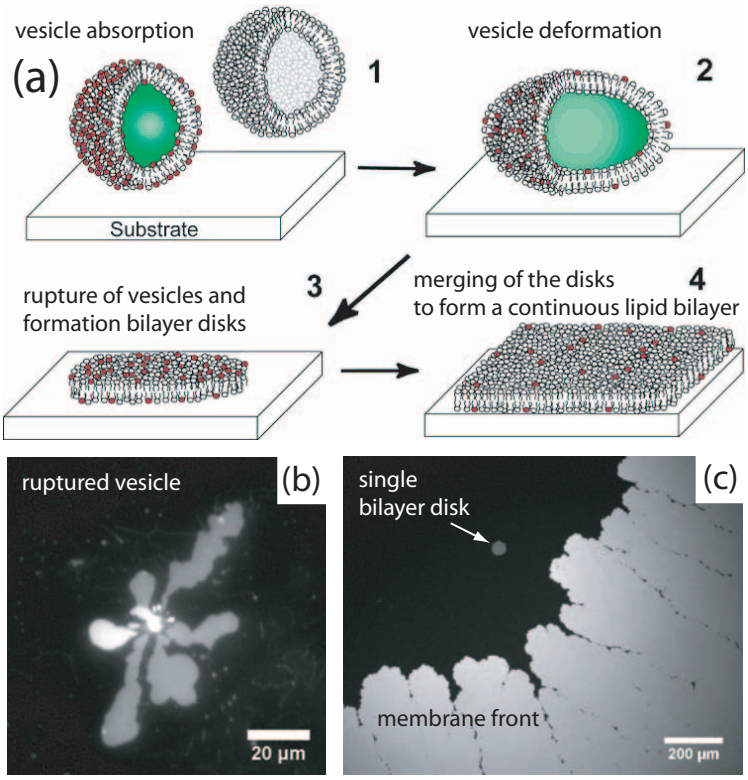

Figure 2.8: (**a**) Mechanism of bilayer formation by vesicle fusion: (1) Unilamellar lipid vesicles in aqueous solution (typically of diameter 50-200 nm) adsorb to a hydrophilic substrate, such as silicon oxide or mica. (2) Attractive adhesion forces with the substrate flatten the vesicle (up to a width to height ratio of 5) and induce tension in the lipid bilayer. (3) Rupture of the vesicle and formation of an isolated bilayer disk. (4) Lipid bilayer disks merge to form a continuous SLB. Schematic is adapted from Ref. [40]. (**b**) Fluorescence micrograph of a ruptured vesicle of SOPC ($\sim \mu$m size) on silicon oxide. (**c**) Spreading of a membrane front (DOPC) across a silicon oxide substrate after vesicle rupture. A continuous SLB is formed.

membrane deformation and rupture at solid interfaces. A detailed protocol is given in Ref. [5].
For lipid mixtures of SOPC and biotin-X-DPPE[8], as used in Ref. [4], vesicle fusion did not occur on silicon oxide at all buffer compositions, lipid concentrations and temperatures used in experiments. In this case, it was necessary to prepare single SLBs by the spin coating technique.

Spin coating: Spin coating of lipid films onto solid supports has been introduced as a preparation method to produce highly oriented and uniform lipid bilayer stacks suitable for X-ray diffraction [14, 37, 44]. This configuration is not stable

[8] N-((6-(biotinoyl)amino)hexanoyl)-1,2-dihexadecanoyl-*sn*-glycero-3-phosphoethanolamine

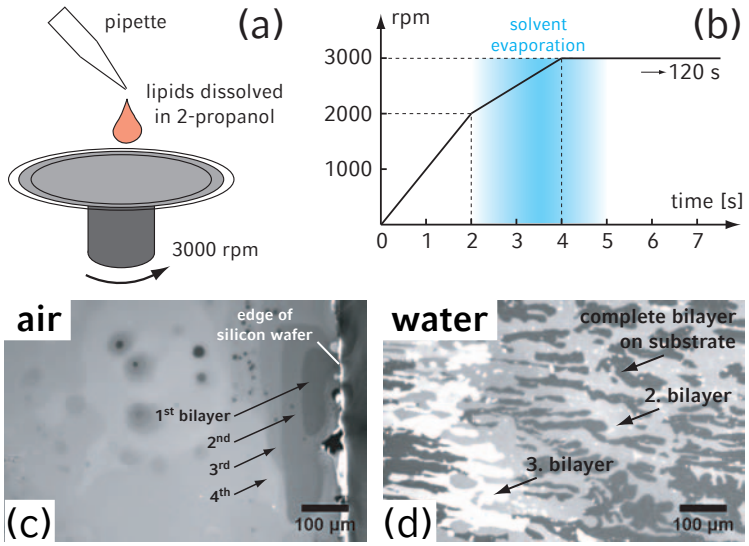

Figure 2.9: Principle of membrane preparation by spin coating. (**a**) A pipette drop of lipid solution in 2-propanol ($\sim$150 μl) is placed on a freshly cleaned silicon oxide wafer, fixed on the spinning disk of the spin coating device. (**b**) The wafer is accelerated according to the depicted ramp. For t $<$ 2s, the low spinning velocity evenly distributes the solvent across the substrate. For t $>$ 2s, the solvent is evaporated upon acceleration to 3000 rpm and the lipid molecules spontaneously self-assemble to form uniform lipid bilayer stacks. (**c**) SOPC multilayers on silicon oxide, as exposed to air directly after spin-coating, using a lipid concentration of 5 mg/mL. The overall surface coverage decreases with increasing bilayer number. (**d**) Continuous flushing of the surface with deionized water or buffer successively detaches the upper bilayers.

in water and it has been observed that individual bilayers readily detach upon hydration [38]. However, the undermost lipid bilayer in direct contact with the solid interface remains on the substrate and is highly homogeneous and defect-free [38]. This makes the technique feasible for the preparation of single SLBs. Lipid mixtures are dissolved in polar organic solvents such as 2-propanol or ethanol to ensure complete wetting of hydrophilic substrates. Lipid stock solutions in chloroform are not readily suited for spin coating since chloroform inadequately wets hydrophilic surfaces such as mica and silicon oxide. A brief outline of the preparation method is depicted in Fig. 2.9 and detailed protocols are given in Ref. [2] and Ref. [4]. A critical parameter which determines the absolute number of bilayers formed on the substrate is the lipid concentration in the solvent. An lipid concentration of 1.5 mg/mL ensures a complete SLB on the substrate, with only small residues of incomplete secondary bilayers on the top [38]. These residues can be washed away with excess water or buffer and subsequent tempering of the sample at $\sim$30°C for several hours leaves a highly uniform and homogenous single bilayer on the substrate.

Chapter 3

Supported lipid membranes on polymer substrates

Many biophysical properties of cellular membranes, such as phase state and membrane curvature, are affected by interactions of the lipid bilayer with the cytoskeleton present in the cell cytoplasm. For example, micron-scale phase separation into coexisting liquid phases has been extensively observed in free giant unilamellar vesicles [45–47], but is not observed in natural cell membranes with complex lipid and protein constituents. Recently, it has been demonstrated that cell membranes are nevertheless capable of micron-scale phase separation once the cytoskeleton backbone is removed [17]. These results suggest that coupling of the plasma membrane to the underlying cytoskeleton may prevent microscopic segregation. The biophysical properties of supported lipid bilayers (SLBs) are also considerably influenced by interactions with the solid support [9, 48, 49]. For example, comparative studies of lipid diffusion in free giant unilamellar vesicles and mica supported lipid bilayers have shown that the diffusion coefficients of DOPC bilayers are reduced by a factor of two at the solid interface (from D=7.8$\pm$0.8 μm^2/s to 3.1$\pm$0.3 μm^2/s, respectively) [30].

Substrates for biomimetic lipid membrane preparation should have a high hydrophilicity in order to enhance adhesion, rupture and surface spreading of vesicles to form continuous lipid bilayers [35, 49]. Suitable substrates include silica surfaces (such as glass, quartz, sputtered silicon dioxide) [50] and hydrophilic mica [51], on which lipid bilayers retain a high lateral fluidity and similar thermodynamic properties as compared to free standing bilayers. However, on similar solid supports such as TiO_2, oxidized platinum and oxidized gold, vesicle adhesion takes place but rupture and formation of homogeneous and fluid bilayers is not readily facilitated [39]. In addition to the aforementioned solid supports, polymers are interesting substrates for lipid bilayers as well, since they can be easily modified in terms of lateral structure, surface charge and hydrophobicity/hydrophilicity. For example, fluid and homogeneous membranes can be successfully formed on oxidized

poly(dimethylsiloxane) (PDMS), and the chemical composition of the substrate can be locally modified to support either lipid monolayers or bilayers, or even reject lipid adhesion in a controlled fashion [52]. For biosensoric applications, controlling the local composition and dielectric properties of SLBs is important for using them as interfaces between biological systems and inorganic materials. In this chapter, structural studies of SLBs on two polymer substrates with potential for applications in biology and biotechnology are presented.

3.1 Lipid membranes on a thermoplastic substrate

Part of the work described in this section has been published [2]. The full article is attached in Appendix A.2.

In this work the properties of lipid bilayers supported on 2-norbornene ethylene (Topas) were investigated. Topas is the building material of our microfluidic sample chambers and we had previously observed the formation of fluid membranes directly on the chamber material. This raised the question of whether Topas itself provides a suitable substrate for SLB formation. Known material properties of Topas which qualify it for lab-on-a-chip applications include a high UV-transparency, low water absorption and chemical resistivity against hydrolysis, polar organic solvents and most acids and bases [53]. Further, thermal nanoimprint lithography can be used to provide well-defined surface geometries [53]. The water contact angle of Topas is 89° and is situated in the intermediate range between hydrophilic and hydrophobic surfaces. It was therefore important to clarify the structure and mobility of lipid membranes on such surfaces, since it is unclear whether the support facilitates the formation of a lipid monolayer or a lipid bilayer. For comparison, the surface chemistry of PDMS has been systematically modified to produce supports with different hydrophilicity [52]. The formation of supported fluid bilayers was observed at contact angles $< 30°$, whereas fluid supported monolayers were observed for contact angles $> 109°$. Thus, the key questions were: What kind of lipid structure forms on Topas? How does the fluidity of that lipid phase compare to lipid fluidity on other supports?
As a first step, we prepared well-defined interfaces of Topas and assessed the surface roughness. A smooth interface is not necessary for the formation of lipid membranes, but it is important for enhancing the reflectivity signal. Topas dissolved in toluene was spin coated onto silicon oxide substrates of surface roughness 3 Å. The resulting Topas layer was characterized with X-ray reflectivity both on air and in contact with water at the beamline ID01 (ESRF) and had an average roughness of 7 Å. The thickness ($\sim$ 450 Å) and electron density (0.24 $e^-/Å^3$) did not change in the presence of water, indicating that no swelling of the Topas layer occurred.

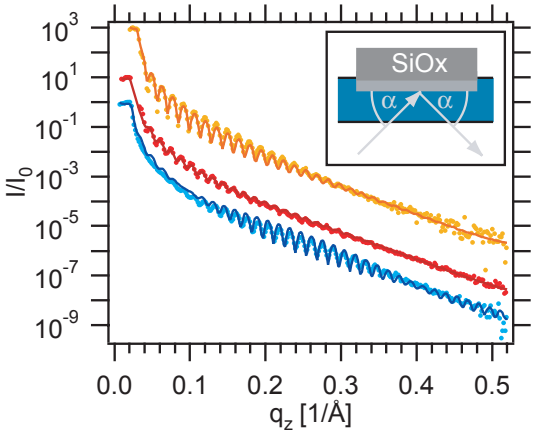

Figure 3.1: Reflectivity data of Topas films on silicon oxide, measured on air (orange dots), in water (red dots) and after deposition of a DOPC membrane (blue dots). The presence of a DOPC membrane imposes a shift in the surging amplitude on the Kiessig fringes. Data fits are included as solid lines. The curves are normalized and shifted vertically for clarity. The inset illustrates the scattering geometry during the measurements.

Supported lipid membranes of various mixtures of neutral DOPC[1] and cationic DOTAP[2] were prepared on the Topas-layered substrates by vesicle fusion. Mixtures of DOPC and DOTAP were chosen because they are relevant for cationic lipid-mediated nucleic acid and protein delivery [54]. Both acyl chains of these lipids are unsaturated (18:1) and ensured that the membrane was in the fluid state at room temperature. Small amounts of the dye NBD-PC[3] were incorporated for fluorescence microscopy experiments.
The formation of complete and homogeneous lipid membranes of compositions DOPC:DOTAP (molar percentage 100:0, 90:10, 50:50, 25:75 and 0:100) was verified by fluorescence microscopy and the lipid mobility was independently assessed using both continuous bleaching and fluorescence recovery after photobleaching (FRAP). Using continuous bleaching, the diffusion coefficients obtained for these compositions were in the range 2 ± 1 $\mu m^2/s$. The sensitivity of these experiments was limited by non-ideal illumination of the samples. Thus, a more precise determination of the diffusion coefficients was attempted using FRAP. The diffusion coefficients were 0.83 $\mu m^2/s$ in all cases and no dependence on the amount of cationic lipid was observed. These values are smaller than the diffusion coefficients reported from fluid lipid bilayers on hydrophilic mica ($1-4$ $\mu m^2/s$) [51] and silicon oxide ($2-4$ $\mu m^2/s$) [35] at room temperature.

[1] 1,2-dioleoyl-*sn*-glycero-3-phosphocholine
[2] 1,2-dioleoyl-3-trimethylammonium-propane
[3] 2-[12-(7-nitrobenz-2-oxa-1,3-diazol-4-yl)amino]dodecanoyl-1-hexadecanoyl-*sn*-glycero-3-phosphocholine

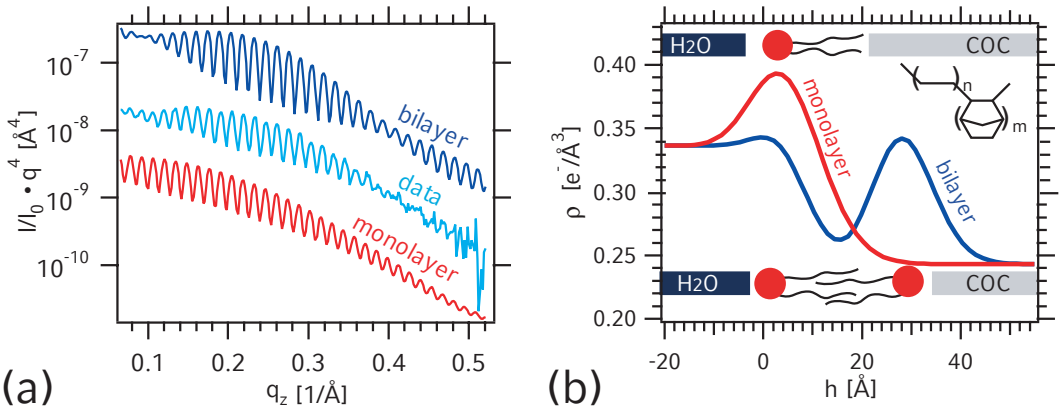

Figure 3.2: (**a**) The measured reflectivity of a DOPC membrane on Topas is plotted with Fresnel normalization (*center*) and compared with the optimal data fits obtained from fitting a bilayer (*top curve*) or a monolayer model (*bottom curve*). (**b**) Electron density profiles corresponding to the fit curves. Schematic drawings of the proposed models are included. The structural formula of Topas is placed in the upper right corner.

X-ray reflectivity measurements were performed at the ESRF on DOPC membranes supported on Topas. After deposition of the membrane, the observed Kiessig fringes were still dominated by the oscillations resulting from the Topas layer; however, the presence of additional layers (thickness $\ll$ Topas layer) was clearly indicated by a shift of the surging amplitude (Fig. 3.1). We compared two different structural models to assess the possibility of the formation of a lipid monolayer or a lipid bilayer. We expected one of these two limiting cases to represent the actual state of the membrane and exclude heterogeneous structures, since it was very unlikely that heterogeneously formed membranes would display such a high and uniform lateral lipid fluidity. By simulating the reflectivity based on slab models representing either a lipid monolayer or lipid bilayer, we found that the data were better described by the bilayer model (Fig. 3.2). The characteristic shift of the surging amplitude could not be adequately reproduced by fitting a monolayer model. The bilayer model however described the data reasonably well and a quantitative data fit provided following parameters: Electron density of lipid headgroups ($\rho_1 = 0.34$ e$^-$/Å^3), acyl chains ($\rho_2 = 0.26$ e$^-$/Å^3) and headgroup-headgroup distance ($d = 29$ Å). These results were different from values reported from X-ray studies on silicon oxide supported lipid multilayers of DOPC [55], where the corresponding values were $\rho_1 = 0.44{-}46$ e$^-$/Å^3, $\rho_2 = 0.24{-}0.29$ e$^-$/Å^3 and $d = 37$ Å. The parameters obtained from our work indicated that a lipid bilayer with a substantially modified structure formed on Topas. The bilayer appeared 'thinned' and less densely packed than a bilayer on silicon oxide and exhibited a slightly reduced lipid fluidity. We proposed two possible configurations of the Topas-supported bilayer: A configuration with coiled acyl chains, and a configuration with interdigitated acyl chains (Fig.3.3). Both models account for the reduced

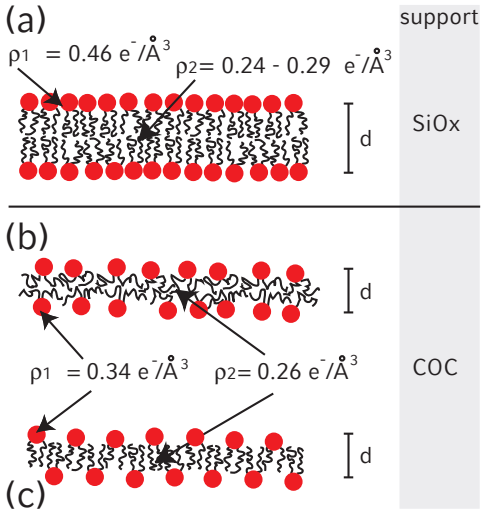

Figure 3.3: (**a**) Schematic of the lipid bilayer structure as found on silicon oxide substrates. The two proposed lipid arrangements within a thinned bilayer on Topas are illustrated below: (**b**) coiled tails and (**c**) interdigitated tails.

bilayer thickness found in this study.

3.2 Lipid membranes on dielectric polymer multilayers

Part of the work described in this section has been published [3]. The full article is attached in Appendix A.3.

Layer-by-layer self assembly of polyanions and polycations on solid supports has evolved as a simple and reliable method to build up multilayer architectures of defined thickness and net charge density [56]. Potential applications are for example silicon-on-insulator transistors, wherein polyelectrolyte multilayers act as a dielectric [57]. The high hydrophilicity of such multilayer stacks also make them promising substrates for lipid bilayers and therefore useful for biosensoric applications. Most of the charges within a polyelectrolyte layer are compensated by the charges of the opposing layer and can be further screened by counterions allocated from buffer solutions [57, 58].
In this study, we intended to characterize polyelectrolyte multilayers of varying thicknesses (number of monolayers n=1, 7, 13) and to investigate the structure of SLBs adhered on top of the uppermost layer in terms structural modifications due to the polyanion/polycation multilayer support. We chose polyallylamine hydrochloride (PAH, positive net charge) and poly(sodium 4-styrenesulfonate) (PSS, negative net charge) to build up multilayer architectures on silicon oxide. This

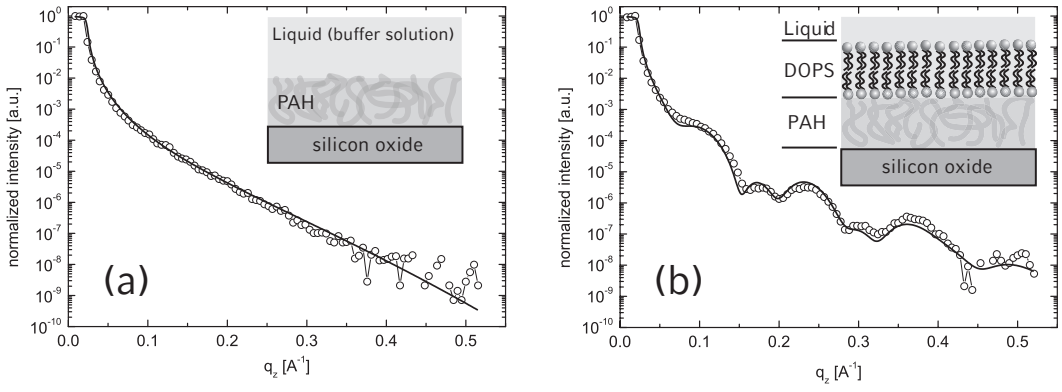

Figure 3.4: (**a**) Reflectivity of a fully hydrated PAH-layer on silicon oxide. No characteristic oscillations were visible. (**b**) Reflectivity of a DOPS-bilayer supported on the hydrated PAH-layer. Solid lines represent data fits. The sketches illustrate the compositions of the respective interfaces, as determined by reflectivity analysis.

polyanion/polycation system has been thoroughly investigated in terms of its dielectric properties [57, 58]. The polyelectrolytes were dissolved in buffer (10 mM Tris, 50 mM NaCl, pH 7.5) and deposited on a silicon oxide substrate using a layer-by-layer procedure. The interface was kept continuously hydrated during sample preparation, since previous structural studies showed that polyelectrolyte multilayers intercalate and irreversibly shrink upon dehydration [59].

We began with the simplest case of only one charged layer (n=1) and deposed a single layer of PAH on silicon oxide. In our first attempt to characterize the PAH layer with X-ray reflectivity at beamline ID01 (ESRF), we were not able to verify the presence of a PAH layer (Fig. 3.4). This could have been either due to improper sample preparation or due to a negligible electron density contrast between water and PAH. The latter case proved to be the actual reason, as subsequent vesicle fusion of DOPS[4] on the substrate strongly modified the reflectivity signal and a data analysis clearly showed the presence of a lipid bilayer supported on a polymer layer of thickness 40($\pm$4) Å (Fig. 3.4). The electron density of the polymer layer is identical to the water density within our experimental sensitivity, which explains why no scattering contrast was observable for PAH alone. It is interesting to note that the formation of a DOPS bilayer is usually inhibited due to repulsive interactions between the negatively charged lipid headgroups and silicon oxide substrates [60]. In the present case, the positive net charge of the uppermost PAH layer and the ionic strength of the buffer sufficiently screened these repulsive interactions.

We then measured more complex multilayer stacks and investigated with X-ray reflectivity the formation of n=7 and n=13 alternating PAH/PSS layers. The terminal layer on top was PAH in both cases. The reflectivity data was recorded at

[4] 1,2-dioleoyl-*sn*-glycero-3-[phospho-L-serine] (sodium salt)

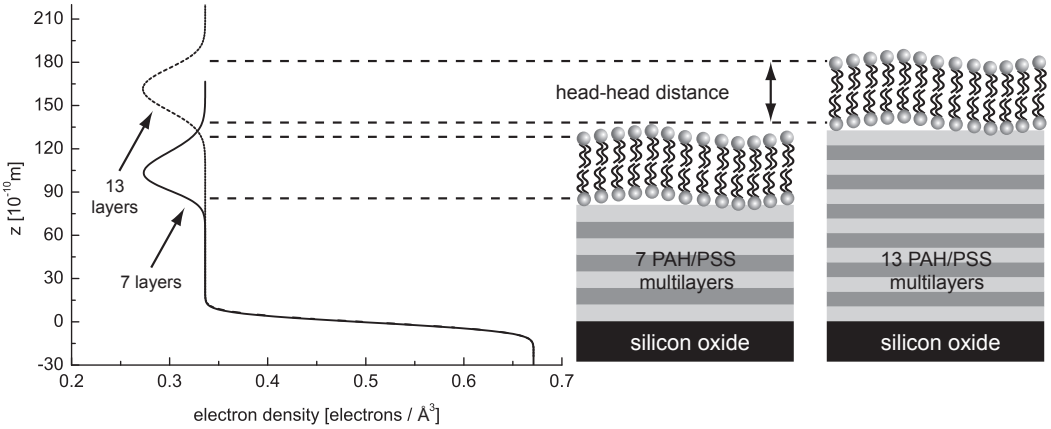

Figure 3.5: Electron density profiles for polyelectrolyte stacks of 7 and 13 multilayers. The most prominent contribution to the contrast is provided by the water-free acyl chains of the polymer supported lipid bilayers.

beamline D4 (Hasylab) and initially did not indicate any presence of multilayers due to vanishing contrast. However, upon incubation of the n=7 layer sample with DOPS vesicles, Kiessig fringes became apparent in the reflectivity, which we have associated in the electron density profile with a water-depleted layer of $\sim$40 Å in a distance of 82($\pm$7) Å (= the multilayer) from the silicon oxide (Fig. 3.5). The Kiessig fringes in the data were well pronounced only in the region of small momentum transfer ($q_z < 0.2$ Å^{-1}) and vanish at higher q_z due to the relatively large interface roughness ($\sim$12 Å) of the terminal PAH-layer on top of the multilayer. Correlative results were obtained in a subsequent experiment, where neutral DOPC vesicles were spread on n=13 PAH/PSS layers. In this case, again a water-depleted region of $\sim$40 Å was found on top of a multilayer of thickness 133($\pm$10) Å with a roughness of 11 Å. We have associated the observed water-free layer in both cases with the hydrophobic acyl chains of a SLB, situated on top of the multilayer structure. The fact that we did not observe representative features of lipid headgroups in both electron density profiles suggests that the roughness of the multilayer surface resulted in a corrugated bilayer, which smeared the laterally averaged headgroup density in the profile. Incomplete surface coverage or intercalation of lipid headgroups within cavities of the underlying polymer could also be a reason for vanishing headgroup contrast.

These experiments allowed us to elucidate the structure of polyelectrolyte multilayers with regard to applications as dielectric polymer cushions for supporting lipid bilayers. Their high water content makes these polar hydrophilic polymers undistinguishable from water by means of X-rays, and allows the SLB to appear as virtually floating. Upon increasing the number of layers, the overall multilayer thickness increases in a nonlinear manner, structurally reflecting the intercalation of multiple polyelectrolyte layers. The surface roughnesses of the investigated mul-

tilayer stacks are $\sim$1 nm and the SLB structure on top appears smeared, although clearly identifiable by the drop in electron density of the hydrophobic acyl chains.

Chapter 4

Structure and dynamics of crystalline protein layers bound to supported lipid bilayers

Part of the work described in this chapter has been published [4]. The full article is attached in Appendix A.4.

The plasma membrane of living cells consists of a variety of lipid species and associated proteins, which can self assemble to form functional lipid-protein complexes. Membrane-associated proteins can be imbedded in the lipid bilayer or peripherally attached to the membrane. Such complexes can locally influence the membrane structure and fluidity through lipid rearrangement within the bilayer. For example, the membrane protein phospholipase A_2 can bind to lipid bilayers and catalyze the hydrolysis of phospholipids into fatty acids and single-chained lipids, thus changing the lipid composition and increasing the membrane heterogeneity [61]. Systematic structural studies of protein binding to model lipid bilayers can elucidate the implications of lipid-protein interactions on membrane structure and fluidity. In the past, efforts have been made to use nanoscale-resolution techniques such as atomic force microscopy (AFM) [11] or X-ray reflectivity [62–64] to study lipid-protein binding events. Whereas the information provided by AFM is limited to height differences in the bilayer, X-ray reflectivity offers detailed conclusions about the molecular arrangement within the bilayer. X-Ray studies consistently report that proteins directly bound to lipid headgroups can intercalate between headgroups and change the lipid arrangement [63, 64]. So far, these studies focus on protein-coated membranes modeled by lipid monolayers prepared in Langmuir troughs, mainly because the air-liquid interface is much more accessible to X-rays than interfaces in a liquid environment. However, we believe that the fluid lipid bilayer at the solid-liquid interface is a much more representative and presumably more stable model system for mimicking cell membranes than the lipid monolayer.

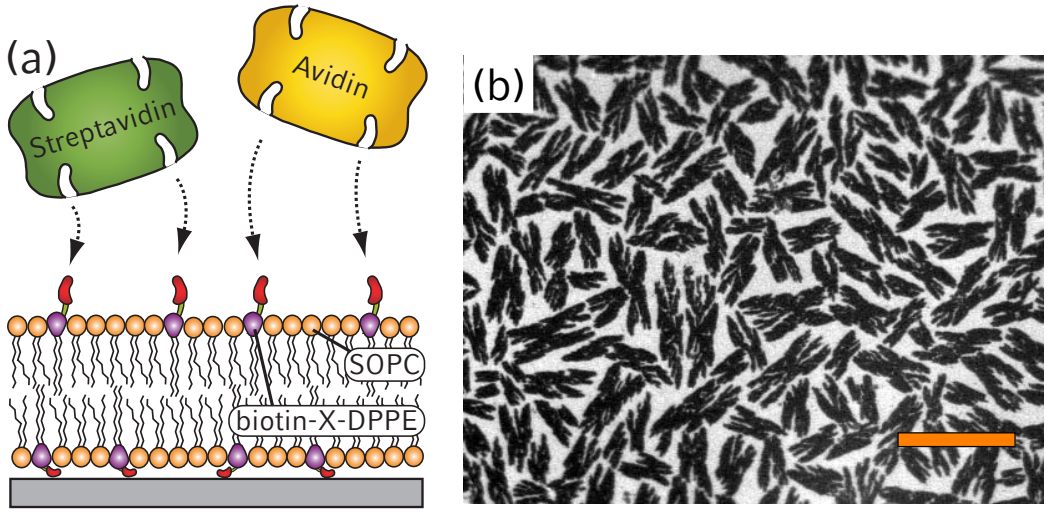

Figure 4.1: (**a**) Schematic of streptavidin/avidin binding to a SLB. (**b**) Fluorescence micrograph of the SLB surface, showing dark crystalline domains of streptavidin, surrounded by a matrix of partially fluorescently labeled avidin. The protein composition for this sample was 50:40:10 mass percent of streptavidin:avidin:alexa488-avidin. Scale bar is 100 μm (*orange*).

In this project, we have studied the binding of the proteins streptavidin and avidin to biotinylated lipids in a supported lipid bilayer by means of X-ray reflectivity and fluorescence microscopy. This model system is widely used in biotechnological research since the streptavidin-biotin interaction has a very strong noncovalent binding affinity. The binding of streptavidin to model membranes occurs through biotin anchors on the membrane surface, where it can form 2D-crystalline arrays [65, 66]. A schematic is shown in Fig. 4.1. In the case of lipid monolayers, it has been reported that the lipid packing is heavily distorted upon streptavidin binding with the protein partially penetrating the monolayer [64]. The key questions raised in our work were: Can we resolve a single protein layer with X-rays? Does protein binding significantly affect the structure of the underlying lipid bilayer, as reported for lipid monolayers? What are the implications for the lipid fluidity upon protein binding?
All experiments were conducted at the beamline ID01 (ESRF) using the microfluidic setup; the same samples were used for X-ray reflectivity and fluorescence microscopy studies. We prepared lipid mixtures of SOPC[1] and biotin-X-DPPE[2] with molar ratio 9:1, respectively, and added a small amount of the fluorescence dye Texas Red DPPE[3]. Single homogeneous SLBs of this lipid composition were deposited on silicon oxide substrates by the spin coating technique. Previous efforts

[1] 1-stearoyl-2-oleoyl-*sn*-glycero-3-phosphocholine
[2] N-((6-(biotinoyl)amino)hexanoyl)-1,2-dihexadecanoyl-*sn*-glycero-3-phosphoethanolamine
[3] Texas Red - 1,2-dihexadecanoyl-*sn*-glycero-3-phosphoethanolamine

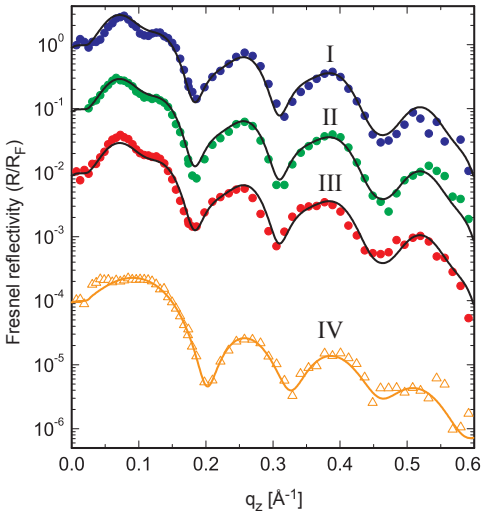

Figure 4.2: Reflectivity scans of protein-coated (*I-III*) and bare SLBs (*IV*). The compositions of the protein solutions were (*I*) 90:0:10, (*II*) 50:40:10 and (*III*) 10:80:10 mass percent of streptavidin:avidin:alexa488-avidin. All data are presented with Fresnel normalization and with the corresponding data fits (*solid lines*).

to form SLBs from these compositions using vesicle fusion were not successful. The proper formation of the single SLBs from spin coating was verified using fluorescence microscopy and the lateral diffusion coefficients were measured by continuous bleaching. All samples showed diffusion coefficients of 2.3 ($\pm$0.4) μm^2/s.
Protein solutions composed of streptavidin, egg white avidin and a fluorescently labeled conjugate of avidin (alexa488-avidin) were used to incubate the samples in different volume ratios of 90:0:10, 50:40:10 and 10:80:10, respectively. Whereas streptavidin is known to form 2D crystal arrays, avidin does not crystallize at neutral pH due to its high isoelectric point of $\sim$10 and its bulky glycosylation groups. Thus, these protein compositions formed dark crystalline streptavidin domains surrounded by partially fluorescently labeled avidin, as shown in Fig. 4.1. The bilayer surface was completely covered with protein for all compositions. The protein domains exhibited the characteristic X- and H-shapes of streptavidin crystals with C222 symmetry as observed on lipid monolayers [67] and giant unilamellar vesicles [65]. The nucleation density, shape and size of the domains were uniform across the whole substrate (20$\times$15 mm^2), indicating large-scale homogeneity of the protein layer and the underlying lipid bilayer. All protein layers appeared immobile on the timescale of continuous bleaching (several hours). We ascribe the immobility to a jammed configuration of avidin among the crystalline streptavidin domains, as a result of full surface coverage. It has been previously reported that proteins bound to membrane surfaces can show a 20- to 100-fold reduced diffusion as compared to the underlying lipids at high surface coverages [68]. The fluidity of the SLBs below the protein was reassessed by continuous bleaching for all samples and

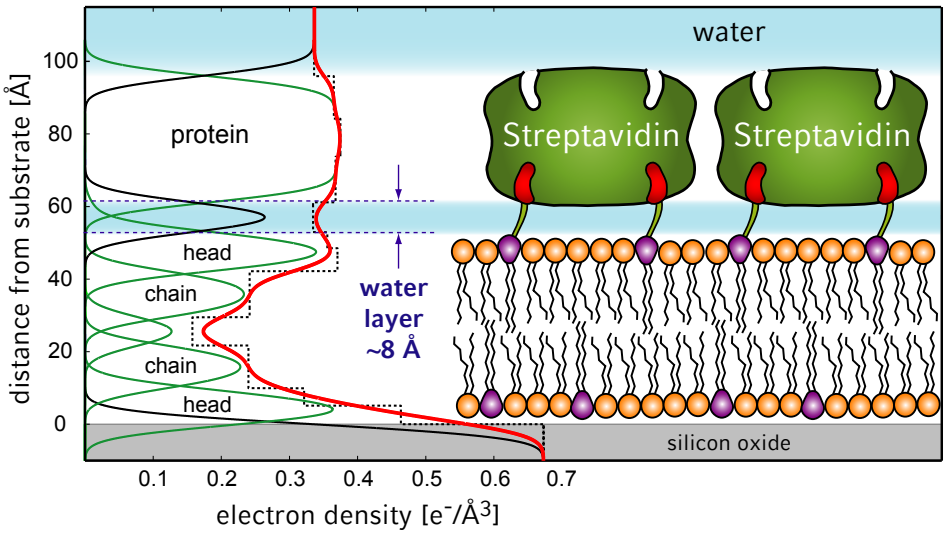

Figure 4.3: Electron density profile of streptavidin/avidin coated SLBs. The overall profile (*red line*) is composed of multiple components, such as the lipid headgroups, the acyl chains and the protein layer (*green sigmoidal curves*). The dotted line corresponds to the slab model employed for fitting the data. The thicknesses of the protein layer (40 Å) and the separating water layer (8 Å) between the protein and the SLB can be clearly resolved.

showed in each case a slightly reduced lipid mobility of 1.9−2.0 ($\pm$0.1) $\mu m^2/s$. Thus the bound protein layer reduced the SLB mobility by only a small amount.
We have characterized the SLBs prior to and after incubation with protein solution using X-ray reflectivity (Fig. 4.2). The electron density profiles of the SLBs lacking the protein were very similar and showed a high symmetry across the leaflets. After full formation of the protein layers, the reflectivity for each sample changed significantly and the fringes exhibited a more complex signature (Fig. 4.2). The data of all protein coated SLBs appeared very similar and were not distinguishable within our experimental resolution. This is not surprising since streptavidin and avidin have very similar structures [69]. Lateral segregation of streptavidin and avidin was not detectable within the sensitivity of our X-ray reflectivity setup. Thus, the quantitative data analysis was done by fitting an 11-slab model to the averaged reflectivity of all protein coated samples. The resulting electron density profile showed an additional feature as compared to the profiles of the bare SLBs, which we have assigned to a protein layer (thickness 40 Å) on top of the SLBs (Fig. 4.3). Interestingly, we resolved an additional layer (thickness 8 Å) separating the protein layer from the SLB. The electron density of this layer matched the value of water (0.334 $e^-/Å^3$); we therefore concluded that this layer predominantly consists of water and, as a minor part, the spacer of biotin-X-DPPE.
We propose that the observed reduction in lipid mobility of 10−15 % is due to

a small fraction of biotinylated lipids that are immobilized within the SLB. These lipids are linked to the immobile protein layer and create obstacles to membrane diffusion. Theoretical descriptions of two-dimensional diffusion among obstacles have been developed in the past [70] and simulated for the case of lipid bilayers [71]. Assuming bivalent binding (one streptavidin/avidin binds two biotinylated lipids), a comparison of the relative sizes of lipids and proteins suggest an immobile lipid fraction of 0.04 at complete surface coverage. Applying the model calculation to our system yields an area fraction of immobilized lipids of $0.02-0.09$ with respect to the error margins of our diffusion coefficients. We can reasonably exclude further lipid-protein interactions that might limit lipid diffusion due to the separation provided by the water layer between the SLB and the proteins. This separation allows the underlying lipid bilayer to retain a high fluidity and stability. In addition, we have shown that the lipid bilayer represents a much more stable lipid layer than lipid monolayers. Our results contrast the observation in monolayers that streptavidin binding rearranges lipids [64]. In general, we have demonstrated that protein binding to lipid membranes does not necessarily modify the membrane structure.

Chapter 5

Condensation, stretching and asymmetry: G_{M1} and cholesterol in single supported lipid bilayers

Part of the work described in this chapter has been submitted for publication [5]. The full text of the submitted manuscript is attached in Appendix A.5.

The structural complexity of cell membranes is reflected by their numerous lipid and protein constituents, which can asymmetrically organize across the membrane leaflets and induce lipid phase separation [18]. The thickness of the membrane and the lipid fluidity depend locally on the length and degree of saturation of the acyl chains. Lipids with long saturated chains such as sphingomyelin preferentially interact with cholesterol to form tightly packed domains in the membrane [19, 22]. Such a condensed lipid phase (also termed liquid ordered, L_o) can coexist with non-condensed lipid phases (liquid-disordered, L_d) over a broad range of temperatures. L_o domains, often referred to as lipid rafts, are proposed to play a key role in membrane organization by concentrating specific receptor molecules into ordered lipid environments, thereby targeting their ligands to specific functional regions in the membrane [7]. The monosialoganglioside G_{M1} is the receptor for cholera toxin entering the cell through the endocytic pathway and has been shown to localize to raft domains in the outer membrane leaflet [72]. The asymmetric localization of receptors within L_o or L_d phases is a structural phenomenon governed by intermolecular interactions within the membrane. The leaflet asymmetry of G_{M1} may also induce an asymmetric distribution of cholesterol, whose exact transbilayer distribution is not known [22]. The particular preference of G_{M1} to partition into cholesterol-enriched L_o phases is likely due to its saturated acyl chains, but there is little knowledge about the interaction of its large oligosaccharide headgroup with the lipid environment [7], although it is known that G_{M1} can decrease the mobility of surrounding lipids [73].

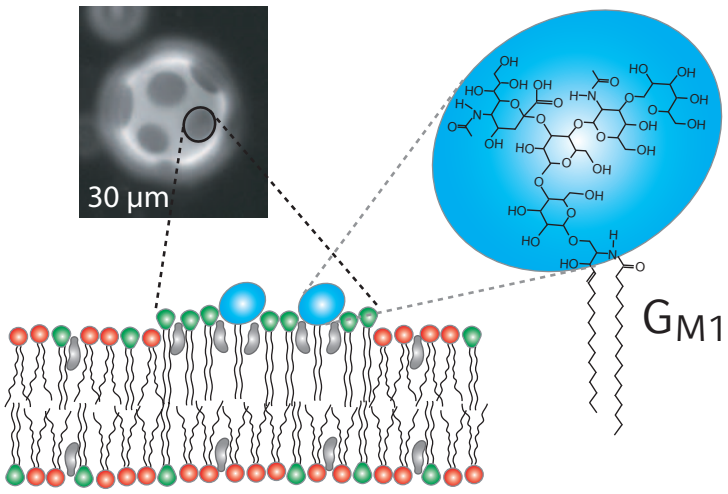

Figure 5.1: Model of a condensed L_o domain (lipid raft) in a lipid bilayer. Lipids within the L_o phase have condensed acyl chains and are close-packed with cholesterol. Cholesterol (*gray*) fills the space under the headgroups of sphingomyelin (*green*). A fluorescence micrograph shows a giant unilamellar vesicle with coexisting L_o and L_d phases.

In this work, we aim to elucidate by means of high resolution X-ray reflectivity how the receptor G_{M1} modifies membrane structure in supported lipid bilayers (SLBs) of one single component and also of more complex compositions enriched with cholesterol. In order to mimic the asymmetric distribution of G_{M1} in the plasma membrane leaflets of mammalian cells, we have adapted a protocol to asymmetrically incorporate G_{M1} into single bilayer leaflets [74]. Of particular interest is the structural effect of G_{M1} in lipid mixtures with L_o and L_d phase coexistence. In principle, the high spatial resolution which is accessible with X-ray reflectivity allow distinct features to be resolved in separate bilayer leaflets.
All X-ray reflectivity experiments were conducted at beamline ID01 (ESRF) using the microfluidic setup described in chapter 2. Single SLBs were deposited on silicon oxide using vesicle fusion assisted by osmotic stress. After SLB formation, G_{M1} was asymmetrically incorporated into the distal leaflet of the bilayers by incubating the SLBs with aqueous G_{M1} solution. G_{M1} can spontaneously partition into the distal leaflet up to concentrations of 30 % due to its amphiphilic nature.
First, we have characterized a single component SLB in the fluid phase and assessed whether lipid packing modifications occur after asymmetric insertion of G_{M1}. The reflectivity data of a fluid lipid bilayer of SOPC before and after insertion of G_{M1} are shown in Fig. 5.2. A detailed data analysis was done using slab model fits, followed by a decomposition of the resulting electron density profile into gaussian components, which represent separate regions in the bilayer. A comparison of the corresponding electron density profiles showed that the SLB was significantly thickened after G_{M1} insertion. The most prominent effect was apparent in the distal

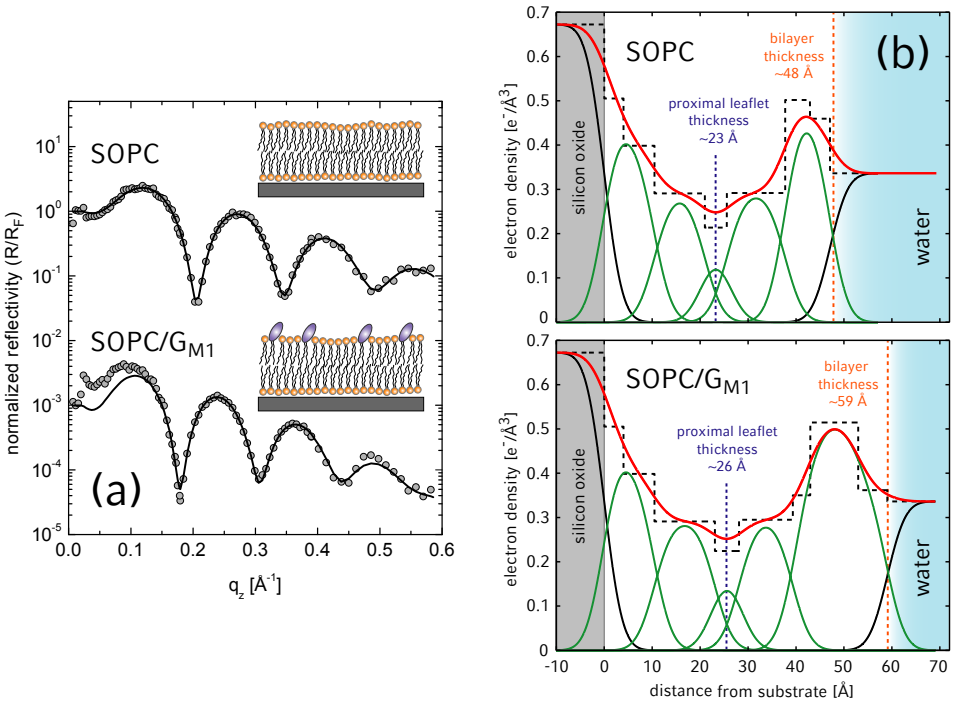

Figure 5.2: (**a**) Normalized reflectivity scans with fits (*solid lines*) for a single SOPC bilayer before and after incubation with excess G_{M1}. Sketches illustrate the approximated bilayer structure and asymmetric incorporation of G_{M1} into the distal leaflet. (**b**) Electron density profiles (*red curves*) with and without incorporated G_{M1}. The green curves represent the separate regions of the membrane: the lipid headgroups, acyl chains and the space where the acyl chains meet. The slab model used for fitting the data is included as dotted line.

bilayer leaflet, whose thickness was increased by 8 Å. We ascribe the thickening to a protrusion of the large oligosaccharide headgroups of G_{M1} above the surface of the neighboring phosphocholine headgroups. The protrusion length of 8 Å is smaller than the reported value of 12 Å from fully extended G_{M1} headgroups in egg PC multibilayers [75], indicating that G_{M1} was not completely extended from the bilayer surface. Our results clearly demonstrate that we were able to create SLBs with asymmetric G_{M1} distribution and we could resolve different regions within the bilayer (headgroups, acyl chains) in nanoscopic detail by means of high-resolution X-ray reflectivity.

In addition, we have investigated whether the binding of the subunit B of cholera toxin (CTB) to G_{M1} has an effect on the SLB structure. CTB can bind 5 G_{M1} receptors on the membrane surface to form a complex that allows the cholera toxin to cross the membrane [72]. Fluorescent labeled CTB was incubated with SLBs containing G_{M1} and specific binding to the SLB was verified by fluorescence microscopy. We could not detect the bound CTB layer on top of the SLB by

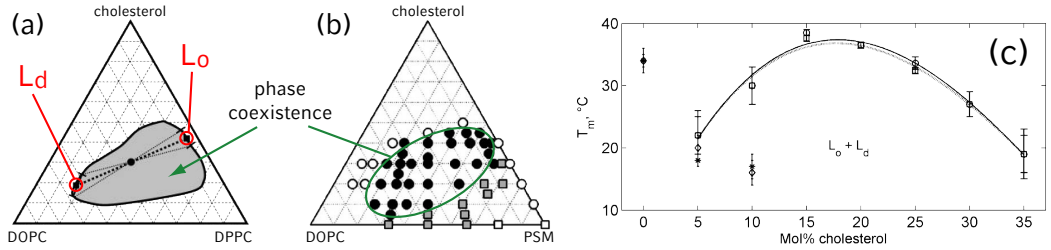

Figure 5.3: (**a**) A tie-line (*thick dotted line*) in the phase diagram of cholesterol/DOPC/DPPC, as estimated for a mixture of 1:1 DOPC/DPPC + 30 % cholesterol at 25°C. Thin dashed lines are bounds on the errors. The figure is adapted from Ref. [76]. (**b**) The similar phase diagram of cholesterol/DOPC/palmitoyl SM for fluid GUVs at T = 23°C is shown. Within the green circle, two liquid phases coexist. White symbols denote membranes which are in one uniform phase, either liquid (*circles*) or solid (*squares*). Black circles denote coexisting liquid-liquid phases, and gray squares denote coexisting solid and liquid phases. The figure is adapted from Ref. [47]. (**c**) Partial lipid phase diagrams of GUVs composed of different cholesterol concentrations and a 1:1 fixed DOPC/bSM ratio. The L_o/L_d liquid-liquid phase coexistence region is indicated. The figure is adapted from Ref. [45].

means of X-ray reflectivity. The SLB structure was not affected upon binding as well, in agreement with our previous studies on similar systems of receptor-ligand binding to a SLB. We ascribe this observation to a lack of electron density contrast between the excess water and the hollow, water-filled ring structure of CTB.
We have also characterized the more complex system of lipid bilayers with ternary lipid mixtures capable of phase separation. Compositions of cholesterol/DOPC/SM in vesicle bilayers can form coexisting L_o and L_d phases, which can grow to microscopic size [47]. We chose two molar ratios of this lipid mixture which we presumed to represent either a 100% L_o or a 100% L_d phase, based on a tie line approximated from the lipid phase diagram of a similar composition (Fig. 5.3). These lipid phase diagrams were originally established for giant unilamellar vesicles (GUVs) [45, 47, 76]. We estimated that a molar composition of 15/65/20 (cholesterol/DOPC/bSM) represents the 100% L_d phase and that a composition of 29/6/65 (cholesterol/DOPC/bSM) corresponds to a 100% L_o phase. The X-ray reflectivity data showed that the SLB of L_d composition had a similar electron density and thickness as compared to the SOPC-bilayer, which is characteristic for a fluid bilayer (Fig. 5.4). The SLB of L_o-composition, however, showed in both leaflets a clearly increased thickness and a higher electron density in the acyl chain region. These measurements allowed us to empirically define condensation in terms of acyl chain length and packing density. In this scheme, both an electron density of 0.28($\pm$0.01) $e^-/Å^3$ and acyl chain length of 14($\pm$1) Å are characteristic of a non-condensed bilayer leaflet, whereas an electron density of 0.33($\pm$0.01) $e^-/Å^3$ and acyl chain length of 17($\pm$1) Å is representative of a condensed bilayer leaflet.

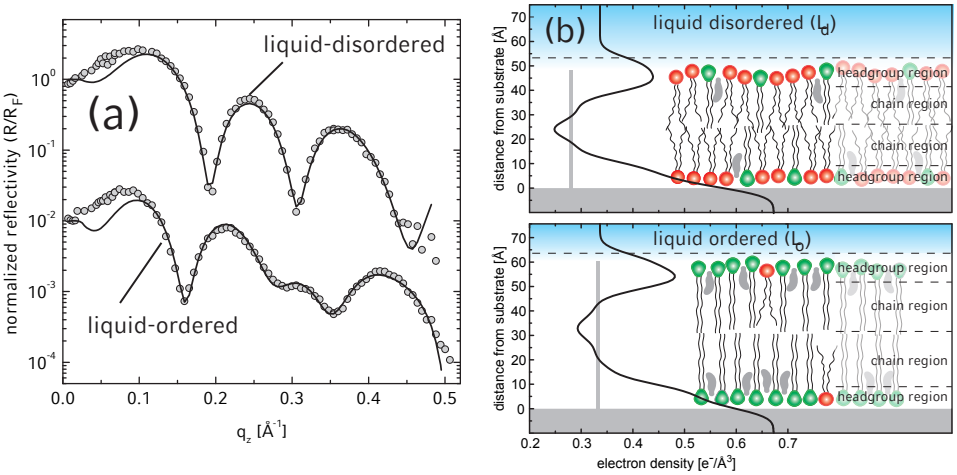

Figure 5.4: (**a**) Normalized X-ray reflectivity of SLBs with ternary compositions of cholesterol/DOPC/bSM, modeling the L_d phase and the L_o phase. Solid lines represent fits to the data. (**b**) Corresponding electron density profiles. The sketches represent the approximated molar ratios of cholesterol (*gray*), DOPC (*red*) and bSM (*green*) in the bilayers and illustrate the differences in bilayer condensation and thickness. The gray bars indicate the average electron density of the acyl chains for the L_d and the L_o compositions.

These threshold values are graphically indicated in the electron density profiles of Fig. 5.4.

Next, we have investigated a series of SLBs from cholesterol/DOPC/bSM mixtures which are capable of separation into coexisting L_d and L_o phases in GUVs. SLBs of molar compositions of 20/40/40 (referred to as *20chol*), 30/35/35 (*30chol*) and 40/30/30 (*40chol*) were chosen. X-ray reflectivity showed that the structure of *20chol* corresponded to a condensed phase, whereas *30chol* *40chol* were non-condensed (Fig. 5.5). A qualitative comparison with the GUV phase diagram shows that condensation is expected in GUVs of composition 20/40/40; whereas GUVs of 30/35/35 are at the onset of L_d/L_o coexistence and GUVs of 40/30/30 are clearly in the non-condensed single phase region [45]. These results indicate that the condensation states of a lipid bilayer on a solid support are at least in partial agreement with the results found in free standing GUVs (compare Fig. 5.3 and Fig. 5.6).

The samples *20chol*, *30chol* and *40chol* were reassessed after asymmetric insertion of G_{M1}. The capability of G_{M1} to locally moderate lipid bilayer shape and fluidity in cholesterol-enriched lipid mixtures has been previously investigated [77, 78]; in this work, we studied the structural implications of G_{M1} insertion into such mixtures. We found that asymmetrically incorporated G_{M1} had only minor structural influence on the already condensed *20chol*-SLB. However, the structures of the non-condensed SLBs, *30chol* and *40chol*, changed significantly in the presence of

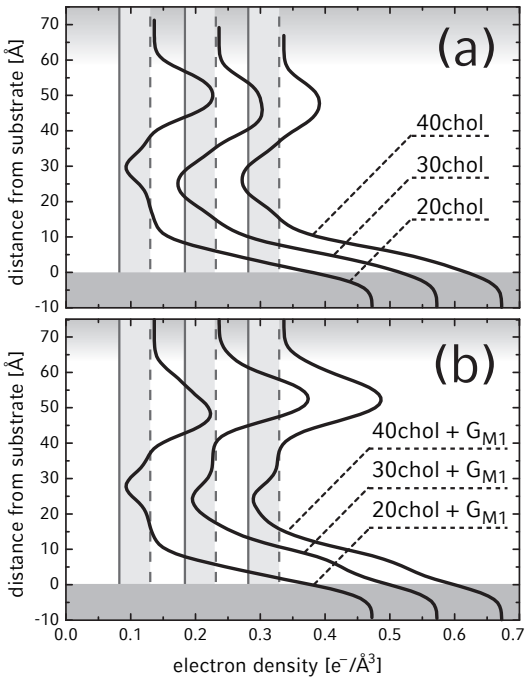

Figure 5.5: Electron density profiles of cholesterol/DOPC/bSM SLBs with equimolar composition of DOPC and bSM, with (**a**) and without G_{M1} (**b**). The electron density axis is correctly aligned for *40chol* and *40chol+G_{M1}*; the other profiles are shifted for clarity. The gray vertical lines indicate the lower and upper threshold values for the electron density of the acyl chains, as defined in the text and illustrated in Fig. 5.4. The intermediate region between the lower value (0.28 $e^-/Å^3$, non-condensed) and the upper value (0.33 $e^-/Å^3$, condensed) is shaded for clarity of presentation.

G_{M1}. These SLBs exhibited a strong condensation in the distal leaflet, where G_{M1} was actually present (Fig. 5.5). The proximal leaflet, lacking G_{M1}, was not affected by the condensation of the neighboring leaflet.

As in our other work, we used fluorescence microscopy to complement the structural X-ray studies. We examined the samples *20chol*, *30chol* and *40chol* for homogeneity prior to G_{M1} incubation. All samples showed uniform fluorescence from Texas Red-DPPE, and no observable phase separation occurred on our smooth silicon oxide substrates (roughness 3 Å). Interestingly, we have observed for all samples the formation of dark immobile domains ($\sim$5 μm) upon incorporation of G_{M1} (Fig. 5.6). These domains did not change size or shape up to a temperature increase of 70°C, suggesting that they were membrane defects such as pinned G_{M1} clusters or bare surface areas. In sample *20chol*, gray spots ($\sim$5 μm) were present which disappeared upon heating at 40°C and reappeared at the same positions upon recooling. The size of these spots and their partial exclusion of the fluorescence dye indicates that the presence of G_{M1} can induce micron scale domain segregation, probably L_o domains. Finally, the lipid diffusion of the samples

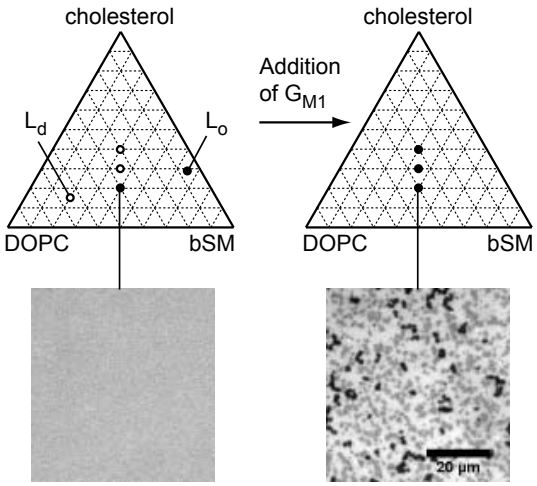

Figure 5.6: Compositional diagram indicating the SLB compositions used in this study. Circles represent non-condensed SLBs and dots represent condensed SLBs, as determined by our reflectivity analysis. Fluorescence micrographs of the sample *20chol* before and after addition of G_{M1} show the SLB surface and the presence of dark and gray spots upon addition of G_{M1}.

20chol, *30chol* and *40chol*, with and without G_{M1}, was assessed using continuous bleaching. We found that the lipid fluidity was significantly reduced upon G_{M1} incorporation ($\sim$50%), which provides further evidence of condensation in the membrane, as ordered lipid phases show a reduced diffusion [51].
The insertion of G_{M1} into supported lipid membranes stretches the outer membrane leaflet and increases the lipid headgroup density, consistent with a structural effect of the G_{M1} headgroup protruding out from the membrane surface. We observed this effect with X-ray reflectivity in single component SLBs of SOPC and also in more complex ternary mixtures containing cholesterol. We were able to distinguish between condensed and non-condensed SLBs and determined how the different regions within the SLB (headgroups, acyl chains) are affected by the presence of G_{M1}. We clearly show that asymmetric inclusion of G_{M1} has a condensation effect on cholesterol-enriched lipid bilayers and that this effect is restricted to the leaflet where G_{M1} is present. As an additional effect, we found that G_{M1} reduces the lipid diffusion of cholesterol-enriched SLBs and introduces segregated domains in the bilayer.

Appendix A

Publications

A.1 Full text of Ref. [1]

Christian Reich, Marion B. Hochrein, Bärbel Krause and Bert Nickel

A microfluidic setup for studies of solid-liquid interfaces using x-ray reflectivity and fluorescence microscopy.

Review of Scientific Instruments **76**, 095103 (2005).

This paper also has been selected for the compilation journals

Virtual Journal of Nanoscale Science & Technology **12** Iss. 12 (2005).
and
Virtual Journal of Biological Physics Research **10** Iss. 6 (2005).

Abstract:
In this paper we present a concept for a microfluidic chamber optimized for x-ray reflectivity studies at solid-liquid interfaces. Experiments of this kind are usually considerably limited by strong beam attenuation due to interactions with the aqueous environment. First experiments at synchrotron sources using supported model membranes showed that the microfluidic setup yields a very effective solution for minimizing background scattering and beam absorption, which are often accompanied by radiation damage of biological samples. Additionally, the setup is also well suited for the application of fluorescence microscopy. The application of these two different techniques on the same sample offers unique possibilities for complementary studies.

Permanent weblink:
http://dx.doi.org/10.1063/1.2040187

A microfluidic setup for studies of solid-liquid interfaces using x-ray reflectivity and fluorescence microscopy

Christian Reich and Marion B. Hochrein
Department für Physik der Ludwig-Maximilians-Universität München, Geschwister-Scholl-Platz 1, D-80539 München, Germany

Bärbel Krause
European Synchrotron Radiation Facility, Boite Postale 220, F-38043 Grenoble Cedex, France

Bert Nickel
Department für Physik der Ludwig-Maximilians-Universität München, Geschwister-Scholl-Platz 1, D-80539 München, Germany

(Received 3 May 2005; accepted 1 August 2005; published online 2 September 2005)

In this paper we present a concept for a microfluidic chamber optimized for x-ray reflectivity studies at solid-liquid interfaces. Experiments of this kind are usually considerably limited by strong beam attenuation due to interactions with the aqueous environment. First experiments at synchrotron sources using supported model membranes showed that the microfluidic setup yields a very effective solution for minimizing background scattering and beam absorption, which are often accompanied by radiation damage of biological samples. Additionally, the setup is also well suited for the application of fluorescence microscopy. The application of these two different techniques on the same sample offers unique possibilities for complementary studies. © *2005 American Institute of Physics.* [DOI: 10.1063/1.2040187]

INTRODUCTION

The organization of biological molecules at solid-liquid interfaces is of central significance in biotechnology and medicine. Typical applications for interfaces between hard matter (metals, semiconductors, ceramics, etc.) and soft matter (polymers, membranes, proteins, etc.) are implants, biosensors, DNA-based microchips, or cell-semiconductor systems. Model systems that retain the properties of real biological interfaces in a liquid environment can be constructed artificially and help to clarify a variety of (bio)physical questions.[1]

A particularly interesting model system is supported lipid membranes,[2] which can be spread on flat hydrophilic substrates such as silicon dioxide. Such membranes show in excess water the fluidity and homogeneity of the biological relevant L_α phase, where lipids are confined in a two-dimensional membrane matrix, but free to diffuse laterally on the membrane surface.[3] Supported membranes are interesting systems for various scientific questions, e.g., cell-cell signaling or protein targeting and trafficking.[4]

Such interfaces can be investigated on the nanometer scale using surface-sensitive techniques such as x-ray reflectivity. It allows a precise determination of single layer and multilayer thicknesses, their roughnesses, and electron-density profiles. Complementary information is offered by neutron reflectivity, however, this technique requires relatively large samples and the accessible momentum transfer is strongly limited compared to x-ray reflectivity.[5] Furthermore, methods of biology, such as microscopy, provide only limited spatial information on the molecular scale, therefore structure investigations employing x-ray radiation play an important role for clarifying molecular structures.

Since x rays are highly incoherently scattered and/or absorbed in liquids, such studies at liquid interfaces are a very delicate task. Generally, the high attenuation cross section of x rays in liquids limits the signal gain from the interface and is accompanied by radiation damage of the biological sample.[6]

In this paper we present a compact microfluidic sample chamber optimized for x-ray studies of biological interfaces such as solid-supported membranes. In contrast to conventional setups with a classical window→water→interface →water→window design,[7,8] our sample chamber is also well suited for microscopy applications without further modification. Fluorescence microscopy can be used for optical sample characterization, e.g. a verification of the phase state of thin films.

The outline is as follows: In Sec. I, the technical specifications of our sample chamber are introduced. Section II demonstrates the feasibility of the microfluidic chamber for fluorescence microscopy. For this purpose, a lipid membrane composed of 1,2-dioleoyl-*sn*-glycero-3-phosphatidylcholine (DOPC) was deposited on a silicon dioxide wafer in the sample chamber. The homogeneity and fluidity of the supported membrane were inspected. Section III reviews the relevant x-ray interaction cross sections and motivates the choice for the optimal energy for x-ray studies. In Sec. IV, the results of the synchrotron reflectivity experiments are presented together with a discussion of radiation damage effects. A summary follows in Sec. V.

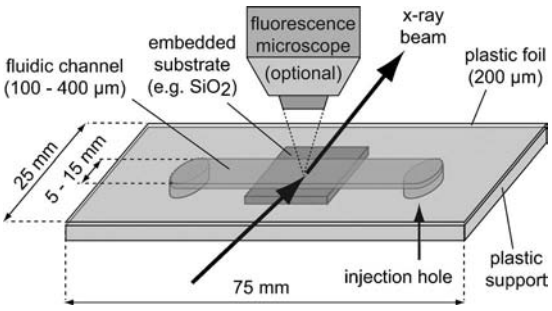

FIG. 1. Sketch of the microfluidic chamber. The x-ray beam geometry is indicated. As an option, the interface can be investigated optically using fluorescence microscopy.

I. CHAMBER DESIGN

Our setup consists of a plastic chamber with a microchannel (Fig. 1). Small absolute dimensions (width 25 mm, length 75 mm) minimize the beam path through attenuating media (chamber walls, channel liquid) and thus the absorption and background, originating from incoherent scattering. The chamber material is a cyclic olefin copolymer (COC), a commercially available engineering thermoplastic (Ticona, Frankfurt, Germany). It is an optical transparent amorphous polymer with low mass density ($\rho=1.02$ g/cm^3) and therefore low absorption for x rays. COC is constituted mainly of CH_2 monomers and hydrophobic with strong resistance and/or inertness against water, acids, bases, and organic solvents such as 2-propanol. It dissolves only in unpolar solvents, such as toluene and hexane, that are rarely used in microfluidic or biological applications.

The support of the microfluidic chamber is manufactured by injection molding. Such supports are commercially available from ibidi, München, Germany. A channel of variable thickness (100–400 μm, width 5–15 mm) is molded mechanically into the support. A further cavity is milled into the center of the support with a variable area from 10×10 to 20×20 mm^2 and a depth of 0.5 mm. The substrate (e.g., a silicon wafer of approximately 0.5 mm thickness) is embedded into this cavity and fixed on the backside using a two-component glue. The surface of the wafer is on a level with the bottom of the channel. The microchannel is sealed at the top by a bonded COC foil (200 μm thickness) of high mechanical rigidity. COC has a high transparency for visible light,[9] a fact that allows microscopy experiments through the thin top foil.

The silicon wafer inside the chamber acts as a well-defined substrate with very low roughness, which can be (bio)functionalized in a variety of ways, e.g., by surface patterning or coating with thin polymer films.[10–12]

The small pots at the channel endings represent injection holes for sample preparation and liquid exchange. These pots can be accessed using pipettes, syringes, or even sophisticated liquid exchange systems. The channel volume ranges from 25 to 300 μl, depending on the choice of channel dimensions. The microchannel reduces the amount of biological material (e.g., liquids, lipid-peptide mixtures, etc.) necessary for sample preparation. After preparation, the pots are sealed with plastic lids.

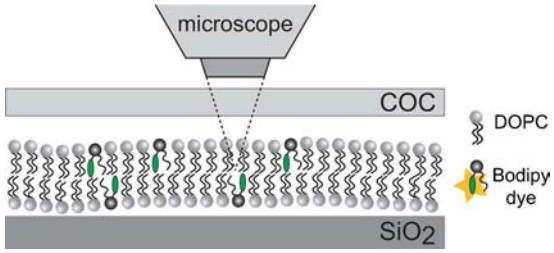

FIG. 2. Experimental scheme for fluorescence microscopy. Light emitted from the fluorescent dye is observed through the thin top foil.

II. FLUORESCENCE MICROSCOPY

Fluorescence microscopy is a standard tool for optical characterization of biological systems on the μm scale. Lipid membranes can be visualized by labeling with small concentrations of fluorescent dyes, which only negligibly alter the properties of the system (Fig. 2). By observing the fluorescence from such a labeled membrane it is possible to inspect its homogeneity and fluidity. A high fluidity guarantees that the membrane is intact on a molecular scale. The fluidity is measured above the phase-transition temperature T_m of the lipid membrane, at which the structure changes from the crystalline, rigid L_β phase to the amorphous, fluid L_α phase.

Fluorescence microscopy experiments in the vicinity of strongly reflecting surfaces such as silicon have to take into account the effect of fluorescence quenching:[13] Near a bare silicon surface, reflection and interference of the fluorescence results in standing light waves. The boundary conditions at the interface enforce the formation of a wave knot (destructive interference). Hence the fluorescence intensity is almost zero close to bare silicon. Therefore our substrate consists of a polished silicon wafer covered on top by a thermally oxidized SiO_2 layer of 400 nm thickness. The substrate was cleaned using the method described in Ref. 14 and afterwards embedded into the plastic chamber. The channel had a thickness of 200 μm and a width of 5 mm.

A lipid membrane [composition 99.95% 1,2-dioleoyl-*sn*-glycero-3-phosphatidylcholine (DOPC, $T_m=-20$ °C) and 0.05% β-Bodipy dye, Avanti Polar Lipids, Alabaster, Alabama, USA] was prepared on the substrate (20×20 mm^2) by spreading lipid vesicles on the hydrophilic surface of SiO_2 (Refs. 15 and 16): Small unilamellar lipid vesicles dispersed in pure water (concentration 1 mg/ml) were injected into the channel and incubated for 3 h at room temperature. During incubation, vesicles spread on the hydrophilic surface and form a single homogeneous membrane across the substrate.[17] Afterwards the channel was flushed with deionized pure water (Milli-Q, specific resistivity 18.2 MΩ cm, Millipore Corp., Billerica, Massachusetts) in order to remove excess vesicles.

The homogeneity and fluidity in an aqueous environment is inspected on a nontransparent substrate using a modified continuous bleaching technique[18]:

A roughly circular spot of 230 μm diam is illuminated while the rest of the membrane is left in the dark. Within the bright region the homogeneity of the membrane can be examined. With time, the fluorescence signal of the membrane decays exponentially in the illuminated area as expected for

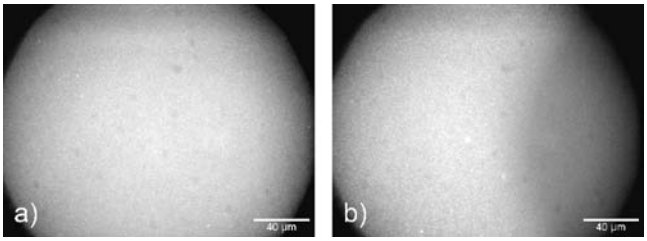

FIG. 3. Fluorescence images of a fluid lipid membrane on SiO_2. (a) Image of a homogeneous lipid membrane. The white bar represents 40 μm. (b) A second image, displaying the former borderline. A continuous, nonsharp transition from the previously nonilluminated to the previously illuminated area is clearly visible.

a large ensemble of continuously exited dyes. Dye molecules cannot be excited consecutively on long time scales, since there is always a certain probability that the molecules chemically react upon illumination. After such a process, the dye is irreversibly bleached.

Figure 3(a) shows a fluorescence image of a lipid membrane taken with a 40× objective on an Axiovert 100M microscope (numerical aperture 0.75, Plan-Neofluar series, Carl Zeiss, Oberkochen, Germany). The membrane shows a spatially homogeneous fluorescence signal. After several seconds of continuous illumination (or bleaching), the sample was translated laterally for about 100 μm and a second picture was taken, showing the borderline between the previously illuminated and nonilluminated area, see Fig. 3(b). If the lipid membrane is immobile, a sharp drop of the fluorescence intensity at the borderline is expected. But in case the lipid membrane is fluid, the intensity will decrease steadily from the former nonilluminated to the former illuminated area, due to lateral diffusion of unbleached fluorescently labeled lipids. The size of the transition area is directly proportional to the diffusion constant.

The homogeneity of the membrane is clearly seen as well as the borderline between the previously bleached and unbleached regions. The borderline is significantly smeared out due to lipid diffusion. It confirms that we were able to produce a supported membrane of good quality on SiO_2 proving that the surface is neither chemically nor physically degraded by the manufacturing process of our chamber.

III. X-RAY ENERGY SELECTION

The interaction of x rays with matter is dominated by high photoabsorption for commonly used x-ray energies around 10 keV. This fact complicates x-ray studies from buried interfaces significantly. The choice of the optimal x-ray energy should take into account three closely related aspects. First of all, transmission through the chamber material and the liquid (H_2O) should be of the order of 10% or more. Second, beam damage caused by incoherent scattering processes, which is always considered a serious problem with complex biomolecules, should be minimal. Third, the coherent cross section giving rise to the diffraction signal from the interface should be high.

A detailed Monte Carlo simulation of the optimal x-ray energy taking into account the different coherent and incoherent cross sections of typical atomic concentrations, in,

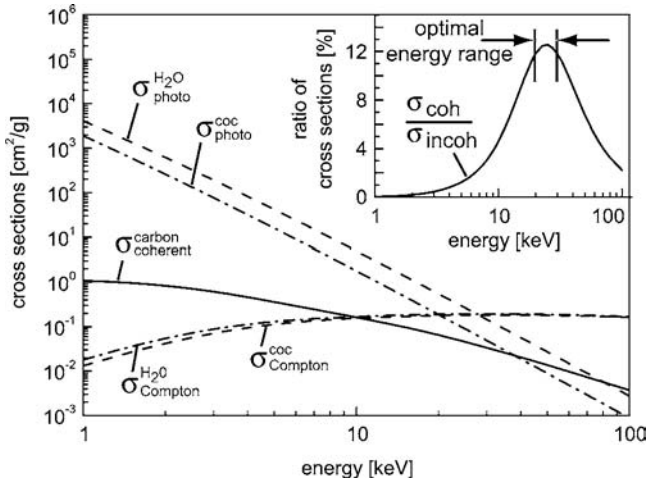

FIG. 4. X-ray interaction cross sections. The coherent cross section is plotted for carbon. The Compton and photocross sections for COC and H_2O are also indicated. The inset shows the cross-section ratio $\sigma_{coh}/\sigma_{incoh}$.

e.g., proteins, is a work in progress.[19] In a simplified approach, we assume an interface composed of organic constituents embedded in a liquid water environment. The cross sections for this case are summarized in Fig. 4.[20,21]

We assume the coherent cross section of carbon (σ_{coh}) as the relevant signal from the interface and estimate the incoherent contribution as the weighted sum of photo scattering and Compton scattering from the bulk. Based on the design of the sample cell (see Sec. IV), the beam passes through 20 mm of COC and 5 mm of H_2O (total beam path 25 mm), i.e., $\sigma_{incoh}=0.8\sigma_{photo+Compton}(COC)+0.2\sigma_{photo+Compton}(H_2O)$. The ratio of the cross sections $\sigma_{coh}/\sigma_{incoh}$ indicates a favorable energy range around 20 keV for low-Z material (inset of Fig. 4). This is a reasonable approximation in our specific case, since our compact microfluidic design limits the overall beam attenuation by the sample environment to less than one order of magnitude. The calculation of the attenuation is presented in detail for an x-ray energy of 20 keV in Sec. IV.

IV. SYNCHROTRON EXPERIMENTS

The feasibility of the proposed concept for x-ray reflectivity was tested at the Hamburger Synchrotronstrahlungslabor (HASYLAB) in Hamburg, Germany (bending magnet beamline D4) and the European Synchrotron Radiation Facility (ESRF) in Grenoble, France (undulator beamline ID01). Microfluidic devices with the same specifications as described in Sec. II were used (Fig. 5). The employed x-ray energy at HASYLAB was $E=20$ keV and the beam cross section was limited by a presample aperture of 0.05×2 mm^2 (vertical × horizontal). At ESRF, the photon energy was $E=19.5$ keV and the presample aperture consisted of 0.02×0.2 mm^2 ($v\times h$). The grazing-incidence x-ray beam effectively illuminated a surface area comparable to the focal spot of the fluorescence microscope shown in Fig. 3, which is roughly $(0.23\text{ mm}/2)^2\pi\approx0.2\times0.2$ mm^2.

In principle, the chamber can be mounted on the sample table in a horizontal or vertical scattering geometry. For the experiments presented here, the horizontal setup was em-

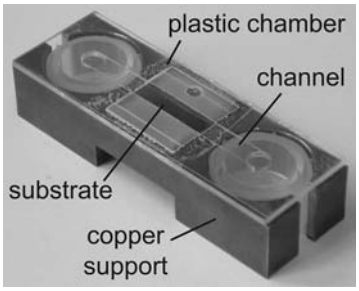

FIG. 5. Microfluidic chamber with 200 μm channel and an embedded 20 $\times 20$ mm^2 wafer, as used for the microscopy and synchrotron experiments. The plastic chamber is mounted on a copper support.

ployed with the beam impinging from the short side of the chamber in order to minimize the beam path through matter.

For reflectivity experiments, the solid-liquid interface must be positioned exactly in the center of rotation (θ angle) of the sample table. In order to properly identify the interface, the attenuation profile of an air-filled chamber was recorded as a function of sample height by a vertical scan of the chamber along the z coordinate (Fig. 6).

The low beam attenuation through the chamber material is evident. The vertical beam sizes of 50 μm and 20 μm at HASYLAB and ESRF, respectively, proved sufficient to clearly identify the position of the SiO_2 surface. It allowed a precise assignment of the interface to the center of rotation of the diffractometer (sketch in Fig. 7), which is crucial for the necessary alignment procedures.[22] The small beam size, together with a high detector collimation, ensured that the reflected intensity from the top COC foil was entirely suppressed.

Reflectivity at the water/SiO_2 interface

The refractive index is defined as $n=1-\delta+i\beta$, with the dispersion δ and the absorption β. The critical angle for total external reflection at an interface is

$$\cos(\theta_{\mathrm{crit}}) = \frac{n_2}{n_1} \approx \frac{1-\delta_2}{1-\delta_1} \quad \text{for } n_2 < n_1, \tag{1}$$

neglecting the small absorption contribution. Using small-angle approximations, the critical angle becomes

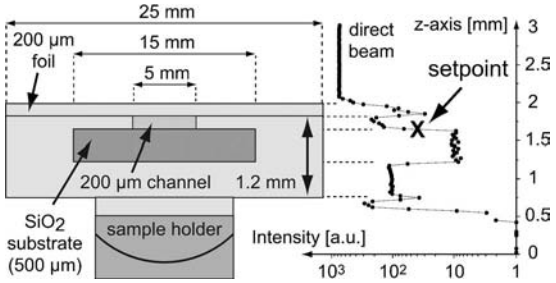

FIG. 6. Attenuation profile along the z axis (sample height). For a proper alignment, the beam must be positioned to illuminate the interface of interest (here: setpoint at the air/SiO_2 interface). Data recorded at HASYLAB.

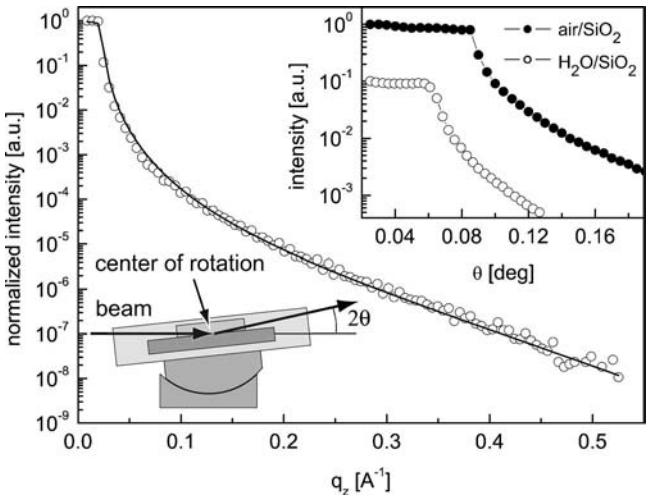

FIG. 7. Normalized reflectivity from the water/SiO_2 interface in a chamber with 200 μm channel, recorded up to an incidence angle of $\theta=1.5°$. The inset shows clearly the shift of the critical angle from the air/SiO_2 to the water/SiO_2 interface. The data is presented with a vertical offset for clarity.

$$\theta_{\mathrm{crit}} \approx \sqrt{2(\delta_2 - \delta_1)}. \tag{2}$$

This formula yields critical angles of $\theta_c=0.089°$ for the air/SiO_2 interface and $\theta_c=0.065°$ for the water/SiO_2 interface, assuming an x-ray energy of 20 keV.

Reflectivity experiments at the air/SiO_2 interface and the water/SiO_2 interface (measured with the same chamber after filling with water) reveal critical angles of $\theta_c \approx 0.085°$ and $\theta_c \approx 0.060°$, respectively, in good agreement with the calculated values (see Fig. 7).

The reflectivity data from HASYLAB covers about eight orders of magnitude in intensity, which represents an achievable momentum transfer of up to $q_z=0.5$ Å^{-1} (Fig. 7). It should be pointed out that the small-angle-scattering signal from the chamber material (COC) has a characteristic peak at $q=1.21$ Å^{-1} (Ref. 23). Thus the reflectivity signal is not influenced in the momentum-transfer range reported here.

A quantitative data evaluation using the Parratt algorithm[24,25] gives an average roughness of $\sigma \approx 3.5$ Å for the SiO_2 surface. The solid line in Fig. 7 represents the corresponding fitted curve. The data analysis takes into account the correction for background, footprint, and beam attenuation. The attenuation correction is more complicated than in the case of standard setups, where the beam usually enters through negligibly thin windows (e.g., Kapton) and strikes an interface facing a bulk water reservoir.[7,8] In fact, the beam path through the chamber material is angle dependent. The coherent scattered intensity from the buried interface is reduced by beam attenuation as a function of the grazing incidence angle θ. As a result, we gain a *reduced* coherent intensity

$$I = I_{\mathrm{coh}} \exp\left[-2\frac{d(\theta)}{\xi_{H_2O}} - 2\frac{l(\theta)-d(\theta)}{\xi_{\mathrm{COC}}} \right]. \tag{3}$$

The beam paths l and d through the chamber are illustrated in Fig. 8. ξ is the energy- and material-dependent attenuation length.

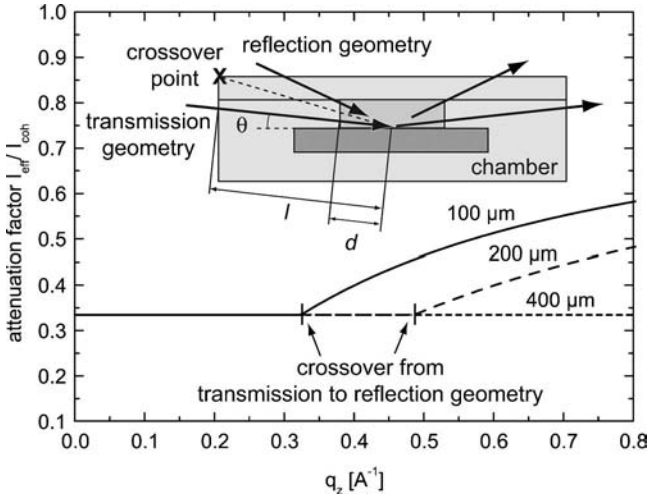

FIG. 8. Calculated beam attenuation (correction factor) as a function of momentum transfer for different channel thicknesses. Two regimes (transmission and reflection geometry) are distinguished, separated by the chamber edge. The crossover point is indicated. The sketch shows the pathway of the beam through the chamber. The total beam path through matter decreases with growing incidence angle, inducing a lower attenuation.

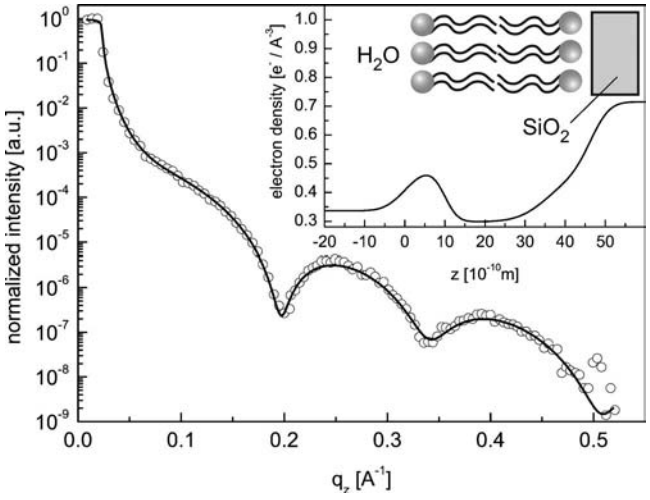

FIG. 9. Reflectivity of a lipid bilayer adsorbed on SiO_2. The solid line is a fit corresponding to the electron-density profile shown in the inset. The data is corrected for background, beam attenuation, and footprint.

For determining the attenuation factor (I/I_{coh}), the overall path has to be calculated as a function of incidence angle. For small angles, the beam impinges the chamber from the side (transmission geometry) while for larger angles the beam enters from the top (reflection geometry). These adjacent regimes have to be distinguished.

We define the channel width a and the overall chamber width b. Further, h is the channel thickness and f the foil thickness. The path d through water and the path $l-d$ through the plastic chamber are defined separately for transmission (d_1, l_1) and for reflection (d_2, l_2). Thus we get $d_1 = a/2 \cos\theta$, $l_1 = b/2 \cos\theta$, and accordingly, $d_2 = a/2 \cos\theta$, $l_2 = (f+h)/\sin\theta$. The calculated attenuation profiles for 100, 200, and 400 μm channels are plotted in Fig. 8, assuming the following values: $a = 5$ mm, $b = 25$ mm, and $c = 15$ mm. The corresponding attenuation lengths for a photon energy of 20 keV are $\xi_{H_2O} = 14.25$ mm and $\xi_{COC} = 26.88$ mm. The raw data (I) has to be divided by the attenuation factor in order to extract I_{coh}.

In any case, the loss of intensity is less than one order of magnitude due to the compact chamber geometry.

Reflectivity of supported membranes on SiO_2

A single DOPC membrane was deposited on the embedded SiO_2 substrate using the procedure and composition described in Sec. II. Reflectivity scans of the interface with the supported membrane were performed at ESRF. Biomolecules such as lipids are very sensitive to radiation damage due to the high-flux x-ray beam, a fact that has to be considered particularly during synchrotron measurements. Therefore automatic attenuators in front of the sample were used in order to reduce exposure to the full beam intensity of approximately $2-5\times10^{10}$ photons/s. Data sets were always recorded on fresh spots on the interface which were not previously illuminated during alignment procedures. An automatic shutter system ensured that the sample was not unnecessarily exposed to the beam during motor movements (positioning of the θ and 2θ angle).

The reflectivity data (Fig. 9) show characteristic oscillations, indicating the presence of a lipid membrane above the substrate. An exposure time of 1 s/collected data point proved sufficient for recording the reflectivity (100 points in total) up to a momentum transfer of $q_z = 0.5$ Å^{-1}. The electron-density profile of a lipid bilayer on SiO_2 was modeled using a simple three-box model. In detail, the bilayer is separated into a lipid headgroup facing the water (density $\rho_{head} = 0.484\ e^-/$Å^3, thickness $d = 10.3$ Å, and roughness $\sigma = 4.10$ Å), the hydrocarbon chains ($\rho_{chains} = 0.307\ e^-/$Å^3, $d = 27.3$ Å, $\sigma = 2.52$ Å), and a lipid headgroup facing the silicon oxide ($\rho_{head} = 0.636\ e^-/$Å^3, $d = 9.53$ Å, $\sigma = 6.36$ Å). The profile is shown in the inset of Fig. 9. The calculated reflectivity of this model fits the data accurately (solid line in Fig. 9). The reported parameters are in excellent agreement with electron densities extracted from oriented multilayer stacks.[26]

It is a present field of debate whether supported lipid bilayer fluidity relies on the presence of a very thin water layer ($\sim$ some Å) confined to the silicon oxide interface. However, it was not necessary to introduce such a water layer in order to reproduce adequately our data. Further high-resolution measurements (which even exceed the wide momentum-transfer range presented here) together with more sophisticated refinement techniques, e.g., Ref. 27, would be necessary to clarify this question in an adequate manner.

Radiation damage

During our experiments we found that a continuous illumination of the membrane interface with the full intensity available at ESRF caused a significant altering of the reflectivity signal. As the most striking effect, we observed a shift of the positions of the characteristic minima at $q_z = 0.198$ and 0.340 Å^{-1} towards higher q_z values with increasing exposure time, see Fig. 10(a).

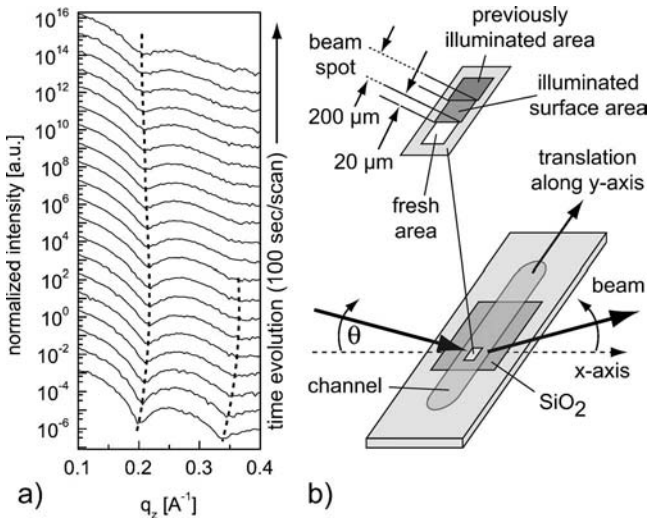

FIG. 10. (a) Radiation damage: time evolution of the specular reflected intensity near the initial positions of the minima at q_z=0.198 and 0.340 Å^{-1}. (b) The sketch illustrates an alternative procedure for recording a reflectivity curve. Note that the illuminated surface area decreases with growing incidence angle.

We have recorded a set of reflectivity curves on a single surface spot in the region around the first and second minima (0.1 Å^{-1} $< q_z <$ 0.4 Å^{-1}) in order get an estimate for the time evolution of the effect. Under the corresponding grazing angles ($0.29° < \theta < 1.16°$), the beam illuminated an area on the interface from 4.0×0.2 mm^2 to 1.0×0.2 mm^2, respectively, as illustrated in Fig. 10(b). The sample was illuminated consecutively for 100 s/scan. No beam attenuators were used.

We observed a nonlinear shift of the minima positions [Fig. 10(a), dotted line] along with a smearing of the minima. We ascribe this effect to partial damaging of the membrane due to the high-flux beam, resulting in a decrease of surface coverage within the irradiated spot. It is obvious that such a characteristic mutation of the signal may easily lead to wrong data evaluation. Therefore experiments on biological interfaces using high-flux synchrotron sources must be prepared and performed very carefully.

Additional measurements performed at HASYLAB confirm the data presented in Fig. 9 with high accuracy. Analogous sets of reflectivity scans (not shown here) do not show variations of the signal, even after exposure times of several hours. The scans employed a maximal flux of approximately 10^8 photons/s and the beam illuminated a significantly larger surface area. Nevertheless the necessary counting time per scan at HASYLAB is significantly higher than at ESRF. Furthermore the characteristic features of the reflectivity at high momentum transfers are much more distinct in the ESRF data.

A further strategy for minimizing radiation effects is to illuminate for each data point a new area on the membrane surface. Several reflectivity curves (100 data points each) were recorded at ESRF by laterally shifting the impinging beam on the sample. The translation occurred along the y axis, which is perpendicular to the direction of the incident beam (x axis). The step size of the y shift was 20 μm per data point, so that each contributing area was illuminated for a maximum of 10 s. The principle is illustrated in Fig. 10(b). In order to ensure a proper alignment during such a translation scan, we carefully checked the correct position of the specular peak at the start-, middle-, and endpoint prior to each scan. This procedure together with the use of automatic attenuators reduces radiation effects below the observable limit. Of course, it requires that the surface is homogeneously covered over wide areas, as can be verified by fluorescence microscopy.

V. SUMMARY

Studies of buried interfaces using synchrotron x rays with high brilliance and sophisticated experimental setups[28,29] are becoming highly competitive in fields formerly dominated by neutron scattering. Our measurements performed at HASYLAB and ESRF demonstrate the feasibility of microfluidic chambers for x-ray reflectivity using synchrotron radiation. The problem of radiation damage, often mentioned as the principal disadvantage compared to neutron reflectivity, must nevertheless always be considered depending on the type of sample interface. Sample damage can be minimized significantly by choosing a favorable energy, a moderate exposure of the sample to just the necessary flux, and by recording the data sets on different sample spots whenever possible. Using this scheme, high-resolution reflectivity curves from solid-liquid interfaces could be recorded up to a momentum transfer of q_z=0.5 Å^{-1} until reaching the background level. This represents a far higher q_z range than achievable with comparable neutron-reflectivity experiments.[30]

The small beam path through the chamber, together with a relatively large interface area accessible by the grazing-incidence beam, makes the setup particularly promising for diffuse scattering studies. Using grazing-incidence small-angle scattering techniques, lateral structures of membranes such as chain-chain distances of lipid molecules[31] and membranes with incorporated peptides and proteins,[32] should be resolvable with high resolution.

The additional microscopy option allows to employ a single setup for investigations both with surface x-ray diffraction techniques and optical microscopy methods. The combination of these two different but highly complementary experimental tools on a single sample is unique.

ACKNOWLEDGMENTS

The authors would like to thank R. Zantl from ibidi GmbH, München, Germany for fruitful discussions and for supplying the plastic supports of the microfluidic chambers. The authors also thank T.H. Metzger (ESRF) and O. Seeck (HASYLAB) for continuous support during the synchrotron experiments. This work was supported by the Deutsche Forschungsgemeinschaft (Grant No. SFB 563).

[1] M. Tirrell, E. Kokkoli, and M. Biesalski, Surf. Sci. **500**, 61 (2002).
[2] E. Sackmann, Science **271**, 43 (1996).
[3] S. J. Singer and G. L. Nicolson, Science **175**, 720 (1972).
[4] K. Simons and E. Ikonen, Nature (London) **387**, 569 (1997).
[5] J. Generosi, C. Castellano, D. Pozzi, A. C. Castellano, R. Felici, F. Natali, and G. Fragneto, J. Appl. Phys. **96**, 6839 (2004).

[6] V. Cherezov, K. M. Riedl, and M. Caffrey, J. Synchrotron Radiat. **9**, 333 (2002).
[7] C. E. Miller, J. Majewski, T. Gog, and T. L. Kuhl, Phys. Rev. Lett. **94**, 238104 (2005).
[8] M. Vogel, C. Münster, W. Fenzl, and T. Salditt, Phys. Rev. Lett. **84**, 390 (2000).
[9] G. Khanarian, Opt. Eng. (Bellingham) **40**, 1024 (2001).
[10] T. Rohr, D. F. Ogletree, F. Svec, and J. M. J. Fréchet, Adv. Funct. Mater. **13**, 264 (2003).
[11] P. Lenz, C. M. Ajo-Franklin, and S. G. Boxer, Langmuir **20**, 11092 (2004).
[12] E. Sackmann and M. Tanaka, Trends Biotechnol. **18**, 58 (2000).
[13] D. Braun and P. Fromherz, Phys. Rev. Lett. **81**, 5241 (1998).
[14] W. Kern and D. A. Puotinen, RCA Rev. **31**, 187 (1970).
[15] A. A. Brian and H. M. McConnell, Proc. Natl. Acad. Sci. U.S.A. **81**, 6159 (1984).
[16] E. Kalb, S. Frey, and L. K. Tamm, Biochim. Biophys. Acta **1103**, 307 (1992).
[17] J. Nissen, K. Jacobs, and J. O. Rädler, Phys. Rev. Lett. **86**, 1904 (2001).
[18] C. Dietrich, R. Merkel, and R. Tampe, Biophys. J. **72**, 1701 (1997).
[19] M. Zahnder, I. Vartaniants, and E. Weckert (private communication).
[20] M. Berger, J. Hubbell, S. Seltzer, J. S. Coursey, and D. S. Zucker, Photon Cross Sections Database (XCOM), NIST.
[21] J. Hubbell, Int. J. Appl. Radiat. Isot. **33**, 1269 (1982).
[22] V. Holý, U. Pietsch, and T. Baumbach, *High-Resolution X-Ray Scattering from Thin Films and Multilayers*, Springer Tracts in Modern Physics, Vol. 149 (Springer, Berlin, 1999).
[23] T. D. Luccio, B. Nickel, F. Antolini, M. Pentimalli, and L. Tapfer, Mater. Res. Soc. Symp. Proc. **847**, EE13.22 (2004).
[24] L. G. Parratt, Phys. Rev. **95**, 359 (1954).
[25] L. Névot and P. Croce, Rev. Phys. Appl. **15**, 761 (1980).
[26] Y. Liu and J. F. Nagle, Phys. Rev. E **69**, 040901 (2004).
[27] M. Schalke and M. Lösche, Adv. Colloid Interface Sci. **88**, 243 (2000).
[28] H. Reichert, O. Klein, H. Dosch, M. Denk, V. Honkimaki, T. Lippmann, and G. Reiter, Nature (London) **408**, 839 (2000).
[29] H. Reichert, V. Honkimäki, A. Snigirev, S. Engemann, and H. Dosch, Physica B **336**, 46 (2003).
[30] G. Fragneto, T. Charitat, F. Graner, K. Mecke, L. Perino-Gallice, and E. Bellet-Amalrice, Europhys. Lett. **53**, 100 (2001).
[31] A. Spaar and T. Salditt, Biophys. J. **85**, 1576 (2003).
[32] C. Münster, A. Spaar, B. Bechinger, and T. Salditt, Biochim. Biophys. Acta **1562**, 37 (2002).

A.2 Full text of Ref. [2]

Marion B. Hochrein, Christian Reich, Bärbel Krause, Joachim O. Rädler and Bert Nickel

Structure and Mobility of Lipid Membranes on a Thermoplastic Substrate.

Langmuir **22** (2), 538-545 (2006).

Abstract:
Supported lipid membranes constitute one of the most important model systems for cell membranes. The properties of lipid membranes supported by the hydrophobic solid polymer cyclic olefin copolymer (COC) were investigated. Lipid layers consisting of varying amounts of 1,2-dioleoyl-3-trimethylammonium propane (DOTAP, cationic) and 1,2-dioleoyl-*sn*-glycero-3-phosphocholine (DOPC, neutral) prepared by vesicle fusion and solvent exchange were compared. All lipid mixtures coated the COC surface homogeneously forming a fluid membrane as verified by fluorescence microscopy and fluorescence recovery after photobleaching (FRAP). The exact structure of the supported membranes was determined by synchrotron reflectivity experiments using a microfluidic chamber. The X-ray data are in agreement with a compressed (head-to-head distance = 29 Å) and less densely packed bilayer.

Permanent weblink:
http://dx.doi.org/10.1021/la051820y

Table of contents graphic:

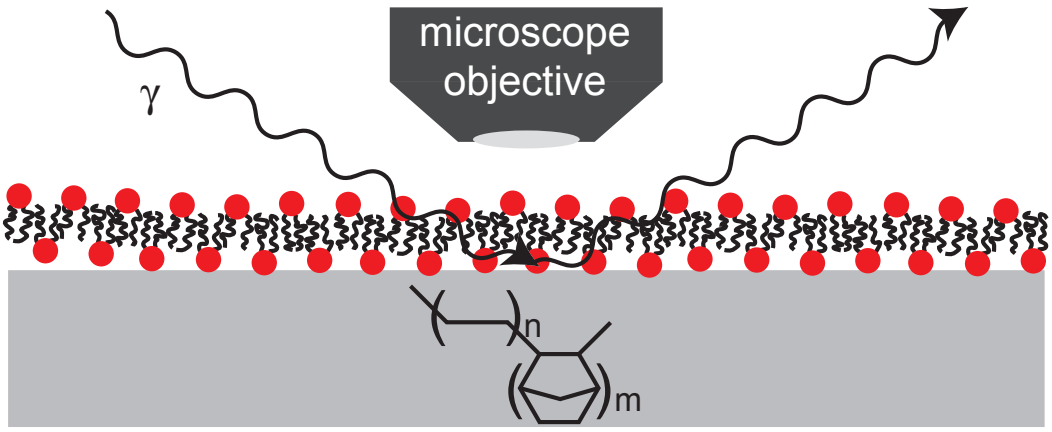

Structure and Mobility of Lipid Membranes on a Thermoplastic Substrate

Marion B. Hochrein,*,† Christian Reich,† Bärbel Krause,‡ Joachim O. Rädler,† and Bert Nickel†

Department für Physik, Ludwig-Maximilians-Universität München, Geschwister-Scholl-Platz 1, 80539 München, Germany, and European Synchrotron Radiation Facility, Boite Postale 220, 38043 Grenoble Cedex, France

Received July 6, 2005. In Final Form: September 23, 2005

Supported lipid membranes constitute one of the most important model systems for cell membranes. The properties of lipid membranes supported by the hydrophobic solid polymer cyclic olefin copolymer (COC) were investigated. Lipid layers consisting of varying amounts of 1,2-dioleoyl-3-trimethylammonium propane (DOTAP, cationic) and 1,2-dioleoyl-*sn*-glycero-3-phosphocholine (DOPC, neutral) prepared by vesicle fusion and solvent exchange were compared. All lipid mixtures coated the COC surface homogeneously forming a fluid membrane as verified by fluorescence microscopy and fluorescence recovery after photobleaching (FRAP). The exact structure of the supported membranes was determined by synchrotron reflectivity experiments using a microfluidic chamber. The X-ray data are in agreement with a compressed (head-to-head distance = 29 Å) and less densely packed bilayer.

1. Introduction

Cells are surrounded by a plasma membrane that protects the cell interior from its environment while still transducing signals necessary for cell functioning. Solid-supported fluid lipid bilayers[1] serve as one of the most important model systems for cell membranes. They allow the application of several surface-sensitive techniques such as ellipsometry, surface plasmon spectroscopy, atomic force microscopy (AFM),[2] and neutron and X-ray reflectivity.[3,4] Hence, structural details of membranes on a solid support that are not accessible to this extent for other model systems can be obtained.

Supported membranes represent an effective way of generating biofunctional surfaces, e.g., for biosensor applications.[5,6] Furthermore, supported fluid positively charged membranes can be used for the manipulation of single biomolecules such as DNA.[7,8,9]

Note that the fluidity of the membrane is a basic requirement for mimicking functional membranes.[1] The proper choice of the supporting substrate is crucial to ensure a fluid supported membrane. Standard supports, including glass cover slides,[10] quartz substrates,[11] oxidized silicon wafers,[12,13] and mica,[14] are hydrophilic and negatively charged. The charge density and the surface chemistry are highly dependent on the cleaning procedure and change with time. Surface modification and structuring is time-consuming and often requires clean-room equipment. Plastic materials can be easily formed at low cost to manifold shapes to comply with different needs. For technical and industrial applications, it is therefore appealing to use plastic materials as support. Studies of the behavior of lipid membranes supported on plastic materials such as poly(dimethylsiloxane) (PDMS)[15] and polystyrene (PS)[16] have been performed previously indicating that fluid membranes can also be formed on plastic supports.

Here, we study the hydrophobic copolymer 2-norbornene ethylene ("cyclic olefin copolymer", COC). COC is a very promising plastic material because it is inert against most acids, bases, and polar solvents and it does not swell in water.[17] Its surface chemistry is robust, e.g., it is independent of the cleaning procedure used and does not vary after exposure to air due to aging effects. Also, COC is basically uncharged. Its high optical transmission, low amount of inclusions, and low autofluorescence[18] make it well-suited for high-resolution fluorescence microscopy. Various kinds of functional microfluidic chambers can be formed from this material by injection molding, nanoimprinting,[19] and surface functionalization.[20]

In this article, we studied the homogeneity, fluidity, and structure of cationic 1,2-dioleoyl-3-trimethylammonium propane (DOTAP)/zwitterionic 1,2-dioleoyl-*sn*-glycero-3-phosphocholine (DOPC) lipid layers supported on COC. We have chosen DOTAP/DOPC mixtures because these lipids have been well-characterized in previous studies.[21−24] Two preparation techniques were compared: the well-established vesicle-fusion method[25] and the

* Corresponding author. E-mail: marion.hochrein@physik.uni-muenchen.de.
† Ludwig-Maximilians-Universität München.
‡ European Synchrotron Radiation Facility.

(1) Yamazaki, V.; Sirenko, O.; Schafer, R. J.; Groves, J. T. *J. Am. Chem. Soc.* **2005**, *127*, 2826−2827.
(2) Sackmann, E. *Science* **1996**, *271*, 43−48.
(3) Fragneto, G.; Charitat, T.; Bellet-Amalric, E.; Cubitt, R.; Graner, F. *Langmuir* **2003**, *19*, 7695−7702.
(4) Vogel, M.; Munster, C.; Fenzl, W.; Salditt, T. *Phys. Rev. Lett.* **2000**, *84*, 390−393.
(5) Cornell, B. A.; BraachMaksvytis, V. L. B.; King, L. G.; Osman, P. D. J.; Raguse, B.; Wieczorek, L.; Pace, R. J. *Nature* **1997**, *387*, 580−583.
(6) Ziegler, C.; Gopel, W. *Curr. Opin. Chem. Biol.* **1998**, *2*, 585−591.
(7) Maier, B.; Rädler, J. O. *Phys. Rev. Lett.* **1999**, *82*, 1911−1914.
(8) Maier, B.; Rädler, J. O. *Macromolecules* **2000**, *33*, 7185−7194.
(9) Olson, D. J.; Johnson, J. M.; Patel, P. D.; Shaqfeh, E. S. G.; Boxer, S. G.; Fuller, G. G. *Langmuir* **2001**, *17*, 7396−7401.
(10) Cremer, P. S.; Boxer, S. G. *J. Phys. Chem. B* **1999**, *103*, 2554−2559.
(11) Kalb, E.; Frey, S.; Tamm, L. K. *Biochim. Biophys. Acta* **1992**, *1103*, 307−316.
(12) Puu, G.; Gustafson, I. *Biochim. Biophys. Acta: Biomembranes* **1997**, *1327*, 149−161.
(13) Reimhult, E.; Hook, F.; Kasemo, B. *Phys. Rev. E* **2002**, *66*.
(14) Mou, J. X.; Yang, J.; Shao, Z. F. *J. Mol. Biol.* **1995**, *248*, 507−512.
(15) Lenz, P.; Ajo-Franklin, C. M.; Boxer, S. G. *Langmuir* **2004**, *20*, 11092−11099.
(16) Elliott, J. T.; Burden, D. L.; Woodward, J. T.; Sehgal, A.; Douglas, J. F. *Langmuir* **2003**, *19*, 2275−2283.
(17) Nielsen, T.; Nilsson, D.; Bundgaard, F.; Shi, P.; Szabo, P.; Geschke, O.; Kristensen, A. *J. Vac. Sci. Technol. B* **2004**, *22*, 1770−1775.
(18) Khanarian, G.; Celanese, H. *Opt. Eng.* **2001**, *40*, 1024−1029.
(19) Monkkonen, K.; Lautanen, J.; Kettunen, V.; Leppanen, V. P.; Pakkanen, T. T.; Jaaskelainen, T. *J. Mater. Chem.* **2000**, *10*, 2634−2636.
(20) Rohr, T.; Ogletree, D. F.; Svec, F.; Frechet, J. M. J. *Adv. Funct. Mater.* **2003**, *13*, 264−270.
(21) Clausen-Schaumann, H.; Gaub, H. E. *Langmuir* **1999**, *15*, 8246−8251.

10.1021/la051820y CCC: $33.50
Published on Web 12/13/2005

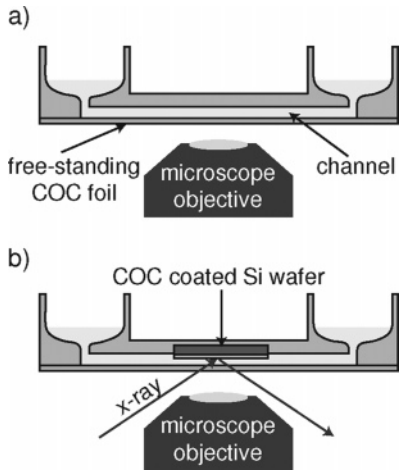

Figure 1. Microfluidic chambers: (a) Schematic drawing of the plastic chamber used for microscopy (side view). (b) Modified chamber for the X-ray measurements (side view). This setup also allowed fluorescence microscopy to be used to optically characterize the sample. The microscope objective shown here was not present during reflectivity experiments.

method of solvent exchange.[26] First, the homogeneity and fluidity of the supported membranes were optically characterized with fluorescence microscopy, continuous bleaching, and fluorescence recovery after photobleaching. Finally, the structure of COC-supported DOPC membranes was resolved by X-ray reflectivity, and the results are discussed.

2. Experiments

2.1. Materials and Methods. *Chemicals.* 1,2-Dioleoyl-3-trimethylammonium propane (DOTAP) and 1,2-dioleoyl-*sn*-glycero-3-phosphocholine (DOPC) were purchased from Avanti Polar Lipids Inc. (Alabaster, AL) and used without further purification. 2-[12-(7-Nitrobenz-2-oxa-1,3-diazol-4-yl)amino]dodecanoyl-1-hexadecanoyl-*sn*-gl ycero-3-phosphocholine (NBD C12-HPC) was purchased from Molecular Probes (Eugene, OR). One percent (w/w) of the fluorescence probe was used to label the membrane. Only freshly bidistilled water (18.2 MΩ, Millipore, Billerica, MA) was used throughout this study. Chloroform, toluene, and 2-propanol of HPLC grade were obtained from Carl Roth GmbH & Co. (Karlsruhe, Germany).

Microfluidic Chambers. The plastic chambers (μ-Slides, ibidi GmbH, München, Germany) consisted of two reservoirs connected by a channel with dimensions $5 \times 0.4 \times 50$ mm^3 (width $\times$ height $\times$ length). The bottom of the channel was sealed using a plastic foil made of the copolymer of 2-norbornene ethylene [cyclic olefin copolymer (COC), Ticona, Frankfurt, Germany]. The high transparency and 0.18-mm thickness of the foil allow for the application of high-resolution optical microscopy (Figure 1a). The microfluidic chambers were cleaned before use by flushing 2 mL of 2-propanol through the flow chamber, followed by at least 20 mL of bidistilled water.

For the X-ray reflectivity measurements, a thin COC film was prepared by spin-coating COC onto a silicon wafer, thus avoiding the long-range undulations present in free-standing foils. A silicon wafer (20×20 mm^2) with a thermally grown oxide layer of 400-nm thickness was cleaned thoroughly for the COC coating by a modified RCA method.[27] In short, the silicon wafer was ultrasonicated for 5 min in each acetone, 2-propanol, and finally water. Afterward, it was boiled at 80 °C in a 1:1:5 $H_2O_2/NH_4OH/H_2O$ mixture. The wafer was shortly rinsed in bidistilled water and then boiled in 1:1:5 $H_2O_2/HCl/H_2O$ at 80 °C. The wafer was dried at 70 °C for 3 h. Three hundred microliters of 10 μg/mL COC dissolved in toluene was deposited onto the wafer, and the wafer was accelerated to 3000 rpm for 2 min. This procedure yielded a homogeneous, smooth COC layer with a thickness of around 450 Å and a surface roughness of 7 Å.

A specially modified chamber was used to embed the silicon wafer as described in detail elsewhere.[28] In brief, the μ-slide was milled open with a square the size of the wafer. The wafer was embedded into the chamber with the COC layer facing toward the channel interior. Finally, the chamber was sealed again with a two-component epoxy glue (Uhu Plus Endfest 300, Uhu GmbH, Bühl, Germany) (Figure 1b). After being allowed to dry for several hours, the chamber was ready for the deposition of the lipids.

Vesicle Fusion (VF). The desired lipid ratio was mixed in chloroform, dried under nitrogen flow, and stored in a vacuum chamber overnight. Bidistilled water was added to the dried lipid to obtain a concentration of 1 mg/mL, and the solution was incubated for 4 h at 50 °C, resulting in multilamellar vesicles. Small unilamellar vesicles were prepared by sonicating the lipid−water mixture in a tip sonicator (Sonoplus UW 2070, Bandelin electronic, Berlin, Germany) for 10 min at an amplitude of 170 μm while the solution was cooled on ice.[29] Four hundred microliters of the lipid solution was deposited into the chamber channel and incubated overnight. The chambers were flushed with at least 100 mL of bidistilled water while avoiding air contact with the lipid layer.

Solvent Exchange (SE). The lipids were mixed and dried as described above. A solution with a concentration of 1 mg/mL was prepared by adding 2-propanol to the dried lipid. Two hundred microliters of the lipid solution was injected into the chamber. Two milliliters of bidistilled water was added into one of the two reservoirs of the chamber, which led to a reduction of the 2-propanol content in the solvent to 10%. After equilibration of the water levels in the two reservoirs, 30 mL of bidistilled water was quickly flushed through the channel to remove excess vesicles and reduce the amount of vesicles adhered to the membrane.

For comparison, a membrane on a hydrogen-terminated silicon wafer (H−Si) was prepared as follows: A DOPC membrane was deposited by spin coating a DOPC−2-propanol solution (1 mg/mL) immediately after a HF etch.[30] Then, the dried sample was placed in the microfluidic chamber and flushed with water prior to the measurement.

X-ray Reflectivity Measurements. All X-ray reflectivity measurements using COC supports were performed at the European Synchrotron Radiation Facility (ESRF) in Grenoble, France, at the beamline ID01. The measurement of a lipid membrane supported by hydrogen-terminated silicon was carried out at the Hamburger Synchrotronstrahlungslabor (Hasylab) (beamline D4, Hamburg, Germany). The X-ray energy was 19.5 keV ($\lambda = 0.636$ Å). Details of the experimental setup are described in Reich et al.[28] Special care was taken to avoid beam damage due to overexposure by shifting the sample during the measurements. Because reflectivity curves could be reproduced with high accuracy during several consecutive scans, we can exclude beam damage. The data were analyzed using the software Parratt32, version 1.5.2 (Christian Braun, HMI Berlin), which uses the Parratt algorithm[31] to calculate the reflectivity data and implements error minimization according to a simplified one-dimensional Newton−Raphson method.[32] Good starting values were needed.

(22) Campbell, R. B.; Balasubramanian, S. V.; Straubinger, R. M. *Biochim. Biophys. Acta: Biomembranes* **2001**, *1512*, 27−39.
(23) Symietz, C.; Schneider, M.; Brezesinski, G.; Mohwald, H. *Macromolecules* **2004**, *37*, 3865−3873.
(24) Rädler, J. O.; Koltover, I.; Salditt, T.; Safinya, C. R. *Science* **1997**, *275*, 810−814.
(25) Brian, A. A.; McConnell, H. M. *Proc. Nat. Acad. Sci. U.S.A.* **1984**, *81*, 6159−6163.
(26) Miller, C.; Cuendet, P.; Grätzel, M. *J. Electroanal. Chem.* **1990**, *278*, 175−192.
(27) Kern, W.; Puotinen, D. A. *Rca Rev.* **1970**, *31*, 187.
(28) Reich, C.; Hochrein, M.; Krause, B.; Nickel, B. *Rev. Sci. Instrum.* **2005**, *76*, 095103.
(29) Barenholz, Y.; Gibbes, D.; Litman, B. J.; Goll, J.; Thompson, T. E.; Carlson, F. D. *Biochemistry* **1977**, *16*, 2806−2810.
(30) Mennicke, U.; Salditt, T. *Langmuir* **2002**, *18*, 8172−8177.
(31) Parratt, L. G. *Phys. Rev.* **1954**, *95*, 359−369.
(32) Press, W.; Flannery, B.; Teukolsky, S.; Vetterling, W. *Numerical Recipes*; Cambridge University Press: Cambridge, U.K., 1986.

Fluorescence Microcopy. The optical appearance of the lipid membranes was judged using an inverted fluorescence microscope (Axiovert 100M, Carl Zeiss, Oberkochen, Germany) equipped with a 100× oil-immersion objective (100 Plan Neofluar, N.A. 1.3, Carl Zeiss, Oberkochen, Germany). Images were captured with a CCD camera (CoolSnap HQ, Photometrics, Roper Scientific Inc., Tuscon, AZ) and analyzed with Igor Pro 4.0 (Wavemetrics, Portland, OR).

Continuous Bleaching. The diffusivity of lipid membranes is determined by continuous bleaching following the method initially developed by Dietrich et al.[33] The field stop of the microscope is closed in such a way that only a roughly circular spot (ø 70 μm) is illuminated while the rest of the membrane is left in the dark.

In the center of the observation area, the fluorescence signal of the membrane decays exponentially as a function of exposure time as expected for a large ensemble of continuously exited dyes

$$I(x{=}d/2,t) = I_{d/2}\mathrm{e}^{-bt} + B \qquad (1)$$

Here, $I(x,t)$ is the intensity; x is the distance from the rim toward the center of the illuminated area; d is the diameter of the field stop; t is the time since the beginning of the exposure; B is the background noise; and b is the bleaching constant, which depends on the brightness of the illumination, the buffer, and the fluorescence molecule used.

At the edge of the illuminated area, two cases have to be taken into account. If the membrane is immobile, a discontinuous jump in the concentration of unbleached dyes forms at the edge of the illuminated area. If the lipid layer is fluid, unbleached fluorescently labeled lipids from the surrounding nonilluminated area diffuse continuously into the illuminated spot, thereby increasing the fluorescence signal at the rim. As a result, a bright halo forms at the periphery of the illuminated area. In this case, the signal decreases approximately exponentially from the dark field stop toward the middle of the observation area

$$I(x,t_0) = I_{t0}e^{-x/\lambda} + B = I_{t0}\mathrm{e}^{-\sqrt{b/D}\cdot x} + B \qquad (2)$$

where λ is the decay length, $D = b/\lambda^2$ is the diffusion constant of the lipid layer, and b is the bleaching constant. Equation 2 holds for x close to the periphery the illuminated area. If x is too large, the decaying fluorescence signal is obscured by the background. It is important that equilibrium between the bleaching process and the diffusion process is established. Care has to be taken that the sample is not bleached too much for obtaining a good signal-to-noise ratio. This holds well for the condition $5 \leq tb \leq 10$.

Fluorescence Recovery after Photobleaching. Fluorescence recovery after photobleaching (FRAP)[34] was measured on a modified inverted microscope (Axiomat, Carl Zeiss, Oberkochen, Germany). The beam ($\lambda = 488$ nm) of a 0.8-W argon laser (Innova 70-4, Coherent Inc., Santa Clara, CA) was split into a bleaching beam and an observation beam such that the intensity of the bleaching beam was more than 1000 times stronger than that of the observation beam. The microscope objective (100× Fluar N.A. 1.3, Carl Zeiss, Oberkochen, Germany) was used to direct both beams to the same spot and collect the fluorescence. A rectangular intensity profile with a diameter of 9.3 μm was created by insertion of a pinhole into the beam path. The dye molecules were bleached by a short laser pulse (200 ms), and the recovery of the fluorescence intensity was monitored with a photomultiplier (Hamamatsu Photonics, Herrsching, Germany). The lateral diffusion constant D and the mobile fraction were calculated from the measured fluorescence recovery profiles, following the method reported by Soumpasis.[35]

2.2. Results. *Homogeneity and Fluidity of the Lipid Layers.* Lipid DOPC membranes ranging from 0% to 100% DOTAP were prepared on COC by vesicle fusion and solvent exchange. The optical homogeneity of all lipid layers was checked repeatedly for each preparation technique using fluorescence microscopy. In all cases, the membranes were found to be homogeneous independent of the lipid composition and preparation technique. Increasing the salt content to 150 mM did not alter the membrane appearance. The same held true if the temperature was varied between 15 and 50 °C. In contrast, defect formation was observed on membranes supported on glass cover slides if either the temperature or the salt concentration were changed (data not shown).

Because the main transition temperatures of DOTAP and DOPC are below 0 °C, all intact lipid membranes are expected to be in the fluid phase at room temperature regardless of composition. This was verified by continuous bleaching (see Figure 2).

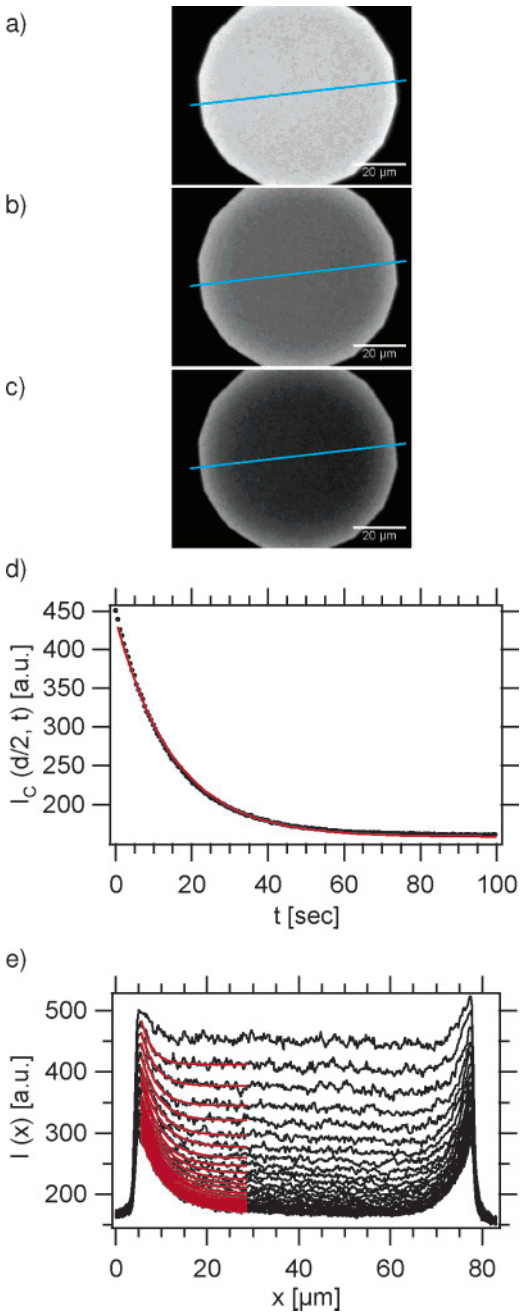

Figure 2. Continuous bleaching: Three fluorescence images show a supported membrane on COC after different illumination times. (a) Image taken shortly after the continuous illumination is started. (b) Image taken after 50 s of continuous illumination. (c) Image taken after 100 s of continuous illumination. (d) Time-dependent fluorescence signal measured in the center of the image. The solid red line represents a fit to an exponential decay (eq 2). (e) Consecutive line profiles across the illuminated area are displayed in black. The time between consecutive curves is 2 s. The solid red lines depict fits to an exponential decay (eq 2).

(33) Dietrich, C.; Merkel, R.; Tampe, R. *Biophys. J.* **1997**, *72*, 1701−1710.
(34) Axelrod, D.; Koppel, D. E.; Schlessinger, J.; Elson, E.; Webb, W. W. *Biophys. J.* **1976**, *16*, 1055−1069.
(35) Soumpasis, D. M. *Biophys. J.* **1983**, *41*, 95−97.

Eight hundred consecutive pictures were recorded using an exposure time of 500 ms. Three typical images are shown at $t = 0$, 50, and 100 s in Figure 2a−c, respectively. For each image, the mean fluorescence intensity of a central square area of size 10 μm was determined. This intensity is plotted against the elapsed time and fitted to an exponential decay to determine the bleaching constant b (Figure 2d). Line profiles were extracted for each image. Figure 2e includes every fourth line profile up to 100 s. The first curves show an essentially flat intensity profile. With time, a pronounced exponential decrease at the periphery develops.

To test for the homogeneity of the illumination, the diffusion constant was determined on both sides of the illuminated area (left and right). The two calculated diffusion constants coincided, indicating truly homogeneous illumination.

All lipid layers displayed a diffusion constant of around 2 ± 1 $\mu m^2/s$, which is of the order of magnitude expected for a fluid membrane.[36,37]

In summary, using the continuous bleaching method, it was possible to estimate easily and quickly the integrity and fluidity of all supported membranes prepared on COC. Further, fluorescence recovery after photobleaching (FRAP) experiments were performed to quantify whether the diffusion constant depends on the lipid composition beyond the limited sensitivity of the continuous bleaching method.

For each membrane, at least five independent measurements on different spots were performed to determine the mean value and the standard deviation of the diffusion constant D and the mobile fraction R. Typical measurements are shown in Figure 3a. All membranes had mobile fractions above 98%.

The average diffusion constant of all membranes prepared by vesicle fusion and by solvent exchange, except for 100% DOTAP prepared by solvent exchange, was calculated to be 0.83 $\mu m^2/s$. The diffusion constant D of the membranes prepared by vesicle fusion exhibits almost no dependence on the amount of cationic lipids and is approximately 0.73 $\mu m^2/s$ (Figure 3b, blue circles). This is in striking contrast to our results on glass surfaces where the diffusion constant was found to depend strongly on the amount of charged lipids in the membrane and on the detailed cleaning procedure (data not shown). Only for the solvent-exchange preparation did the diffusion constant of the membrane consisting of 100% DOTAP ($D = 0.38$ $\mu m^2/s$) deviate clearly from the average of the other lipid mixtures prepared by solvent exchange ($D = 0.88$ $\mu m^2/s$). This was validated for several independently prepared membranes, and the origin of this behavior is discussed below. The diffusion constant of glass-supported membranes showed a strong dependence on the cleaning procedure (data not shown).

Structure of the Lipid Layer. To probe the structure of the lipid membranes supported on COC, X-ray reflectivity experiments on DOPC membranes obtained by both preparation techniques were performed.

To characterize the bare polymer surface, first, the oxide-terminated silicon wafer with the spin-coated COC layer was measured in air (Figure 4a, orange dots) and in contact with water (Figure 4a, red dots) using a microfluidic setup.[28]

The air−COC−silicon oxide system exhibits a high contrast in electron density; therefore, the X-ray intensity oscillations occurring in the reflectivity curve of the COC layer have a large amplitude. When water is filled into the chamber, the loss of contrast at the water−COC interface reduces the oscillations. At the same time, the critical angle shifts from 0.09° to 0.06° while the shape of the curve remains unchanged.

Both curves (air and water) can be fitted nicely with a box model shown in Figure 4b where the electron density of silicon and air/water are known[38] and the electron density and the thickness of the COC layer and the surface roughnesses are free fitting parameters. Thus, the main information obtained is the electron density of the

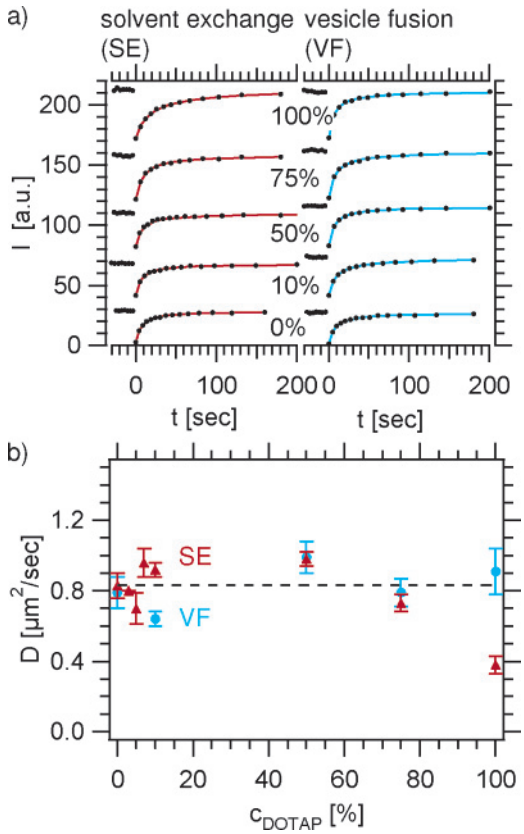

Figure 3. FRAP: (a) Typical FRAP measurements for membranes prepared by solvent exchange (SE, curves on the left) and by vesicle fusion (VF, curves on the right). The measured intensity is plotted vs time (black dots); the fit is shown as a red line (solvent exchange) or blue line (vesicle fusion). From top to bottom, the percentage of DOTAP in the membranes decreases from 100% to 0%. (b) Diffusion constant of the lipid membrane prepared by vesicle fusion (blue dots) and solvent exchange (red triangles) vs content of cationic DOTAP. The dashed line indicates the average diffusion constant of all measurements except 100% DOTAP prepared by solvent exchange.

COC layer ($\rho = 0.24$ $e^-/Å^3$), the COC layer thickness (~450 Å), and the COC surface roughness ($\sigma = 7$ Å), all of which do not change significantly in the presence of water. The resulting modeled reflectivity curves are displayed in Figure 4a as solid lines overlaying the original data.

The shape of the reflectivity curve changed qualitatively when a DOPC layer was prepared on the COC film by vesicle fusion (Figure 4a, light blue dots). The corresponding X-ray intensity curve exhibits a beating effect, indicating that additional layers are present. In fact, the data can be well described by introducing two additional electron density boxes representing lipid headgroups ($\rho_h = 0.34$ $e^-/Å^3$) and a box with a low electron density representing the lipid tails ($\rho_t = 0.26$ $e^-/Å^3$) (Figure 4a,b, blue curves), i.e., a lipid bilayer. The head-to-head distance, i.e., the distance between headgroup peaks, was found to be $d_{hh} = 29$ Å (see Table 1). An explanation as to why these measured data deviate from literature values of free or supported bilayers is provided in the Discussion section.

To explore whether the observation of a lipid bilayer on a hydrophobic support is unique to COC polymer surfaces, we also prepared a lipid membrane on hydrogen-terminated silicon (H−Si). The data are shown in Figure 5 as black dots.

Finally, a control experiment was carried out with a DOPC membrane deposited on a hydrophilic silicon wafer covered by an oxide layer (SiO_x) (Figure 5, red dots).

The reflectivity curves of the SiO_x and H−Si supported membranes can be fitted by a bilayer model. The resulting electron density profiles are shown in the inset of Figure 5. The resulting electron density of the lipid heads ρ_h is found to be 0.43 and 0.46 $e^-/Å^3$ for

(36) Köchy, T.; Bayerl, T. M. *Phys. Rev. E* **1993**, *47*, 2109−2116.
(37) Tamm, L. K.; McConnell, H. M. *Biophys. J.* **1985**, *47*, 105−113.
(38) Henke, B. L.; Gullikson, E. M.; Davis, J. C. *Atomic Data Nucl. Data Tables* **1993**, *54*, 181−342.

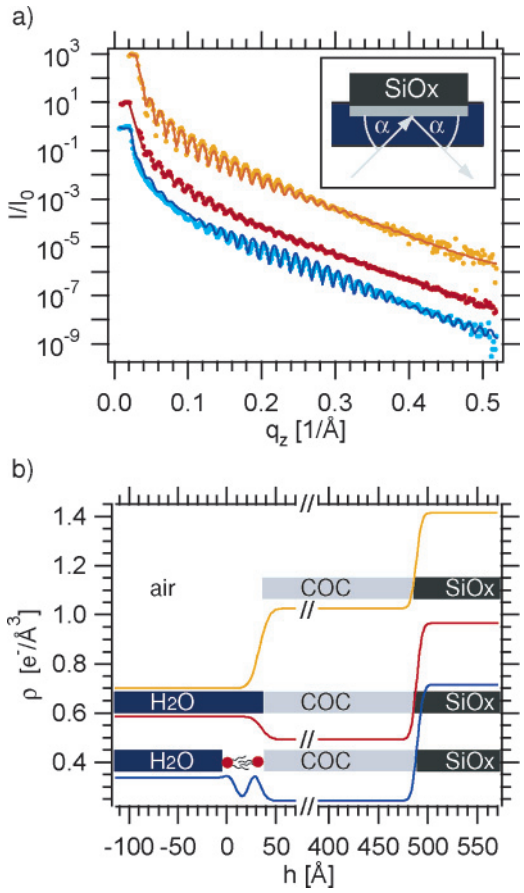

Figure 4. X-ray data: (a) Reflectivity curves of a uniform COC film exposed to air (orange dots) and to water (red squares) and with a DOPC layer prepared by vesicle fusion (light blue triangles). Fits to the different curves are included as solid lines in the same color shaded slightly darker. The reflectivity curves are shifted vertically for clarity. The inset illustrates the setup used during reflectivity measurements. (b) Electron density profiles corresponding to the fits in a. The profile for the COC layer on air is shown as an orange line, the profile for the COC layer under water is displayed as a red line, and the profile of a COC layer with a lipid membrane on top is depicted with a blue line. The profiles are shifted vertically for clarity. A cartoon illuminating the physical meaning of the electron density profile is placed on top of each profile.

Table 1. Parameters Extracted from X-ray Reflectivity Measurements for DOPC Membranes on Different Supports

source	support	d_{hh} (Å)	ρ_h ($e^-/Å^3$)	ρ_t ($e^-/Å^3$)
this work	COC (VF)	29	0.34	0.26
	COC (SE)	27	0.33	0.29
	H-Si	40	0.43	0.30
	SiO_x	36	0.46	0.30
Liu et al.[42]	stacks on SiO_x	37	0.44	0.24−0.29
Tristram-Nagle[43]	free stacks	35	0.46	0.23−0.29

H−Si and SiO_x, respectively. The electron density of the lipid tails ρ_t coincides at 0.30 $e^-/Å^3$ for both supports. The head-to-head distance d_{hh} is given by 40 and 36 Å for H−Si and SiO_x, respectively (see Table 1).

To test the influence of the deposition method, we performed reflectivity measurements on a DOPC membrane deposited on COC by solvent exchange. The measurements on the lipid membranes prepared by vesicle fusion (light blue dots) and by solvent exchange (red dots) are compared in Figure 6. For the membrane prepared by solvent exchange, a slightly reduced amplitude of the oscillations was observed.

Again, a bilayer model fits best to the data, indicating that, qualitatively, the bilayer formation is not dependent on the preparation

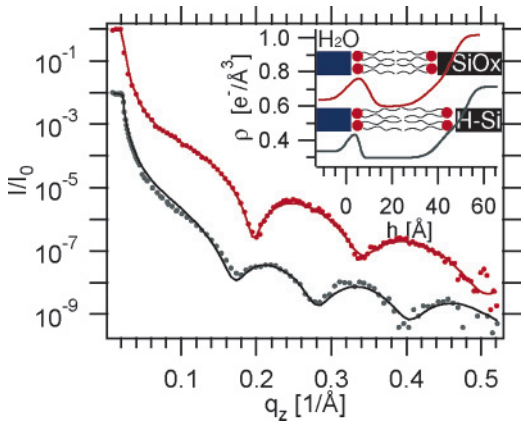

Figure 5. DOPC membranes on SiO_x and H−Si: reflectivity curve of a lipid layer on the hydrophilic SiO_x (red circles) and the best fit (dark red line). Displaced vertically is the reflectivity curve of a membrane on the hydrophobic H−Si (gray dots) with the best fit (black line). The profiles corresponding to the fits are shown in the inset in the upper right corner. A schematic drawing above the profiles illustrates the interpretation of the box models.

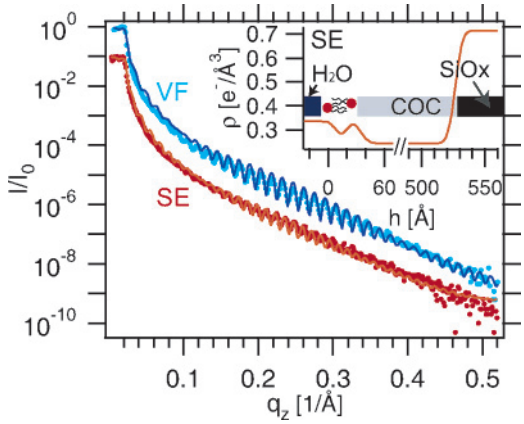

Figure 6. X-ray reflectivity: Reflectivity curves of DOPC lipid layers prepared by vesicle fusion (VF) and solvent exchange (SE). The fits are included as full lines in the same color shaded darker. The inset shows the electron density profile of the sample prepared by solvent exchange.

method. However, the contrast in electron density is clearly reduced ($\rho_h = 0.33\ e^-/Å^3$ and $\rho_t = 0.29\ e^-/Å^3$). The reason for this is elucidated in the following discussion. The head-to-head distance is $d_{hh} = 27$ Å.

3. Discussion

Homogeneity and Fluidity. On hydrophilic supports such as glass cover slides, a change in temperature or salt concentration might result in membrane defects visible with fluorescence microscopy. It is known that the diffusion constant of glass-supported membranes shows a strong dependence on the cleaning procedure.[11] The conformation of a lipid membrane supported by COC seems more stable and less dependent on solvent and temperature conditions, as defect formation was not observed in this study and the diffusion constant does not depend on the amount of charge in the membrane. This stability is of practical relevance.

The possibility that the lipids adsorb to the surface as vesicles can be ruled out because our continuous bleaching and FRAP experiments probed the mobility of the lipid membrane on the length scale of a few micrometers.

The diffusion constants measured in our present work with FRAP (0.8 $\mu m^2/s$) is very similar to the diffusion constant (0.9

$\mu m^2/s$) measured by Lenz et al.[15] for a POPC lipid membrane on hydrophobic poly(dimethylsiloxane) (PDMS) surfaces. Also, FRAP measurements showed no dependence of the diffusion constant on the lipid composition for membranes on COC prepared by vesicle fusion. The same holds true for membranes prepared by solvent exchange up to a DOTAP ratio of 75%. This is explained by the hydrophobic surface being uncharged, so that the electrostatic interactions between the lipid membrane and the substrate are reduced compared to those with glass surfaces. Only the diffusion constant of a membrane composed of 100% DOTAP prepared by solvent exchange differs notably from all others. It is likely that, during the preparation process by solvent exchange, some amphiphilic 2-propanol stays intercalated in the membrane.[39,40] This effect might increase for charged lipids, which could lead to the formation of small defects (below the resolution of optical microscopy) in the membrane. Such defects reduce the diffusion constant significantly.

Structure. COC represents a highly hydrophobic substrate (contact angle = 89°).[20] Because of hydrophobic effects, one might expect that lipids form a monolayer on hydrophobic substrates with the lipid tails facing toward the substrate. A clear reduction of the number of lipids in membranes deposited on hydrophobic substrates has been reported before.[15,16,41] In detail, Lenz et al.[15] found a factor of 2 difference between the two fluorescence intensities of a lipid membrane on hydrophobic and oxidized (hydrophilic) PDMS. Elliot et al.[16] compared the fluorescence intensity of lipid membranes on polystyrene films with equivalent membranes on glass surfaces and counted the single fluorescence events with fluorescence correlation spectroscopy. Retzinger et al.[41] counted the radioactivity of radioactively labeled lipids on polystyrene−divinylbenzene beads.

These experiments have taken the reduced number of lipids as an indication for monolayer formation. Naturally, the total amount of lipids in a monolayer is only one-half that in a compact bilayer. Our experiments suggest a different interpretation. We argue that the reduction of the number of lipids on hydrophobic supports might be due not to formation of a compact monolayer but, at least in the case of COC, to the formation of a thinned, less densely packed bilayer, as we will show in the following discussion of the X-ray data.

To emphasize details of the reflectivity curves, we divide the reflectivity of the lipid layer by the Fresnel reflectivity ($1/q_z^4$). The measured reflectivity curve of the COC layer coated with a lipid membrane by vesicle fusion is displayed in Figure 7a as light blue dots (labeled data). Vertically displaced is the best fit of the reflectivity curve resulting from a bilayer box model shown as a solid dark blue line (labeled bilayer). The best fit of the reflectivity data resulting from a monolayer box model is displayed stacked under it (labeled monolayer). Figure 7b shows the associated electron density profiles with a schematic drawing on top illustrating the physical composition of the layers. Only the section of the electron density profile in proximity to the lipid layer is displayed.

The monolayer model succeeds in reproducing the amplitude and phase of the small oscillations quite well, but it fails to show the beating effect.

In contrast, the bilayer model fits the oscillations reasonably well, including the beating. Thus, we conclude that a bilayer formed.

Details of the Bilayer Structure. The vertical head-to-head distance of the COC supported bilayer (d_{hh}) was found to be 29 Å. This is 8 and 6 Å shorter, respectively, than the values reported by Liu et al.[42] for DOPC multilamellar membranes on SiO_x and similar measurements on DOPC/water solutions.[43] In the following, discussion, we call this membrane a thinned bilayer.

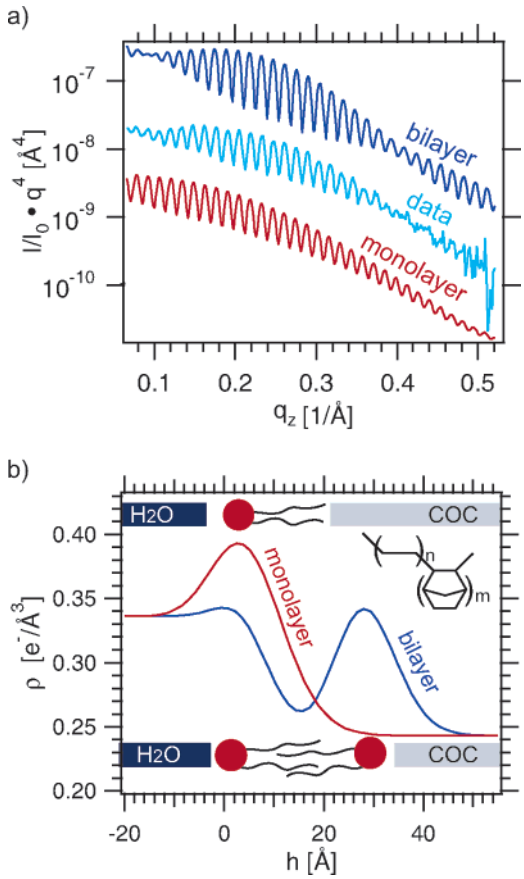

Figure 7. Analysis: (a) The top curve features the best fit of the reflectivity data assuming a bilayer box model, divided by the Fresnel reflectivity q^{-4} (dark blue solid line, bilayer). Stacked under it, the measured reflectivity data (light blue solid line, data) are displayed. The last curve represents the best fit of the reflectivity curve based on a monolayer box model (red solid line, monolayer). (b) Profiles corresponding to the fit curves in a (bilayer, dark blue line; monolayer, red line). Right above and below the profiles, schematic drawings illustrate the box models. The structural formula of COC is placed in the upper right corner.

The electron density of the lipid heads (ρ_h) in the thinned bilayer is reduced to 0.34 $e^-/Å^3$, i.e., 0.1 and 0.12 $e^-/Å^3$ smaller than reported previously,[42,43] indicating a clear reduction in the packing density of the lipids.

The electron density of the lipid tails (ρ_t) in the thinned bilayer was found to be 0.26 $e^-/Å^3$. Tristram et al.[43] and Liu et al.[42] distinguish two domains in the lipid tail region. The headgroup region is followed by a tail region with an intermediate electron density (0.29 $e^-/Å^3$)[42,43] separated from the other leaflet of the bilayer by a small region with very low electron density (0.24[42] and 0.23[43] $e^-/Å^3$). In our study, we do not distinguish between those tail regions, as it is well-known that data up to $q > 0.5$ Å are readily explained by a two-box model.[44] Therefore, our ρ_t result is between these literature values ($\rho_t = 0.26$ $e^-/Å^3$).

Note that the lipid density of a bilayer formed on SiO_x (Figure 5) compares reasonably well with literature values[42,43] (sum-

(39) Barry, J. A.; Gawrisch, K. *Biochemistry* **1994**, *33*, 8082−8088.
(40) Barry, J. A.; Gawrisch, K. *Biochemistry* **1995**, *34*, 8852−8860.
(41) Retzinger, G. S.; Meredith, S. C.; Lau, S. H.; Kaiser, E. T.; Kezdy, F. J. *Anal. Biochem.* **1985**, *150*, 131−140.
(42) Liu, Y. F.; Nagle, J. F. *Phys. Rev. E* **2004**, *69*, 040901.
(43) Tristram-Nagle, S.; Petrache, H. I.; Nagle, J. F. *Biophys. J.* **1998**, *75*, 917−925.
(44) Schalke, M.; Lösche, M. *Adv. Colloid Interface Sci.* **2000**, *88*, 243−274 (Special Issue).

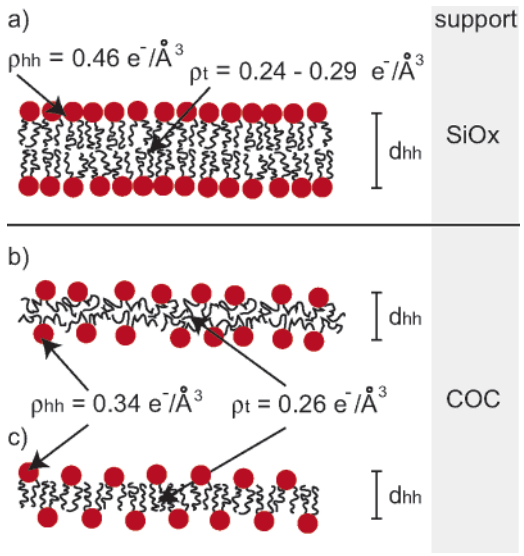

Figure 8. Packing density in a bilayer: (a) typical bilayer as found in supported DOPC membrane stacks or on SiO_x. Thinned bilayer: (b) coiled tails, (c) interdigitated tails.

marized in Table 1). For a SiO_x-supported membrane (Figure 5), we obtain a head-to-head distance of $d_{hh} = 36$ Å, an electron density of the heads of $\rho_h = 0.46$ e$^-$/Å^3, and an electron density of the tails of $\rho_t = 0.3$ e$^-$/Å^3, in good agreement with literature values.[42,43]

Table 1 summarizes the head-to-head distance d_{hh}, the maximum electron density of the headgroups ρ_h, and the density of the lipid tails ρ_t on the different supports and for the different preparation techniques. Values from the literature are included for comparison.

A simple explanation of the reduced electron density of the thinned bilayer on COC is a reduced packing density of the lipids.

The bilayer structure on SiO_x and two different bilayer configurations in agreement with the measurements on COC are summarized in Figure 8. Figure 8a shows the configuration of a typical bilayer as found, for example, on SiO_x. On COC, the packing density of the lipids is reduced, allowing the lipid tails to relax into a more disordered conformation (see Figure 8b). As shown in Figure 8c, the lipid tails could also interdigitate, reducing the packing density while the bilayer thickness is reduced.

This thinned bilayer is similar to the monolayer formation found for the bipolar lipids in archae bacteria.[45] Interdigitated PC bilayers induced by traces of alcohol in the bulk solution have been reported by Mou et al.[46] Hollinshead et al.[47] also demonstrated that lipids can interdigitate on a supported monolayer grafted from octadecyltrichlorosilane (OTS) if the grafting density is 60%.

For COC, a different, more general mechanism might be responsible for the formation of a thinned bilayer. d_b is the lipid bilayer thickness, i.e., the distance from the beginning of the headgroup in the first layer to the end of the opposing headgroup. Burgess et al.[48] showed that the bilayer thickness d_b of DMPC membranes spread on gold depends critically on the surface charge density of the gold surface. At charge densities more negative than -0.2 Cm^{-2}, the bilayer thickness on gold corresponded to the thickness typically found for fully hydrated multilayers ($d_b = 37$ Å). A similar surface charge density of -0.25 Cm^{-2} was estimated for silicon oxide surfaces at pH 8.[49] In turn, the bilayer thickness on SiO_x is the similar to that of bilayer stacks.

At zero surface charge, the bilayer thickness on gold was reduced to 26 Å. The ζ potential of COC[50] is -25 mV,[50] corresponding to a basically uncharged surface. Remarkably, the reduced bilayer thickness on COC agrees with the reduced bilayer thickness on uncharged gold surfaces, suggesting that surface charge might control the membrane thickness.

On the other hand, we cannot exclude other explanations that might be responsible for the membrane thinning on COC. Such reasons could include surface roughness or details of the molecular composition of the surface. This is supported by the enlarged d_{hh} value found on H−Si. The d_{hh} value of DOPC on H−Si was calculated to be 40 Å, 3−5 Å larger than the respective literature values, while ρ_h and ρ_t did not deviate significantly.

Although both H−Si and COC are hydrophobic, the two substrates are very different in terms of molecular composition. Also, the COC support has a larger surface roughness, which might influence the packing density as well.

For a membrane prepared by solvent exchange on COC, a bilayer model also fits the data reasonably well. The head-to-head distance d_{hh} is 27 Å, in accordance with the distance gained from the vesicle-fusion sample. The reduced contrast in electron density ($\rho_h = 0.33$, $\rho_t = 0.29$) compared to the vesicle-fusion sample can be explained by intercalated 2-propanol molecules. Another explanation is the formation of defects smaller than the optical resolution. Other experiments performed in our laboratory in which DNA molecules were adsorbed onto mixed DOPC/DOTAP lipid membranes did not show a difference between the preparation methods, even though these experiments are intrinsically very sensitive to even small membrane defects.[51] Therefore, the reduced electron density of the heads is most likely explained by 2-propanol molecules being intercalated into the membrane rather than by defect formation.

The fluorescence microscopy and FRAP experiments did not detect any difference in the lipid membranes prepared by vesicle fusion or by solvent exchange. This was further supported by X-ray reflectivity experiments where the two preparation techniques resulted in similar curves except for a slight reduction in the electron density contrast.

Water Layer. Finally, we address the question of whether a mesocopic water layer ($d_w \geq 10$ Å) is needed to ensure a fluid bilayer.

In the literature, d_w has been determined directly with scattering methods[30,52−55] or indirectly with microscopic techniques[56] and found to range between 5 and 500 Å. The large deviations in d_w resulted most likely from different surface treatments.

(45) Gliozzi, A.; Relini, A.; Chong, P. L. G. *J. Membr. Sci.* **2002**, *206*, 131−147 (Special Issue).
(46) Mou, J. X.; Yang, J.; Huang, C.; Shao, Z. F. *Biochemistry* **1994**, *33*, 9981−9985.
(47) Hollinshead, C. M.; Hanna, M.; Barlow, D. J.; De Biasi, V.; Bucknall, D. G.; Camilleri, P.; Hutt, A. J.; Lawrence, M. J.; Lu, J. R.; Su, T. J. *Biochim. Biophys. Acta: Biomembranes* **2001**, *1511*, 49−59.
(48) Burgess, I.; Li, M.; Horswell, S. L.; Szymanski, G.; Lipkowski, J.; Majewski, J.; Satija, S. *Biophys. J.* **2004**, *86*, 1763−1776.
(49) Groves, J. T.; Boxer, S. G.; McConnell, H. M. *Proc. Nat. Acad. Sci. U.S.A.* **1997**, *94*, 13390−13395.
(50) Rädler, U.; Kahl, V. Private communication, ibidi GmbH, Munich, Germany, 2005.
(51) Hochrein, M.; Leierseder, J.; Rädler, J.; Golubovic, L. *Phys. Rev. Lett.*, accepted.
(52) Charitat, T.; Bellet-Amalric, E.; Fragneto, G.; Graner, F. *Eur. Phys. J. B* **1999**, *8*, 583−593.
(53) Fragneto, G.; Bellet-Amalric, E.; Charitat, T.; Dubos, P.; Graner, F.; Perino-Galice, L. *Physica B* **2000**, *276*, 501−502.
(54) Koenig, B. W.; Kruger, S.; Orts, W. J.; Majkrzak, C. F.; Berk, N. F.; Silverton, J. V.; Gawrisch, K. *Langmuir* **1996**, *12*, 1343−1350.
(55) Johnson, S. J.; Bayerl, T. M.; McDermott, D. C.; Adam, G. W.; Rennie, A. R.; Thomas, R. K.; Sackmann, E. *Biophys. J.* **1991**, *59*, 289−294.
(56) Merkel, R.; Sackmann, E.; Evans, E. *J. Phys.* **1989**, *50*, 1535−1555.

In our study, we tried to determine the size of the water gap (d_w) between the membrane and the support for COC, SiO_x, and H−Si. We were not able to resolve a water layer on COC within the error of the surface roughness, which implies that d_w must be smaller than 7 Å if present at all. Also, no water gap was resolved on SiO_x and H−Si, implying that, in these cases, d_w is smaller than 4 and 3 Å, respectively. The value $d_w = 4$ Å was measured recently by X-ray reflectivity by Miller et al.[57] for a DOPC membrane supported on SiO_x. Another study found that it was not necessary to introduce a water layer in order to reproduce adequately the reflectivity data of a DOPC membrane on SiO_x.[28]

The fact that we obtain fluid membranes on COC and SiO_x without the presence of a significant water layer suggests that a mesoscopic water layer is not mandatory to maintain fluidity.

4. Conclusion

In this article, we demonstrated that it is possible to prepare homogeneous and fluid lipid membranes on COC surfaces for different membranes consisting of different concentrations of DOTAP and DOPC. Using X-ray reflectivity measurements, we found that these membranes consist of a thinned bilayer. These coating properties make the thermoplast COC an ideal material for biofunctional surfaces.[51]

Acknowledgment. We thank Oliver Purrucker, Thomas Schubert, and Murat Tutus for their help with the FRAP measurements and Oliver Seeck for help with the setup of the D4 reflectometer at Hasylab. We owe thanks to ibidi GmbH for the donation of μ-slides. This work was supported by SFB 563 of the Deutsche Forschungsgemeinschaft. We thank the ESRF and the Hasylab for continuous support of this work.

Supporting Information Available: Additional structural model of the lipid membrane. This material is available free of charge via the Internet at http://pubs.acs.org.

LA051820Y

(57) Miller, C.; Majewski, J.; Gog, T.; Kuhl, T. L. *Phys. Rev. Lett.* **2005**, *94*, 238104.

A.3 Full text of Ref. [3]

Christian Reich, Petra A. Neff, Andreas R. Bausch, Joachim O. Rädler and Bert Nickel

Supported Membranes on Polyelectrolyte Layers Studied by X-ray Reflectometry.

physica status solidi (a) **203**, no. 14, 3463-3467 (2006).

Abstract:
Supported lipid membranes on polymer layers were investigated by X-ray reflectivity in aqueous environment using a microfluidic setup. Polyallylamine hydrochloride and poly(sodium 4-styrenesulfonate) were used for building up multilayer architectures with alternating charge distribution. First results from synchrotron reflectivity experiments demonstrate that such polyelectrolyte layers can act as aqueous spacers with almost negligible electron density contrast as compared to water. Lipid membranes on top of such polymer spacers are expected to show only minor structural denaturation. Thus this model system is proposed as a step towards decoupling lipid membranes from solid substrates. The accessibility to such biological systems using high-resolution X-ray reflectivity and the possibility to insert well-defined spacers with minimum contrast are highly competitive to established methods of neutron reflectivity.

Permanent weblink:
http://dx.doi.org/10.1002/pssa.200622408

Original Paper

phys. stat. sol. (a) **203**, No. 14, 3463–3467 (2006) / **DOI** 10.1002/pssa.200622408

Supported membranes on polyelectrolyte layers studied by X-ray reflectometry

Christian Reich[1], **Petra A. Neff**[2], **Andreas R. Bausch**[2], **Joachim O. Rädler**[1], and **Bert Nickel**[*, 1]

[1] Department für Physik, Ludwig-Maximilians-Universität, Geschwister-Scholl-Platz 1, 80539 München, Germany

[2] Physik-Department E22, Technische Universität München, James-Franck-Straße, 85748 Garching, Germany

Received 9 July 2006, revised 16 August 2006, accepted 17 August 2006
Published online 10 November 2006

PACS 61.10.Kw, 82.35.Rs, 87.16.Dg

Supported lipid membranes on polymer layers were investigated by X-ray reflectivity in aqueous environment using a microfluidic setup. Polyallylamine hydrochloride and poly(sodium 4-styrenesulfonate) were used for building up multilayer architectures with alternating charge distribution.
First results from synchrotron reflectivity experiments demonstrate that such polyelectrolyte layers can act as aqueous spacers with almost negligible electron density contrast as compared to water. Lipid membranes on top of such polymer spacers are expected to show only minor structural denaturation. Thus this model system is proposed as a step towards decoupling lipid membranes from solid substrates. The accessibility to such biological systems using high-resolution X-ray reflectivity and the possibility to insert well-defined spacers with minimum contrast are highly competitive to established methods of neutron reflectivity.

1 Introduction

Layer-by-layer self-assembly of polyelectrolytes is a simple and convenient method to form well- defined layers on solid substrates such as silicon [1, 2]. Polyelectrolytes in solution can adsorb to substrates with a defined net charge due to electrostatic forces. Multilayers of binary composition are produced by alternating deposition of polyelectrolytes with different charge. Although there is interdigitation between the layers up to a certain extent [3], the top layer usually is smooth and well defined. Such multilayers are highly hydrophilic and contain a significant amount of water. This feature makes these polymers particularly promising as polymeric interlayer to support lipid membranes.

Supported lipid membranes are widely investigated model systems for studying cell membrane properties [4]. Placing a membrane on a flat substrate allows access to a manifold of different surface sensitive techniques such as X-ray and neutron surface diffraction. Nevertheless, lipid-substrate interactions generally limit lipid diffusion capability in the membrane bilayer and may sometimes inhibit biological functionality. Thus it is desirable to have well-defined substrates which interact only negligibly with the membrane. Decoupling the membrane from the substrate by soft polymer spacers can fulfill this requirement.

In this communication we present results from X-ray reflectivity studies of lipid membranes supported on soft polyelectrolyte layers. We show that this model system is a promising candidate for further studies on detached lipid membranes.

[*] Corresponding author: e-mail: nickel@lmu.de, Phone: +49 89 2180 1460, Fax: +49 89 2180 3182

2 Experiment

Polyallylamine hydrochloride (PAH, positive net charge) and poly(sodium 4-styrenesulfonate) (PSS, negative net charge) were purchased from Sigma–Aldrich and dissolved in buffer solution (50 mM NaCl, 10 mM Tris, pH 7.5). Lipids were bought from Avanti Polar Lipids, Alabama, USA and used without further purification.

A sample chamber with a silicon wafer at the bottom of a microfluidic channel was used for the reflectivity studies. The chamber design is optimized for X-ray diffraction at solid-liquid interfaces and described in Ref. [5, 6].

Polyelectrolyte layers were produced as follows: The silicon wafers were cleaned using the method described in Ref. [7] and pre-wetted with buffer solution (50 mM NaCl, 10 mM Tris, pH 7.5). A single layer of PAH (5 mg/ml in buffer) was deposited on the wafer by flushing the microfluidic channel with 1 ml solution. After three minutes, the channel was flushed again with pure buffer to get rid of excess solution. As next step, PSS was injected into the channel (1 ml of 5 mg/ml solution) and again replaced by buffer after three minutes. This procedure was repeated consecutively until the desired multilayer architecture was achieved.

Preparation of supported lipid bilayers: Lipid stock solutions of 1,2-Dioleoyl-sn-Glycero-3-Phosphocholine (DOPC, neutral) and 1,2-Dioleoyl-sn-Glycero-3-Phospho-L-Serine (DOPS, negative net charge) were partitioned into desired quantities and dried under nitrogen flow, followed by 24 hours in an evacuated exsiccator. Multilamellar vesicle suspensions (concentration 1 mg/ml) were obtained by hydration with deionized pure water (specific resistivity 18.2 MΩ cm, Millipore Corp., Billerica, Massachusetts). Sonication of these suspensions gave small unilamellar vesicles (SUVs). The fresh SUV solution was injected into the microchannel and incubated at room temperature for two hours, allowing the vesicles to adsorb on the top polyelectrolyte layer. The microchannel was subsequently flushed with buffer solution (50 mM NaCl, 10 mM Tris, pH 7.5). Due to osmotic pressure between the water-filled vesicles and the buffer environment, SUVs tend to deform and to rupture, giving lipid bilayer disks on the substrate. Such disks subsequently form continuous bilayers on the substrate [8, 9].

The X-ray reflectivity experiments were carried out at the European Synchrotron Radiation Facility (ESRF) in Grenoble, France (beamline ID01) and the Hamburger Synchrotronstrahlungslabor (Hasylab) in Hamburg, Germany (beamline D4). The X-ray energy was 19.9 keV and the same experimental geometry was used as in Ref. [5].

3 Results

3.1 Lipid membrane on a single polyelectrolyte layer

First, a single layer of PAH was prepared on SiO_2 in excess buffer as described above. The X-ray reflectivity of the layer shows no characteristic signature and is undistinguishable to the reflectivity of a smooth silicon oxide substrate exposed to buffer liquid (Fig. 1(a)). Either the polyelectrolyte layer did not form at all, or the layer is invisible in the reflectivity data due to a vanishing electron density contrast between the buffer and the strongly hydrated polyelectrolyte layer.

Subsequently, small unilamellar vesicles of negatively charged DOPS were added and incubated for two hours. Afterwards, the chamber was flushed again with buffer solution to remove non-adhered and unfused vesicles. It is known that supported membranes of pure negatively charged lipids hardly spread on bare silicon oxide due to repulsive electrostatic forces [10]. Thus no lipid membrane is expected on the substrate if no polyelectrolyte layer is present.

The reflectivity signal now shows clear characteristic oscillations, indicating the formation of a supported lipid membrane detached from the substrate by a ca. 40 (±4) Å spacer (Fig. 1(b)). The corresponding electron density profile (Fig. 2(a)) was extracted from a fit using Parratt's algorithm [11]: A simple five box model with an average roughness of 4 Å was refined using a one-dimensional Newton–Raphson method [12]. The refinement did not improve notably upon increasing the number of boxes in the fit model.

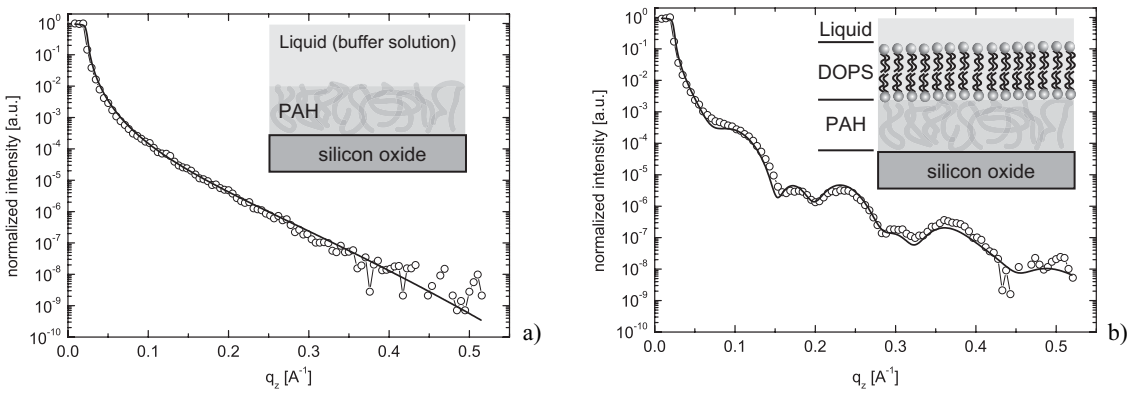

Fig. 1 (a) Reflectivity of a PAH-layer deposited on SiO_2 in excess water. No characteristic oscillations are visible. (b) Reflectivity of a DOPS-membrane floating on a PAH-cushion. The solid lines are fits to the data. All data sets are background corrected and normalized.

The data strongly indicates the presence of a PAH-layer between wafer and lipid membrane. The PAH-layer can be adequately fitted assuming an electron density very similar to the density of water. Thus we conclude that the PAH-layer consists of a significant amount of incorporated water molecules. This is in agreement with previous X-ray reflectivity experiments which have demonstrated that such polymer layers show an increase in electron density upon drying [3].

The extracted headgroup–headgroup distance of the membrane was determined to 49 (±4) Å, which is slightly larger than comparable data from supported DOPC-membranes on silicon oxide [5, 13]. This result was verified by performing the data refinement using different models and number of boxes. The dynamical momentum range covered by the data may not be sufficient to exclude other possible electron density profiles. However, it is reasonably large to conclude that the membrane is smoothly aligned on top of the polymer, without large undulations. Further, the membrane on the polymer monolayer retains the interface roughness of the bare silicon substrate (ca. 4 Å). The data sets were recorded at ESRF.

3.2 Lipid membrane on polyelectrolyte multilayers

In the next step, multilayer stacks were deposited on silicon oxide as described above. The top layer was PAH in all cases. The reflectivity of a DOPS membrane on 7 alternating PAH/PSS monolayers is shown in Fig. 2(b). An overall thickness of ca. 82 (±7) Å was found for the polymer cushion (approx.

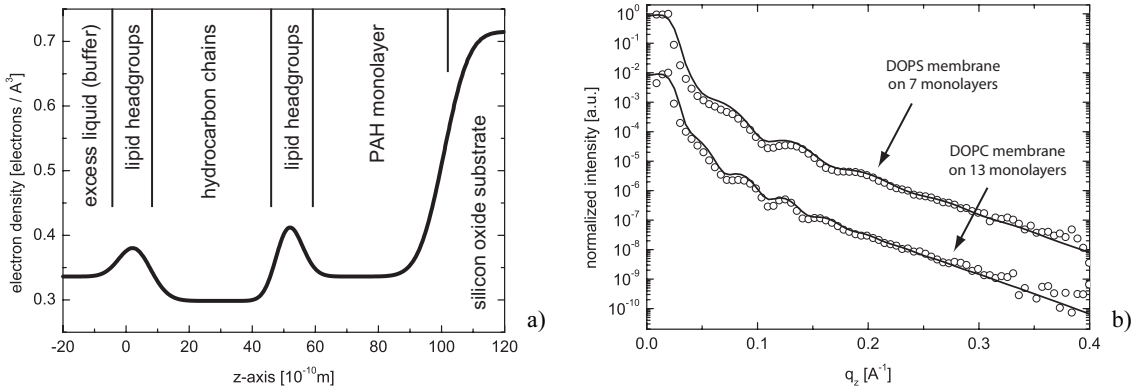

Fig. 2 (a) Electron density profile corresponding to the fit in Fig. 1(b). (b) Reflectivity of a DOPS-membrane on 7 monolayers of PAH/PSS and of a DOPC-membrane on 13 monolayers of PAH/PSS. The scans are shifted for clarity.

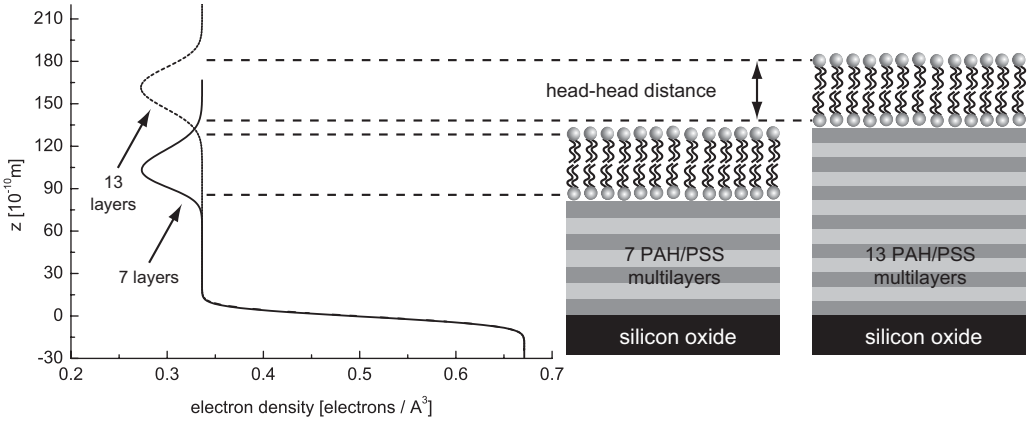

Fig. 3 Electron density profiles for the data in Fig. 2(b). The dominant contrast contribution to the reflectivity signal results from the water-free chain region of the floating membrane.

11.7 Å average thickness for one layer). This result is in good agreement with complementary ellipsometry data [14]. The discrepancy to the thickness of a single PAH-layer (ca. 40 Å) can be explained with a strong intercalation effect of alternating polyelectrolyte layers [3].

The signature of the lipid membrane is dominated by the electron density of the hydrocarbon chains, which are the only hydrophobic components in the system and therefore do not show swelling in the presence of water molecules (Fig. 3). The electron density of the lipid headgroups was found to converge towards the water density level, independently of the applied fitting model. We ascribe the vanishing electron density of the lipid headgroups partially to an increase of the laterally averaged interface roughness. The calculated roughness of the membrane/polymer interface is ca. 12 Å. This interface is not as well-defined as in the case of only one single PAH-layer between silicon oxide and the lipid membrane. Intercalation of lipid headgroups into holes or cavities of the underlying polymer could favor a loss of contrast as well. On the other hand, the fast decay of the oscillations in the data may indicate that these membranes were only partially homogeneous.

In a parallel experiment, 13 alternating monolayers of PAH/PSS were deposited on silicon oxide, followed by a membrane of DOPC (Fig. 2(b)). We found no notable difference in the adhesion behavior between vesicles of (neutral) DOPC and (negative) DOPS on polyelectrolyte layers. Here, the overall multilayer thickness was found to be ca. 133 (±10) Å (approx. 10.2 Å average thickness for one layer), which is in good agreement with the previous experiment and with Ref. [14]. The calculated roughness at the membrane/polymer interface is 11 Å. These data sets were recorded at Hasylab.

4 Conclusions

We have demonstrated that polyelectrolyte layers can act as aqueous spacers and provide well defined model systems for X-ray surface diffraction studies of polymer supported lipid membranes. The reflectivity data show that it is possible to produce homogeneous membranes on smooth polymer layers. The thickness of these layers can be tuned with an accuracy of about one nanometer. However, a thicker layer is accompanied with an increased surface roughness. Another tunable parameter is the overall net charge of the top polymer layer, which offers further possibilities, e.g. for biosensor applications [14].

Acknowledgements We thank ibidi GmbH, München, Germany for supplying the plastic supports of the microfluidic chambers. We also thank B. Krause and T. H. Metzger for continuous support during the synchrotron experiments at ESRF. We are indebted to Hasylab and ESRF for supplying beamtime and financial travel support. This work was supported by the Deutsche Forschungsgemeinschaft (Grant no. SFB 563).

References

[1] G. Decher, Science **277**, 1232–1237 (1997).
[2] C. Delajon, T. Gutberlet, R. Steitz, H. Möhwald, and R. Krastev, Langmuir **21**, 8509–8514 (2005).
[3] A. Plech, T. Salditt, C. Münster, and J. Peisl, J. Colloid Interface Sci. **223**, 74–82 (2000).
[4] E. Sackmann, Science **271**, 43–48 (1996).
[5] C. Reich, M. B. Hochrein, B. Krause, and B. Nickel, Rev. Sci. Instrum. **76**, 095103 (2005).
[6] M. B. Hochrein, C. Reich, B. Krause, J. O. Rädler, and B. Nickel, Langmuir **22**, 538–545 (2006).
[7] W. Kern and D. A. Puotinen, RCA Review **31**, 187 (1970).
[8] A. A. Brian and H. M. McConnell, Proc. Natl. Acad. Sci. **81**, 6159–6163, (1984).
[9] J. Rädler, H. Strey, and E. Sackmann, Langmuir **11**, 4539–4548 (1995).
[10] A. R. Sapuri, M. M. Baksh, and Jay T. Groves, Langmuir **19**, 1606–1610 (2003).
[11] L. G. Parratt, Phys. Rev. **95**, 359 (1954).
[12] W. Press, B. Flannery, S. Teukolsky, and W. Vetterling, Numerical Recipes (Cambridge University Press, Cambridge, 1986).
[13] Y. Liu and J. F. Nagle. Phys. Rev. E **69**, 040901 (2004).
[14] P. A. Neff, A. Naji, C. Ecker, B. Nickel, R. v. Klitzing, and A. R. Bausch, Macromolecules **39**, 463–466 (2006).

A.4 Full text of Ref. [4]

Margaret R. Horton, Christian Reich, Alice P. Gast, Joachim O. Rädler and Bert Nickel

Structure and dynamics of crystalline protein layers bound to supported lipid bilayers.

Langmuir **23** (11), 6263-6269 (2007).

Abstract:
We study proteins at the surface of bilayer membranes using streptavidin and avidin bound to biotinylated lipids in a supported lipid bilayer (SLB) at the solid-liquid interface. Using X-ray reflectivity and simultaneous fluorescence microscopy, we characterize the structure and fluidity of protein layers with varied relative surface coverages of crystalline and noncrystalline protein. With continuous bleaching, we measure a 10-15% decrease in the fluidity of the SLB after the full protein layer is formed. We propose that this reduction in lipid mobility is due to a small fraction (0.04) of immobilized lipids bound to the protein layer that create obstacles to membrane diffusion. Our X-ray reflectivity data show a 40 Å thick layer of protein, and we resolve an 8 Å layer separating the protein layer from the bilayer. We suggest that the separation provided by this water layer allows the underlying lipid bilayer to retain its fluidity and stability.

Permanent weblink:
http://dx.doi.org/10.1021/la063690e

Table of contents graphic:

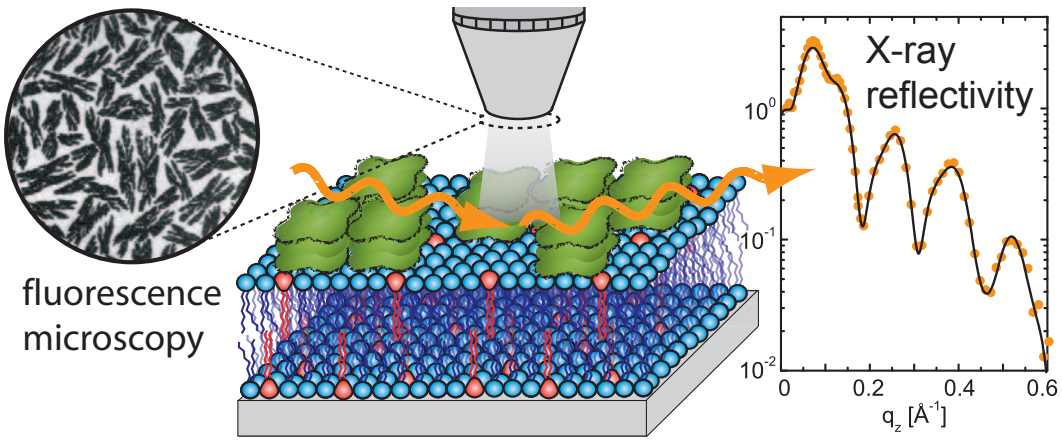

Structure and Dynamics of Crystalline Protein Layers Bound to Supported Lipid Bilayers

Margaret R. Horton,*[,†,‡] Christian Reich,[†] Alice P. Gast,[§] Joachim O. Rädler,[†] and Bert Nickel[†]

Department für Physik, Ludwig-Maximilians-Universität, Geschwister-Scholl-Platz 1, 80539 München, Germany, Department of Chemical Engineering, Massachusetts Institute of Technology, Cambridge, Massachusetts 02139, and Department of Chemical Engineering, Lehigh University, Bethlehem, Pennsylvania 18015

Received December 20, 2006. In Final Form: March 7, 2007

We study proteins at the surface of bilayer membranes using streptavidin and avidin bound to biotinylated lipids in a supported lipid bilayer (SLB) at the solid−liquid interface. Using X-ray reflectivity and simultaneous fluorescence microscopy, we characterize the structure and fluidity of protein layers with varied relative surface coverages of crystalline and noncrystalline protein. With continuous bleaching, we measure a 10−15% decrease in the fluidity of the SLB after the full protein layer is formed. We propose that this reduction in lipid mobility is due to a small fraction (0.04) of immobilized lipids bound to the protein layer that create obstacles to membrane diffusion. Our X-ray reflectivity data show a 40 Å thick layer of protein, and we resolve an 8 Å layer separating the protein layer from the bilayer. We suggest that the separation provided by this water layer allows the underlying lipid bilayer to retain its fluidity and stability.

Introduction

The cell membrane is a heterogeneous matrix of lipids and proteins that provides a barrier between the interior of a cell and its outside environment. Self-assembled protein complexes in cell membranes have diverse functions, including structural membrane deformation[1,2] and transduction of external signals.[3] These complexes can be peripherally attached to the membrane or imbedded in the lipid bilayer; the nature of this physical arrangement can impact the overall membrane structure and fluidity.[4] An important biological function attributed to many membrane-associated proteins and protein complexes is to directly influence the membrane structure and fluidity through lipid bilayer modification or rearrangement. An example of a membrane-active protein that chemically modifies the bilayer is phospholipase A_2, which binds lipid bilayers and catalyzes the hydrolysis of phospholipids into fatty acids and single-chained lipids, thus changing the lipid composition and increasing the membrane heterogeneity.[5] In an example of protein-mediated membrane structural modification, the membrane receptor G_{M1} binds the protein cholera toxin and forms a complex on the surface of the cell membrane that assists the entry of cholera toxin into the cell.[6] To understand the biological activity of proteins in cell membranes better, it is important to study proteins interacting with lipid interfaces.

Microscopic and nanoscopic structural studies of protein complexes at membrane surfaces offer complementary insight into protein−lipid interactions. Studies of the diffusion or mobility of lipids within membranes have provided the basis for understanding the dynamics and fluidity of the lipid bilayer.[7] Fluorescence microscopy can be used to measure the mobility of lipids and demonstrates that proteins bound to lipid bilayers can moderate lipid fluidity.[8] Lipid mobility likewise influences protein complex formation, and a microscopic investigation of the growth of 2D crystals of the tetrameric protein streptavidin suggests that immobile lipids hinder the formation of protein crystals.[9] On the nanoscale, X-ray and neutron scattering provide detailed structural information that can elucidate the role of proteins at biological interfaces.[10] For example, X-ray reflectivity measurements reveal that the membrane-targeting domain of the peripheral protein cPLA-αC2 displaces water molecules from the lipid headgroups to facilitate membrane attachment and ligand binding.[11] Other studies show that single layers of a crystalline protein can intercalate lipids, resulting in a rearrangement of the lipid headgroups.[12−14] In these X-ray and neutron reflectivity examples, lipid monolayers provide the model interface for studying surface proteins.

Experimental accessibility traditionally guides the choice of the biomimetic lipid interface to study protein−lipid interactions. Whereas lipid monolayers at the air/water interface are the most common experimental system currently used for X-ray and neutron reflectivity studies, they are not as representative of cell membranes as a single lipid bilayer in the liquid phase. Stacks of multilamellar lipid membranes can mimic the fluidity of cellular

* To whom correspondence should be addressed. E-mail: mhorton@mit.edu.

[†] Ludwig-Maximilians-Universität.

[‡] Massachusetts Institute of Technology.

[§] Lehigh University.

(1) Antonny, B. *Curr. Opin. Cell Biol.* **2006**, *18*, 386−394.
(2) Farsad, K.; De Camilli, P. *Curr. Opin. Cell Biol.* **2003**, *15*, 372−381.
(3) Bray, D. *Annu. Rev. Biophys. Biomol. Struct.* **1998**, *27*, 59−75.
(4) Janmey, P. A.; Kinnunen, P. K. J. *Trends Cell Biol.* **2006**, *16*, 538−546.
(5) Mouritsen, O. G.; Andresen, T. L.; Halperin, A.; Hansen, P. L.; Jakobsen, A. F.; Jensen, U. B.; Jensen, M. Ø.; Jørgensen, K.; Kaasgaard, T.; Leidy, C.; Simonsen, A. C.; Peters, G. H.; Weiss, M. *J. Phys.: Condens. Matter* **2006**, *18*, S1293−S1304.
(6) Lencer, W. I.; Hirst, T. R.; Holmes, R. *Biochim. Biophys. Acta* **1999**, *1450*, 177−190.
(7) Edidin, M. *Nat. Rev. Mol. Cell Biol.* **2003**, *4*, 414−418.
(8) Yamazaki, V.; Sirenko, O.; Schafer, R. J.; Groves, J. T. *J. Am. Chem. Soc.* **2005**, *127*, 2826−2827.
(9) Calvert, T. L.; Leckband, D. *Langmuir* **1997**, *13*, 6737−6745.
(10) Krueger, S. *Curr. Opin. Colloid Interface Sci.* **2001**, *6*, 111−117.
(11) Málková, Š.; Long, F.; Stahelin, R. V.; Pingali, S. V.; Murray, D.; Cho, W.; Schlossman, M. L. *Biophys. J.* **2005**, *89*, 1861−1873.
(12) Vaknin, D.; Kjaer, K.; Ringsdorf, H.; Blankenburg, R.; Piepenstock, M.; Diederich, A.; Lösche, M. *Langmuir* **1993**, *9*, 1171−1174.
(13) Weygand, M.; Kjaer, K.; Howes, P. B.; Wetzer, B.; Pum, D.; Sleytr, U. B.; Lösche, M. *J. Phys. Chem. B* **2002**, *106*, 5793−5799.
(14) Weygand, M.; Wetzer, B.; Pum, D.; Sleytr, U. B.; Cuvillier, N.; Kjaer, K.; Howes, P. B.; Lösche, M. *Biophys. J.* **1999**, *76*, 458−468.

10.1021/la063690e CCC: $37.00
Published on Web 05/01/2007

membranes and provide signal amplification for X-ray analysis;[15] however, the stacked geometry complicates the study of surface-associated protein complexes. The base structure of all cell membranes is a single lipid bilayer that is often mechanically coupled to a cytoskeletal matrix, which can be approximated experimentally by a supported lipid bilayer (SLB) on a solid substrate.[16] Reflectivity characterization of a single SLB requires a sufficiently flat substrate, optimized contrast, and minimal beam damage. Neutron reflectivity offers the advantages of high contrast and little beam damage; however, X-ray reflectivity at lipid interfaces offers superior resolution.[17] We extend recent developments to resolve single SLBs with X-ray reflectivity[17−20] to study the more complex system of proteins interacting with single SLBs on both microscopic and nanoscopic scales.

We study the proteins streptavidin and avidin bound to biotinylated lipids to model peripheral membrane proteins on the surface of cell membranes. We prepare large ($\sim$cm^2) symmetric biotinylated SLBs and study them in a microfluidic device[19] that enables simultaneous in-situ characterization with X-ray reflectivity and fluorescence microscopy. Our membrane characterization combines dynamic studies of lipid diffusion in the membrane with direct structural observation of protein layer formation on both microscopic and nanoscopic scales. Streptavidin forms 2D crystals visualized among fluorescent Alexa488-conjugated avidin, which binds to the biotinylated lipids but does not crystallize.[9] By using different ratios of streptavidin to avidin, we tune the amount of crystalline versus noncrystalline protein to examine the influence of protein ordering on the mobility of the underlying lipid membrane. Previously published X-ray and neutron reflectivity studies of streptavidin bound to lipid monolayers[12,21] allow us to compare bilayer and monolayer interfaces and, in particular, the structural effect of the protein on different lipid interfaces. In addition to their use in structural studies, stable SLBs at the solid interface have potential biosensing and lab-on-a-chip applications, where a single membrane or a protein layer directly coupled to a surface can be used for measurement and analysis.[16,22]

Materials and Methods

Chemicals. The lipid 1-stearoyl-2-oleoyl-*sn*-glycero-3-phosphocholine (SOPC) was purchased from Avanti Polar Lipids (Alabaster, AL). Lipids *N*-((6-(biotinoyl)amino)hexanoyl)-1,2-dihexadecanoyl-*sn*-glycero-3-phosphoethanolamine triethylammonium salt (biotin-X-DPPE) and 1,2-dihexadecanoyl-*sn*-glycero-3-phosphoethanolamine triethylammonium salt (TR-DPPE) and proteins streptavidin, egg white avidin, and fluorescently labeled Alexa Fluor 488 avidin (Alexa488-avidin) were obtained from Invitrogen (Karlsruhe, Germany). Phosphate-buffered saline (0.01 M PBS; pH 7.4; 138 mM NaCl, 2.7 mM KCl, 10 mM Na_2HPO_4, 2 mM KH_2PO_4) was purchased from Sigma (St. Louis, MO). The buffer was prepared in deionized (DI) water from Millipore Corp. (Billerica, MA). HPLC-grade chloroform, acetone, isopropanol, and ethanol were from Carl Roth (Karlsruhe, Germany). Reagent-grade NH_4OH, 37% HCl, and H_2O_2 were purchased from Sigma.

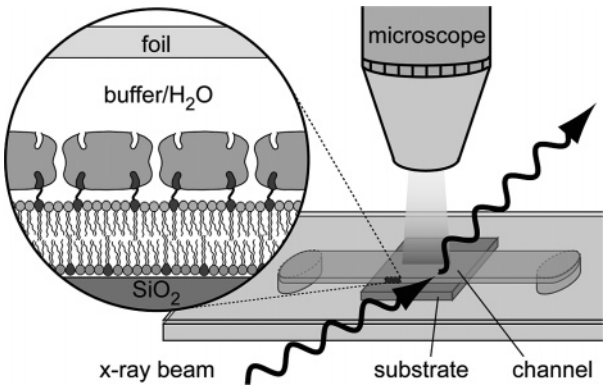

Figure 1. Schematic of the microfluidic chamber used to characterize a protein-coated SLB on an imbedded SiO_2 substrate using X-ray reflectivity and fluorescence microscopy. (Inset): Cross section of the microfluidic channel (200 μm in height) with the protein peripherally bound to the lipid bilayer.

Substrate Preparation. Silicon substrates 20 $\times$ 15 mm^2 in size and 675 μm thick were cut from polished 6 in. silicon wafers with a 100 nm thick thermal oxide layer to avoid fluorescence quenching. The substrates were cleaned by sonication in isopropanol for 10 min, followed by rinsing with DI water, and then a three-stage chemical cleaning treatment was applied. First, substrates were boiled in acetone for 10 min and then in a mixture of 1:1:5 H_2O_2/HCl/H_2O by volume for 15 min at 150 °C and then in 1:1:5 H_2O_2/NH_4OH/H_2O for 15 min at 150 °C. After each step, the substrates were rinsed with DI water. After cleaning, the substrates were stored in DI water for later use.

Spin Coating. The lipid mixture 89.5 mol % SOPC, 10 mol % biotin-X-DPPE, and 0.5 mol % TR-DPPE was prepared in chloroform and 3 mg total lipid was placed in clean glass vials. The chloroform was evaporated from each vial in a nitrogen stream, followed by evacuation in a vacuum chamber for at least 12 h. Dried lipids were then redissolved in isopropanol to a final concentration of 1.5 mg/mL for spin coating. This concentration ensures the formation of a complete single bilayer.[23] Unlike chloroform, isopropanol completely wets the hydrophilic silicon substrates. To coat the substrates, 200 μL of lipid solution was dropped onto a clean silicon substrate in a Delta 10 spin-coater from BLE Lab Equipment (Radolfzell, Germany). The substrate was immediately accelerated with the following profile: a ramp from 0 to 2000 rpm was driven for 2 s, followed by another ramp from 2000 to 3000 rpm for 2 s. Then the sample was spun at constant velocity of 3000 rpm for another 118 s. After spin-coating, the substrates were placed in a vacuum chamber for at least 4 h to ensure complete evaporation of the isopropanol.

Microfluidic Chamber Assembly. The dry spin-coated substrates were glued into plastic microfluidic chambers purchased from ibidi GmbH (München, Germany)[19] using two-component UHU epoxy glue that hardens in 5 min (Bühl, Germany). After allowing the epoxy glue to dry for 30 min, the chambers with glued-in substrates were placed under vacuum for 6 h for final hardening. The microfluidic channels were then flushed several times with DI water to hydrate the supported lipid bilayers (SLBs) and to flush away excess lipids. The geometry of the microfluidic chamber with the imbedded SiO_2 substrate is shown in Figure 1.

Protein Layer Formation on SLBs. The SLBs were rinsed in the microfluidic chambers five times with PBS buffer, and then 1 mL of a protein solution in PBS buffer at a protein concentration of 40 μg/mL was pipetted into channels to allow protein layers to form on the SLBs. The SLBs were left undisturbed to incubate in protein mixtures for more than 12 h at 30 °C.

X-ray Reflectivity. X-ray reflectivity measurements were performed at the undulator beamline ID01 at the European Synchrotron Radiation Facility (ESRF) in Grenoble, France. An X-ray energy of 19.9 keV (λ = 0.623 Å) was chosen to maximize the reflectivity

(15) Salditt, T. *Curr. Opin. Struct. Biol.* **2003**, *13*, 467−478.
(16) Sackmann, E. *Science* **1996**, *271*, 43−48.
(17) Miller, C. E.; Majewski, J.; Gog, T.; Kuhl, T. L. *Phys. Rev. Lett.* **2005**, *94*, 238104.
(18) Nováková, E.; Giewekemeyer, K.; Salditt, T. *Phys. Rev. E* **2006**, *74*, 051911.
(19) Reich, C.; Hochrein, M.; Krause, B.; Nickel, B. *Rev. Sci. Instrum.* **2005**, *76*, 095103.
(20) Vogel, M.; Münster, C.; Fenzl, W.; Salditt, T. *Phys. Rev. Lett.* **2000**, *84*, 390−393.
(21) Lösche, M.; Piepenstock, M.; Diederich, A.; Grünewald, T.; Kjaer, K.; Vaknin, D. *Biophys. J.* **1993**, *65*, 2160−2177.
(22) Astier, Y.; Bayley, H.; Howorka, S. *Curr. Opin. Chem. Biol.* **2005**, *9*, 576−584.
(23) Mennicke, U.; Salditt, T. *Langmuir* **2002**, *18*, 8172−8177.

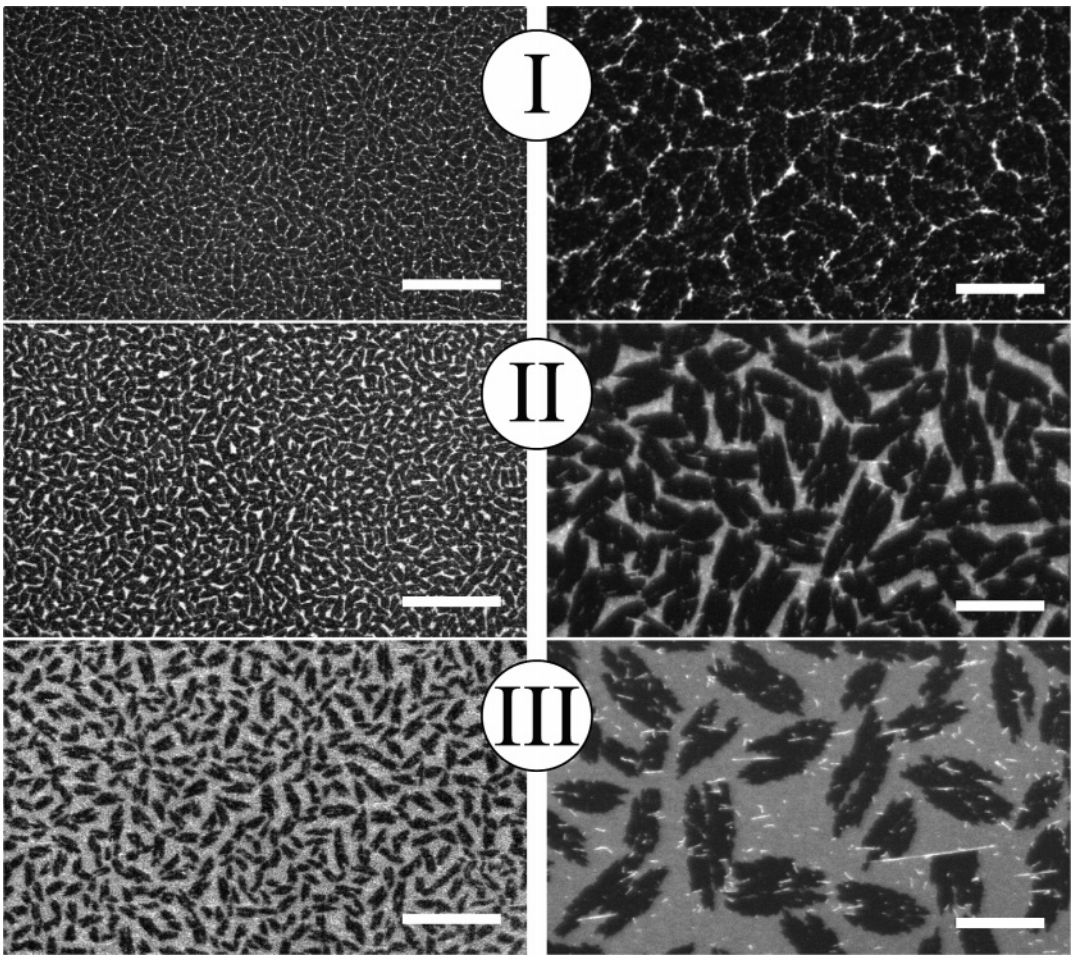

Figure 2. Fluorescence micrographs showing dark crystalline streptavidin domains in a bright Alexa488-avidin matrix bound to SLBs imaged with 10× (left column) and 63× (right column) objectives. SLBs are incubated in protein mixtures with streptavidin/avidin/Alexa488-avidin molar ratios of (I) 92/0/8, (II) 56/36/9, and (III) 12/78/10. Scale bars are 100 μm in the left column and 20 μm in the right column.

signal while minimizing the beam damage in the microfluidic chambers.[19] Sample chambers were mounted in a horizontal scattering geometry with a vertical plane of incidence. The beam cross section was limited by a presample aperture of 200 × 1000 μm^2 (vertical × horizontal); the relatively large beam size ensures a wide illumination of the surface area even at higher grazing angles of incidence. A small vertical postsample aperture was used to completely suppress reflectivity from the thin top foil of the sample chamber (Figure 1). Evacuated beam guides with Kapton windows positioned close to the sample chamber minimized air scattering, and the reflected intensity was collected with a NaI detector. Data were normalized by the Fresnel reflectivity (R_F), where

$$R_F = \left| \frac{1 - \sqrt{1 - (q_c/q_z)^2}}{1 + \sqrt{1 - (q_c/q_z)^2}} \right|^2 \quad (1)$$

The momentum transfer at the critical angle of total external reflection is q_c, and q_z is the momentum transfer perpendicular to the interface. Using Parratt's method,[24] the reflectivity was fit with a slab model, where within each slab the electron density and thickness are uniform. The interfaces between the different slabs were smeared with a surface roughness[25] of 3 Å.

Fluorescence Microscopy. Fluorescence microscopy was performed on site at the ESRF using a transportable Zeiss Axiotech vario fluorescence microscope (Oberkochen, Germany) equipped with 10× (NA 0.3) and long-distance 63× (NA 0.75) Plan-Neofluar objectives. Images were captured with an ORCA C4742-95 CCD camera and WASABI imaging software from Hamamatsu Photonics (Tutzing, Germany). For continuous bleaching experiments, a mercury lamp was aligned to ensure even illumination of the sample. Continuous bleaching data were analyzed using MATLAB software from Mathworks (Cambridge, MA).

Results

Fluorescence Microscopy. We first characterize the proper formation of the lipid bilayer membrane and the protein layer with fluorescence microscopy. After the SLBs are incubated in protein and the chambers are flushed to remove proteins from the solution, fluorescence microscopy provides direct evidence of the formation of the protein layers on the SLBs. We see dark crystalline streptavidin domains among fluorescently labeled avidin in Figure 2. Qualitative observation of the protein crystals in Figure 2 gives insight into the overall quality and fluidity of the SLBs. The surface coverage of the streptavidin clearly increases as the ratio of streptavidin to avidin in the incubation solution is increased. The crystals in Figure 2II, III exhibit the characteristic X and H shapes of streptavidin crystals with *C*222 symmetry observed on monolayers under similar solution conditions.[26−28] At low microscopic resolution at each protein concentration (Figure 2, left column), the density of the crystals is constant across the membrane, suggesting that the nucleation

(24) Parratt, L. G. *Phys. Rev.* **1954**, *95*, 359−369.
(25) Nevot, L.; Croce, P. *Rev. Phys. Appl.* **1980**, *15*, 761−780.
(26) Ku, A. C.; Darst, S. A.; Kornberg, R. D.; Robertson, C. R.; Gast, A. P. *Langmuir* **1992**, *8*, 2357−2360.
(27) Ratanabanangkoon, P.; Gast, A. P. *Langmuir* **2003**, *19*, 1794−1801.
(28) Wang, S.-W.; Robertson, C. R.; Gast, A. P. *Langmuir* **1999**, *15*, 1541−1548.

density and the growth rate of the crystals are uniform. Because the nucleation of microscopic protein crystals is sensitive to lipid mobility and substrate roughness,[9] the uniformity of the streptavidin crystalline domains demonstrates that the SLBs and the substrate are spatially uniform. Crystalline domains at lower streptavidin surface coverages (Figure 2II, III) have an average length of approximately 15 μm and an average length to width aspect ratio of approximately 2. Characterizing the shapes of the streptavidin domains at high surface coverage is more difficult because the domains grow to near confluence (Figure 2I). Previous experiments in monolayers[26] and bilayers[9] also show that high surface coverage of streptavidin results in morphologically indistinguishable domains as a result of the dendritic growth of the crystals.

Continuous Bleaching. Whereas the formation of microscopic crystalline domains indicates that our membranes are fluid, we also quantitatively measure the diffusion constants of the lipid bilayers with and without bound protein layers to characterize the dynamics of the membrane. The continuous bleaching method[29,30] is particularly convenient because it employs the same microscope setup that we use for fluorescence microscopy. According to the theory of continuous bleaching, the spatial intensity of a fluorescently labeled membrane subjected to constant and even illumination is described by simultaneous photobleaching and replenishment of fluorescent molecules via 2D diffusion.

We illuminate a defined region of the SLB that is approximately 180 μm in diameter (d) at 63× magnification (Figure 3a, right). This area is continuously illuminated, and as the fluorescent lipid molecule TR-DPPE is photobleached, the fluorescence intensity, $I_{d/2}$, of the SLB in the center of the illuminated area ($d/2$), decays exponentially as a function of exposure time (t) according to the equation

$$I_{d/2}(t) = I_{t0}e^{-B_0 t} = I_{t0}e^{-\tau} \qquad (2)$$

I_{t0} is the initial fluorescence intensity at the center of the illuminated area, B_0 is the bleaching rate, and τ is the dimensionless time $\tau = B_0 t$. We calculate I_{t0} from the average intensity of an area approximately 15 μm in diameter in the center of the sample, represented by circles in the SLB micrographs in Figure 3a. The fluorescence intensity $I_{d/2}$ is determined from subtracting the background fluorescence measured in the nonilluminated part of the image, A_1, from the actual measured intensity in the center of the sample, $I_{\text{total},d/2}$, and $I_{d/2} = I_{\text{total},d/2} - A_1$. We calculate B_0, which depends on the fluorescent dye, solution conditions, and illumination energy, by fitting eq 2 to the time-resolved intensity in the center of the sample $I_{d/2}$ for each continuous bleaching measurement. The plot of $I_{d/2}$ as a function of time is presented in Figure 3b with the dashed line calculated from eq 1, illustrating how first-order behavior persists up to approximately 300 s. At longer times, the fluorescence intensity measured at the center of the membrane $I_{d/2}$ approaches the background fluorescence A_1, indicating that the center of the membrane is fully bleached.

As the sample is bleached, a bright rim appears at the edge of the image (Figure 3a, bottom right) as TR-DPPE molecules diffuse into the illuminated area. Once the center fluorescence intensity approaches the background fluorescence and remains constant at approximately $\tau > 20$, we fit the fluorescence intensity line profile through the sample as a function of distance, x,

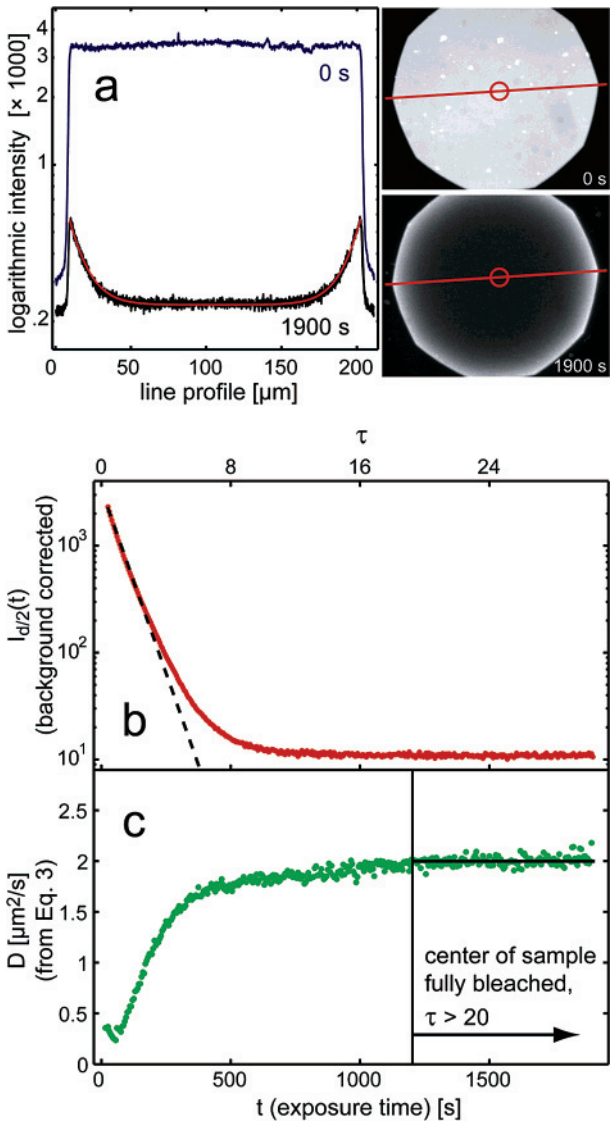

Figure 3. Example of the continuous bleaching measurement of lipid diffusion in an SLB coated with a protein layer with a 92/8 streptavidin/Alexa488-avidin molar ratio. (a) Line intensity profiles and corresponding micrographs at the onset of illumination (0 s) and at the end of the experiment (1900 s). The fit to the line profile at 1900 s from eq 3 is shown in red. (b) Time evolution of the background-corrected fluorescence intensity in the center of the sample used to determine the bleaching rate B_0, where the dashed line is a fit according to eq 2. (c) Diffusion constant D extracted from fitting line intensity profiles at a 5 s time interval to eq 3. The longer time regime ($t > 20$) is indicated when the center of the sample is fully bleached and eq 3 is valid for calculating D.

according to the equation[29]

$$I(x) = I_{x0}\cosh\left[\sqrt{\frac{B_0}{D}}\left(x - \frac{d}{2}\right)\right] + A_2 \qquad (3)$$

The fluorescence intensity at the edge of the rim is I_{x0}, D is the diffusion constant, and A_2 is a constant we use to fit eq 3.[29] Diffusion constants extracted by fitting eq 3 to the line profiles at 5 s intervals are plotted in Figure 3c. The fit of eq 3 to a line profile is shown in Figure 3a. According to the original development of continuous bleaching theory, eq 3 can be used to calculate D accurately only at longer times, when the center of the sample is completely bleached.[29] This time regime for our experiments is indicated in Figure 3c and is represented qualitatively by the plateau of extracted D values at $\tau > 20$. To

(29) Dietrich, C.; Merkel, R.; Tampé, R. *Biophys. J.* **1997**, *72*, 1701−1710.
(30) Hochrein, M.; Reich, C.; Krause, B.; Rädler, J.; Nickel, B. *Langmuir* **2006**, *22*, 538−545.

Table 1. Lipid Diffusion Constants Determined by Continuous Bleaching[a]

composition of protein solution	diffusion constant, D (μm^2/s)
no protein (bare SLB)	2.3 ± 0.4
92 mol % streptavidin, 8 mol % avidin	2.0 ± 0.1
56 mol % streptavidin, 44 mol % avidin	1.9 ± 0.1
12 mol % streptavidin, 88 mol % avidin	1.9 ± 0.1
100% avidin	2.0 ± 0.1

[a] Diffusion constants are calculated by fitting eqs 2 and 3 to continuous bleaching data. SLBs are incubated in protein solutions with the compositions listed; total mol % avidin comprises 8−10 mol % Alexa488-avidin, and the balance is egg white avidin. Three different time-resolved line profiles are measured for every sample, each corresponding to $N > 20$ calculations of D. The error is estimated as the experimental standard deviation.

obtain data suitable for robust quantitative analysis, extra care must be taken to ensure even sample illumination and a flat initial line profile (Figure 3a), and the center of the sample must be completely bleached to the background level to calculate the diffusion constant D.

Using this continuous bleaching method and analysis, we reproducibly measure the diffusion constants of our SLBs to investigate whether a bound protein layer changes the fluidity of the bilayer. Table 1 lists the lipid diffusion constants of the SLBs. We determine that the protein binding to the SLB results in a slight decrease in lipid mobility, as shown by the 10−15% reduction in lipid diffusion constants when a protein layer is present. The composition of the protein mixture and hence the area coverage of crystalline protein do not have a measurable effect on lipid mobility. We are also unable to detect an immobile fraction of lipids; after our continuous bleaching experiments, the SLBs recover to their full original fluorescence after 8 h.

We also investigate whether the protein molecules within the bound protein layers are mobile by using fluorescently labeled avidin as a tracer molecule. When we continuously illuminate the protein layer on the SLBs at 488 nm, corresponding to the excitation energy of Alexa488-avidin, we do not observe the bright rim at the sample edge characteristic of a fluid membrane. Instead, the illuminated area, viewed after 1 h of bleaching, has a sharp outline and a flat fluorescence intensity profile, indicating no diffusion of Alexa488-avidin (data not shown). Note that because of the high photostability of the Alexa dye there is only minimal photobleaching. This immobility is observed for all protein layers, and time-resolved images show that the streptavidin domains do not translate or rotate, further indicating the immobility of the protein layer. By simple comparison of the estimated relative sizes of a lipid molecule (7 Å) and a single protein molecule (50 Å),[31] we expect the diffusion constant of the bound protein to be lower than that of the underlying lipids. This size difference between lipid and protein diverges further as streptavidin crystallizes and the size of the protein crystal increases. The mobility of the protein molecules can also be hindered by collisions with adjacent proteins at the high protein surface coverage in these experiments. Our observation that the proteins within the protein layer are immobilized relative to the lipids is consistent with previous observations: proteins attached to membranes at high surface coverages can diffuse 20−100 times slower than lipids.[26] It is therefore reasonable that the mobility of the proteins is significantly lower than that of the underlying lipids that are not bound to the protein.

X-ray Reflectivity. To further complement the microscopic dynamic and structural insight from fluorescence microscopy

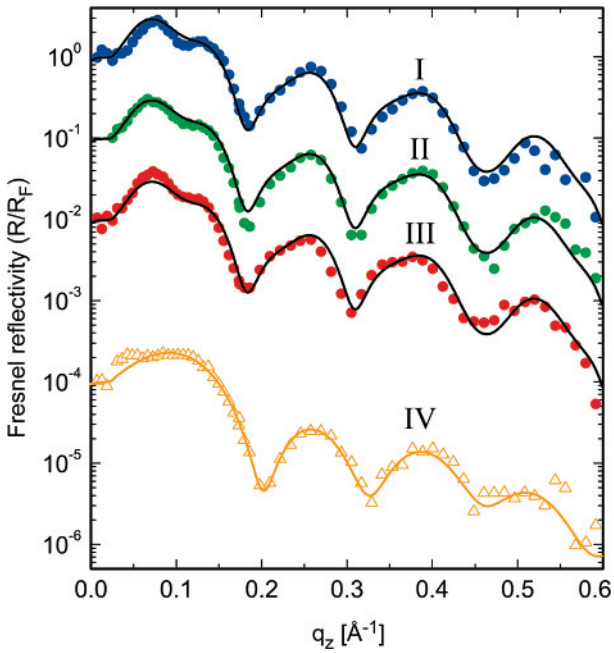

Figure 4. Normalized reflectivity scans of protein-coated (I−III) and bare (IV) SLBs. Protein-coated SLBs (I−III) have a signature dip at q_z = 0.1 Å^{-1}. SLBs coated with protein mixtures with streptavidin/avidin/Alexa488-avidin molar ratios of (I, blue) 92/0/8, (II, green) 56/36/9, and (III, red) 12/78/10. The common reflectivity fit is plotted with the data sets in I−III to illustrate the similarity of the streptavidin and avidin-protein layers. The reflectivity of a bare SLB lacking protein (IV) is shown with its fit (orange curve). Plots are shifted vertically for clarity, and all data are background corrected and normalized by the Fresnel reflectivity, R_F.

characterization, we use X-ray reflectivity to determine the structure of the protein and the underlying bilayer in nanoscopic detail. In Figure 4, we compare the reflectivity of bare and protein-coated bilayers. The main signature of the protein layers in Figure 4I−III is the dip in the reflectivity curve at $q_z = 0.1$ Å^{-1}, indicating an additional layer on the lipid bilayer membrane that is not present in our scan of the bare bilayer (Figure 4(IV)). To extract structural details of the protein layers and SLBs, we fit the X-ray reflectivity data using Parratt's formalism, where the interface is modeled as a series of slabs of varying thickness and electron density.[24] These parameters for each slab are independently varied, and a nonlinear least-squares fitting routine is used to fit the reflectivity. All slab profiles are smoothed by an overall roughness[25] of 3 Å. We model the SLBs with seven slabs: two slabs for each headgroup layer, one slab for each acyl chain layer, and one slab for the space between leaflets. Protein-coated SLBs are modeled with an additional four slabs: the region between the upper surface of the SLB and the bottom of the peripheral protein layer is one slab, and we use three slabs to model the protein layer.

From initial observation, the reflectivity data from protein-coated SLBs with different protein layer compositions shown in Figure 4I−III are nearly indistinguishable. We tested this structural similarity by fitting all reflectivity data of protein-coated bilayers to a single depth profile based on the same slab model. We plot this common profile with data from each protein composition in Figure 4I−III. To verify that this common profile reasonably approximates all of the different protein compositions, we also independently fitted the scans for each protein composition, allowing the thickness and density of each slab to vary. The resulting electron density profiles of the different protein mixtures were identical within the precision of our measurements. The similar reflectivity of different ratios of avidin and streptavidin

(31) Hendrickson, W. A.; Pähler, A.; Smith, J. L.; Satow, Y.; Merritt, E. A.; Phizackerley, R. P. *Proc. Natl. Acad. Sci. U.S.A.* **1989**, *86*, 2190−2194.

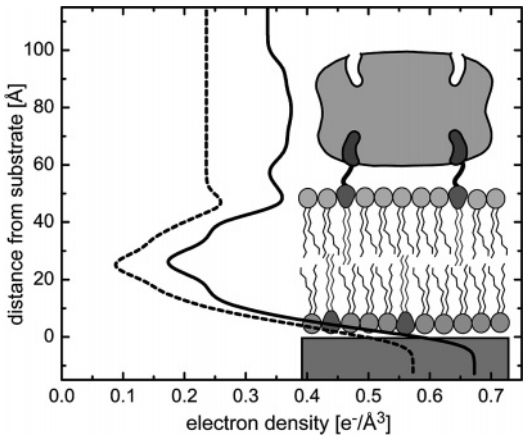

Figure 5. Electron density profiles of SLBs with a protein layer (black) and without protein (dashed line) extracted from the fitting of the reflectivity. The common depth profile for the protein-coated SLB is shown (black). The protein layer is identified by a plateau of increased electron density not seen on the bare SLB. The thickness of the protein layer is 40 Å; the water layer separating the protein from the SLB is 8 Å thick. The electron density axis is correctly aligned for the protein-coated SLB (black), and the profile of the bare SLB (dashed line) is shifted left by 0.1 $e^-/Å^3$ for clarity.

is not surprising because avidin and streptavidin have similar structures;[32] 33% of the residues are the same, and their biotin-binding sites are nearly identical.[33] This structural similarity, combined with the fact that our reflectivity scans are measured with an incident beam footprint on the membrane of ~1 mm^2, makes avidin and streptavidin indistinguishable by our measurements. Thus, our X-ray reflectivity fits do not take into account the segregation of the proteins once crystals are formed.

In Figure 5, we present the electron density profiles extracted from the reflectivity fits of both protein-coated (solid curve) and bare SLBs (dashed curve) with a corresponding sketch of a protein molecule bound to an SLB. The common depth profile of the protein-coated SLB is shown, representing both streptavidin and avidin (Figure 5, solid curve). The distinguishing feature in the electron density profile of the protein-coated SLBs is the increase in electron density at a distance of 55−95 Å from the substrate. This relatively electron-dense layer corresponds to a 40 Å thick protein layer on the SLB. By contrast, the electron density profile of bare SOPC/biotin-X-DPPE in this region (Figure 5, dashed curve) is at the level of the water. The protein thickness that we measure is comparable to previous X-ray and neutron reflectivity studies of streptavidin crystallized on monolayers, where 40−44 Å is reported,[12,21,34] similar to the thickness of avidin measured by X-ray crystallography[32] of 40 Å.

Our reflectivity measurements also reveal a thin 8 Å layer separating the protein from the lipid bilayer. Because our dynamic range extends up to $q_{max} = 0.6$ $Å^{-1}$ and the spatial resolution of the electron density profile, d_{min}, can be estimated by the sampling theorem[35] as $d_{min} = \pi/q_{max}$, our resolution is $d_{min} =$ 5 Å, allowing us to resolve this space between the protein and the SLB. This hydrated layer is structurally distinct from the headgroups and protein layer because the electron density in this space approaches the bulk water density.

Discussion

We form large stable arrays of protein crystals on single supported lipid bilayers suitable for simultaneous microscopy and X-ray reflectivity characterization for over 48 h. We characterize the protein-coated SLBs using both methods to study the dynamics and structure of this interface on both microscopic and nanoscopic scales. Lipid bilayer stability is required for the time-resolved investigation of biological self-assembly at interfaces. In developing a biomimetic interface for studying protein complexes interacting with lipids, the large surface coverage of the bilayer also becomes important because both reflectivity and microscopy require homogeneous samples of ~100 μm^2 dimension. Fluorescence micrographs (Figure 1) provide direct evidence of high substrate surface coverage of both proteins and lipids.

Using the complementary insight from our combined microscopic and X-ray characterization of protein-coated membranes, we can describe how the protein layer interacts with the lipid bilayer in greater detail. Because streptavidin and avidin irreversibly bind the headgroups of biotin-X-DPPE lipids and are immobile relative to the lipid molecules, we can also expect the lipids bound to the peripheral protein to be immobilized. If the approximate area per lipid headgroup is 50 $Å^2$ and each protein molecule is 50 × 50 $Å^2$ in area, then the footprint of the protein is approximately 50 lipids, assuming approximately equal areas of SOPC and biotin-X-DPPE headgroups. Bivalent binding of the protein then suggests that 4 mol % of the lipids are immobilized by protein binding.

Previous theoretical and computational studies of diffusion among obstacles provide a framework for understanding how immobilizing lipids by protein binding can influence diffusion in the underlying bilayer. If we assume that the lipids bound to the protein layer are fixed obstacles around which the bulk lipids must diffuse, then we can first consider the diffusion of lipids in a bilayer as a random walk on a square lattice, where the immobilized lipids are represented by excluded lattice sites. Although it is possible that the lipids in the individual leaflets have different diffusion constants, recent studies suggest strong coupling between the leaflets of SLBs and that molecular friction between the proximal leaflet and the substrate can reduce diffusion constants[36,37] by 5%. Thus, we assume that our measured 10−15% reduction in diffusion is representative of the outer leaflet containing the obstacles. This system of diffusion among obstacles has been studied theoretically[38] and simulated with lipid bilayers.[39] The following expression[38] describes the ratio of the diffusion constant with obstacles, D, to the diffusion constant without obstacles, D_0:

$$\frac{D}{D_0} = 1 - (\pi - 1)c - 8.5571c^2 \qquad (4)$$

Applying this theory to our lipid bilayers, where we have found that the protein layer reduces the diffusion constant of the SLB from $D_0 = 2.3$ $\mu m^2/s$ to $D = 2.0$ $\mu m^2/s$, we calculate an area fraction of immobilized lipids of $c = 0.02-0.09$ from eq 4, with the error in D/D_0 estimated to be 10%. This estimate of the area fraction of immobilized lipids is in agreement with our geometry-based estimate of 0.04.

(32) Rosano, C.; Arioso, P.; Bolognesi, M. *Biomol. Eng.* **1999**, *16*, 5−12.
(33) Green, N. M. *Methods Enzymol.* **1990**, *184*, 51−67.
(34) Vaknin, D.; Als-Nielsen, J.; Piepenstock, M.; Lösche, M. *Biophys. J.* **1991**, *60*, 1545−1552.
(35) Als-Nielsen, J.; McMorrow, D. *Elements of Modern X-Ray Physics*; John Wiley & Sons Ltd: West Sussex, England, 2001.
(36) Zhang, L.; Granick, S. *Proc. Natl. Acad. Sci. U.S.A.* **2005**, *102*, 9118−9121.
(37) Zhang, L.; Granick, S. *J. Chem. Phys.* **2005**, *123*, 211104.
(38) Nieuwenhuizen, T. M.; van Velthoven, P. F. J.; Ernst, M. H. *Phys. Rev. Lett.* **1986**, *57*, 2477−2480.
(39) Saxton, M. J. *Biophys. J.* **1994**, *66*, 394−401.

To further explore this mechanism of lipid diffusion among obstacles created by protein−lipid binding, we consider an additional theoretical model of lipid diffusion among immobilized lipids that takes into account the possibility of lipids clustering around each obstacle.[40] The phenomenon of lipids ordering around immobilized lipids is demonstrated by recent experimental investigations of large molecules adsorbed onto lipid membranes, where the lipids directly under the adsorbed molecule diffuse as a unit with slower characteristic diffusion times than for lipids in the surrounding bare membrane.[36] In the theoretical model considering lipid ordering, each immobilized obstacle of radius R has a coherence length of ξ, which describes an annular region of lipids ordered around the obstacle. The ratio of diffusion constants with and without obstacles is then described by the following equations:[40]

$$\frac{D}{D_0} = 1 + ac + bc^2 \tag{5}$$

$$a = -1.208 - 24.3\exp\left(\frac{-1.763R}{\xi}\right) - 2.408\exp\left(\frac{-0.3138R}{\xi}\right) \tag{6}$$

$$b = 185\exp\left(\frac{-2.587R}{\xi}\right) \tag{7}$$

Using a lipid radius of $R = 3.5$ Å and a fraction area coverage of immobilized lipids of $c = 0.04$, we calculate that the coherence length is $\xi = 2$ Å. A coherence length smaller than the radius of a single lipid headgroup indicates that there is no ordering of the fluid lipids around these immobilized lipids.[41] We can reasonably estimate our measured reduction of diffusion without considering protein−lipid interactions beyond the immobilization of the lipids directly bound to the protein. Therefore, the bulk lipids do not seem to be affected by the bound protein layer.

In presenting a complete physical picture of our system, the hydrated layer separating the protein from the lipids becomes important. The molecular contents of this layer are water and the spacer of the biotin-X-DPPE separating biotin from the headgroup. We propose that because this water layer separates the immobile protein layer anchored to the underlying fluid lipid bilayer, the dominant protein−lipid interaction that we observe is the binding to the biotinylated lipids. Our observations are remarkably different than the previous effects reported for streptavidin bound to monolayers at the air/water interface, where streptavidin binding results in major lipid tilting and rearrangement, resulting in an overall reduced monolayer thickness.[12,21] In contrast to monolayers, our stable lipid bilayers cannot easily adjust surface pressure and density in response to ligand binding and resist dramatic thinning and the collapse of membrane leaflets. We measure no changes in the acyl chain region of the lipid bilayer before and after protein binding, further indicating the stability of the interface. We suggest that lipid bilayers are more representative of cell membranes than monolayers and are more appropriate for studying protein−membrane interactions because we also expect the lipid bilayers in cells to retain their structural integrity upon protein binding and to be stabilized against leaflet collapse.

Interestingly, the fluidity and structure of lipid bilayers with noncrystalline avidin and microscopic crystalline streptavidin domains are similar. Both protein coatings are qualitatively immobile or frozen and cause the same slight decrease in the fluidity of the underlying lipids. Although we would expect noncrystalline avidin to be more mobile than streptavidin molecules confined to crystalline domains, in our model, all bound protein molecules are immobilized relative to the underlying SLB once the protein layer is formed.

Conclusions

We concomitantly characterize the structure and dynamics of a single protein layer bound to a single SLB with fluorescence microscopy and X-ray reflectivity. We demonstrate a method of characterizing proteins interacting with single lipid bilayers at the solid interface; this biomimetic membrane is more representative of cell membranes than lipid monolayers and can be extended to study more complex protein−lipid systems. By resolving the layer separating the streptavidin and avidin from the SLBs, we demonstrate that the lipid−protein interaction is primarily through direct binding to the ligand, in contrast to leaflet collapse effects observed from similar systems in lipid monolayers. Measurement of the slight reduction of the diffusion constant in the lipid bilayer provides further evidence that proteins affect only the immobilized lipids. In our protein-coated membranes, streptavidin and avidin are specifically bound to a fluid interface with a defined orientation. This may provide a platform for biosensing applications that is superior to simple solid-supported protein interfaces. We plan to expand our work on surface-associated proteins to transmembrane and intercalating proteins, and we are extending this in-situ technique to characterize the more complex system of protein complexes on SLBs tethered to polymer cushions.

Acknowledgment. We acknowledge the European Synchrotron Radiation Facility for the provision of synchrotron radiation facilities, and we thank Till H. Metzger for assistance in using beamline ID01 and Harald Müller for assistance in the chemistry laboratory. We are grateful to Ellen Reister-Gottfried and Udo Seifert for locating essential references on obstacle-hindered diffusion. We thank Erich Sackmann for insightful discussions of diffusion at solid interfaces and Christian Daniel for discussions of continuous bleaching. This work was funded in part through the Robert T. Haslam Chair at MIT, the German Federal Ministry of Education and Research (BMBF 03RA6LMU), and the International Graduate School (IDK).

LA063690E

(40) Almeida, P. F. F.; Vaz, W. L. C.; Thompson, T. E. *Biochemistry* **1992**, *31*, 7198−7210.

(41) Deverall, M. A.; Gindl, E.; Sinner, E.-K.; Besir, H.; Ruehe, J.; Saxton, M. J.; Naumann, C. A. *Biophys. J.* **2005**, *88*, 1875−1886.

A.5 Full text of Ref. [5]

Christian Reich, Margaret R. Horton, Bärbel Krause, Alice P. Gast, Joachim O. Rädler and Bert Nickel

Condensation, stretching and asymmetry: G_{M1} and cholesterol in single supported lipid bilayers.

Submitted on May 18, 2007.

Abstract:
The membrane of living cells comprises numerous protein and lipid molecules capable of liquid-liquid phase separation and asymmetric organization between leaflets, resulting in structural heterogeneity. We model cell membranes using supported lipid bilayers (SLBs) to study the structural effects of cholesterol and the ganglioside receptor G_{M1} along the full membrane depth profile with nanoscale resolution using synchrotron reflectivity. Ganglioside G_{M1} resides in the outer cell membrane leaflet and is thought to partition into liquid-ordered phases and promote membrane condensation. We compare the structure of single-component SLBs with and without asymmetrically inserted G_{M1}, mimicking the receptor orientation in cell membranes. Using ternary lipid mixtures of cholesterol, brain sphingomyelin and 1,2-dioleoyl-*sn*-glycero-3-phosphocholine, we resolve the structural differences between condensed and non-condensed SLBs in terms of acyl chain packing density and thickness. We show that asymmetric incorporation of G_{M1} into these SLBs has a condensing effect on the leaflet in which it is present and reduces the lipid diffusion within the SLB, as measured by continuous bleaching using fluorescence microscopy. These results show that X-ray reflectivity is an effective tool for resolving separate condensation states in different membrane leaflets induced by the presence of membrane receptors.

Condensation, stretching and asymmetry: G_{M1} and cholesterol in single supported lipid bilayers

Christian Reich*,
Department für Physik, Ludwig-Maximilians-Universität,
München, Germany

Margaret R. Horton†
Department of Chemical Engineering, Massachusetts Institute of Technology,
Cambridge, Massachusetts

Bärbel Krause‡
European Synchrotron Radiation Facility,
Grenoble, France

Alice P. Gast
Department of Chemical Engineering, Lehigh University,
Bethlehem, Pennsylvania

Joachim O. Rädler and Bert Nickel
Department für Physik, Ludwig-Maximilians-Universität,
München, Germany

May 17, 2007

*Corresponding author. Full address: Department für Physik, Ludwig-Maximilians-Universität, Geschwister-Scholl-Platz 1, D-80539 München, Germany, Tel.: (+49) 89 2180-1453, Fax: (+49) 89 2180-1452, E-mail: creich@lmu.de

†Present address: Department für Physik, Ludwig-Maximilians-Universität

‡Present address: Carl Zeiss AG, Oberkochen, Germany

Abstract

The membrane of living cells comprises numerous protein and lipid molecules capable of liquid-liquid phase separation and asymmetric organization between leaflets, resulting in structural heterogeneity. We model cell membranes using supported lipid bilayers (SLBs) to study the structural effects of cholesterol and the ganglioside receptor G_{M1} along the full membrane depth profile with nanoscale resolution using synchrotron reflectivity. Ganglioside G_{M1} resides in the outer cell membrane leaflet and is thought to partition into liquid-ordered phases and promote membrane condensation. We compare the structure of single-component SLBs with and without asymmetrically inserted G_{M1}, mimicking the receptor orientation in cell membranes. Using ternary lipid mixtures of cholesterol, brain sphingomyelin and 1,2-dioleoyl-*sn*-glycero-3-phosphocholine, we resolve the structural differences between condensed and non-condensed SLBs in terms of acyl chain packing density and thickness. We show that asymmetric incorporation of G_{M1} into these SLBs has a condensing effect on the leaflet in which it is present and reduces the lipid diffusion within the SLB, as measured by continuous bleaching using fluorescence microscopy. These results show that X-ray reflectivity is an effective tool for resolving separate condensation states in different membrane leaflets induced by the presence of membrane receptors.

Key words: X-ray reflectivity; solid-liquid interface; lipid rafts; fluorescence microscopy; lipid diffusion.

Introduction

Cell membranes are highly heterogeneous structures with numerous lipid and protein species. This heterogeneity is reflected in asymmetric lipid compositions in the inner and outer leaflets of the plasma membrane. Within mammalian membrane leaflets, the degree of saturation and the length of the lipid acyl chains vary among molecules and can locally affect the membrane thickness and induce lateral heterogeneity (1). The major constituents of the outer membrane leaflet of mammalian cells (phospholipids, sphingomyelin and cholesterol) are capable of phase separation due to attractive interactions between cholesterol and sphingomyelin (2–4). Cholesterol preferentially localizes to the vicinity of sphingomyelin due to hydrogen bonding between the hydroxyl group of the sphingosine backbone and the polar moiety of the sterol (5, 6). The relatively rigid structure of cholesterol and its ability to fit into the interstitial space between the saturated acyl chains of sphingomyelin tighten lipid packing and result in a cholesterol-enriched liquid-ordered phase (L_o) (6), in coexistence with a cholesterol-depleted liquid-disordered phase (L_d) which contains mainly unsaturated phospholipids. L_o domains, commonly referred to as lipid rafts (2), are thought to play a role in membrane organization by concentrating different receptor molecules into certain lipid environments (7).

The monosialoganglioside G_{M1} is the receptor for cholera toxin entering the cell through the endocytic pathway and has been shown to localize to raft domains in the outer membrane leaflet (8). The asymmetric localization of receptors within L_o or L_d phases is governed by intermolecular interactions within the membrane. The particular preference of G_{M1} to partition into the ordered L_o phase is likely due to its saturated acyl chains, although specific interactions of its large oligosaccharide headgroup with nearby sphingomyelin and phosphocholine headgroups may also play a role (7). The leaflet asymmetry of G_{M1} may also induce an asymmetric distribution of cholesterol, whose exact transbilayer distribution is not known (6). Molecular-level structural methods are necessary to measure leaflet asymmetry and to precisely determine how cholesterol and receptor molecules modify the lipid bilayer structure.

The complex structure of cell membranes often inhibits discrete experimental studies of lipid-lipid interactions. Successful efforts to systematically study intermolecular interactions have been made using simplified biomimetic membranes, which can be engineered with multiple components and lipid asymmetry among the leaflets, mimicking the structure and function of cell membranes. A special class of biomimetic membranes are solid supported lipid bilayers (SLBs) which have proven particularly useful for the application of surface sensitive techiques, such as atomic force microscopy (AFM) (9), X-ray and neutron diffraction (10) and methods based on fluorescence microscopy (11–13). Experimental evidence for condensation of L_o domains in SLBs has been obtained using AFM, where a relative increase in the height of the L_o phase of 8 Å with respect to the surrounding L_d phase (14, 15) has been reported. In SLBs containing model lipid raft domains and symmetrically distributed G_{M1}, a height difference of 20 Å between G_{M1}-enriched domains and the surrounding bilayer has been reported (16). However, these AFM studies do not permit conclusions about the absolute thicknesses and densities of the SLBs and it remains unclear whether the observed height differences originate from a stretching effect of the extended G_{M1} headgroups or from local condensation within the membrane. A method of determining whether certain receptors prefer condensed lipid environments is to use fluorescence microscopy to assess the partitioning behavior of their labeled conjugates into microscopic L_o/L_d phases (17–19) or through detection of changes in the emission spectra of the dye depending on its localization in either the L_o or

L_d phase (20, 21). In such experiments, however, it is not easily possible to distinguish whether the fluorescence intensity of the labeled conjugate was emitted from the inner or outer membrane leaflet.

Another common technique to indirectly study the structure of lipid bilayers is to assess the lateral motion of the dye molecules in a SLB using fluorescence recovery after photobleaching (FRAP) (12), continuous bleaching (22) or fluorescence correlation spectroscopy (FCS). With these measurements, lipid diffusion in the bilayer is quantified, providing information about the bilayer fluidity and whether the SLB is in a condensed or fluid state. Recent FCS studies in model lipid raft SLBs on mica show that lipid diffusion is more than tenfold slower in L_o domains compared to L_d domains (14), suggesting that lipid rafts are condensed entities (3). Membrane receptors have also been shown to influence lipid mobility: FRAP studies on SLBs with G_{M1} symmetrically distributed among the leaflets demonstrate that G_{M1} decreases the mobility of surrounding lipids (23), particularly if the surrounding lipids are near a gel phase transition (24). Possible mechanisms of lipid fluidity moderation by G_{M1} are lateral condensation of lipid molecules (25) or local lipid immobilization due to a disruption of lipid headgroup packing, as reported for lipid monolayer systems (26). Such lateral structures within the membrane may act as obstacles and hinder the diffusion of lipids (27, 28). A direct method to examine lipid bilayer structure is X-ray surface diffraction; in principle, the sensitivity of X-rays to the electron density distribution within SLBs should allow distinction between the different condensation states of a lipid bilayer. X-ray reflectivity at solid-liquid interfaces has been used to study the structure of SLBs with subnanometer resolution (29–31) and there has been progress towards understanding single bilayer heterogeneity using this technique (32). Highly brilliant X-rays, provided by modern synchrotron sources, can give access to detailed depth profiles of lipid bilayers with an accuracy of several Ångstrøm, allowing for an identification of distinct components in separate lipid leaflets.

In this work, we directly measure how the receptor G_{M1} and model lipid rafts impact the structure of model lipid bilayers. We characterize single SLBs at the solid-liquid interface with X-ray reflectivity using a microfluidic sample chamber described in previous work (29, 30, 33). First, a one-component SLB in the fluid phase is characterized and lipid packing modifications after asymmetric insertion of G_{M1} are analyzed. Then, the structural characteristics of single phase SLBs representing either condensed or non-condensed bilayers are identified; we estimate the lipid compositions based on the corresponding 100% L_o and 100% L_d phases in the phase diagram of giant unilamellar vesicles of ternary mixtures of cholesterol/sphingomyelin/1,2-dioleoyl-*sn*-glycero-3-phosphocholine (34, 35). Finally, a series of SLBs from ternary mixtures capable of liquid-liquid phase separation are investigated and the structural modifications of these SLBs upon asymmetric G_{M1} insertion are analyzed in terms of condensation and stretching. These structural X-ray studies are complemented by fluorescence microscopy and continuous bleaching on the same samples. We also investigate lipid dynamics by measuring lipid diffusion before and after incorporation of G_{M1} into the bilayers.

Materials and Methods

Chemicals

The lipids 1-stearoyl-2-oleoyl-*sn*-glycero-3-phosphocholine (SOPC), 1,2-dioleoyl-*sn*-glycero-3-phosphocholine (DOPC), brain sphingomyelin (bSM), cholesterol and the ovine brain ganglioside G_{M1} are purchased from Avanti Polar Lipids (Alabaster, AL). Cholera toxin subunit B, labeled with Alexa Fluor 488 (Alexa488-CTB), and Texas Red labeled 1,2-dihexadecanoyl-*sn*-glycero-3-phosphoethanolamine, triethylammonium salt (TR-DPPE) are purchased from Invitrogen (Karlsruhe, Germany). HPLC-grade chloroform, acetone, isopropanol and ethanol are obtained from Carl Roth (Karlsruhe, Germany). Reagent-grade NH_4OH, HCl (37%) and H_2O_2 are purchased from Sigma (St. Louis, MO). NaCl, $CaCl_2$, $MgCl_2$, phosphate buffered saline (PBS) and HEPES are also from Sigma. Buffer I is composed of 10 mM HEPES, 100 mM NaCl, 2 mM $CaCl_2$, 2 mM $MgCl_2$ at pH$= 7.4$ and buffer II is composed of 138 mM NaCl, 2.7 mM KCl, 10 mM Na_2HPO_4, 2 mM KH_2PO_4 at pH$= 7.4$ (0.01 M PBS). Buffers are prepared in de-ionized (DI) water from Millipore Corp. (Billerica, MA).

Substrate treatment

Polished 6" silicon wafers with a 100 nm thermal oxide layer are cut into small pieces of size 20×15 mm^2 (Crystec GmbH, Berlin, Germany). Before experiments, the substrates are cleaned by sonication in isopropanol for 10 min followed by rinsing with DI water. Afterwards, a three-stage chemical cleaning treatment is applied: first, the substrates are boiled in acetone for 10 min, then in 1/1/5 H_2O_2/HCl/H_2O by volume for 15 min at 150°C, then in 1/1/5 H_2O_2/NH_4OH/H_2O for another 15 min at 150°C. After each step, the substrates are rinsed thoroughly with DI water. The substrates are stored in DI water until further use.

Sample chamber assembly

Plastic sample chambers (μ-Slide I) are purchased from ibidi GmbH (München, Germany) and are modified to embed the silicon wafer pieces (30). The clean SiO_2 substrates are affixed to the base of the chamber. The substrates are dried with a nitrogen stream and immediately glued into the chambers using two-component epoxy glue that hardens in 5 min (UHU, Bühl, Germany). After allowing the epoxy glue to dry for 30 min, the chambers with glued-in substrates are placed under vacuum for 6 h for final hardening. The microfluidic channel inside the sample chamber is then filled with buffer I.

Preparation of large unilamellar vesicles

All lipid mixtures are prepared in HPLC-grade chloroform in clean glass vials, except for TR-DPPE, which is prepared in a 1:1 mixture by volume of chloroform and methanol. The chloroform is first evaporated from each vial in a nitrogen stream followed by 8 h evacuation in a vacuum chamber to completely remove the solvent. The dry lipid film in the vials is suspended in buffer I at a final concentration of 1 mg/mL and heated to 50°C for 1 h. The extrusion method (36) is

used to prepare large unilamellar vesicles (LUVs) for experiments. The lipid suspension is vortexed and then passed 11 times through a polycarbonate filter with uniform 100 nm pores (Avanti Polar Lipids). For compositions of cholesterol/DOPC/bSM, lipids are extruded at a temperature above the lipid phase transition temperature, T_{m}, using the lipid phase diagram of giant unilamellar vesicles (GUVs) for these lipid compositions as a reference to determine T_{m} (37).

Vesicle fusion via osmotic rupture

The LUVs are used to form SLBs on the freshly prepared substrates in the sample chambers via vesicle fusion (38): the LUVs are injected into chambers pre-wetted with buffer I and incubated for 3 h, allowing for the LUVs to adhere on the substrate. The temperature of the LUVs is kept above T_{m} during incubation. The chamber is then flushed with DI water at room temperature to assist the rupture of the LUVs due to osmotic stress, forming a continuous lipid bilayer on the substrate. The surface area coverage is complete as verified by fluorescence microscopy. After formation of the continuous supported bilayer, the samples are kept above T_{m} for another 4 h and then slowly cooled down to room temperature. The samples are flushed several times with buffer II before the measurements.

G_{M1} incorporation into SLBs

Buffer II is added to G_{M1} in powder form at a concentration of 1 mg/mL and the solution is stored at 4°C. G_{M1} in such aqueous solutions can aggregate and form micelles (39) and this G_{M1} concentration of 640 μM is well above the critical micelle concentration (CMC) of 3.32 μM (40). Sample chambers with SLB-coated substrates are rinsed with buffer II, then filled with 100 μL of the G_{M1} solution and left to incubate for 4 h. G_{M1} can spontaneously partition into the outer leaflet of lipid bilayers up to concentrations of 30 % (41) due to its amphiphilic character, as previously reported (42, 43).

X-ray reflectivity measurements

The samples are prepared and measured at the undulator beamline ID01 at the European Synchrotron Radiation Facility (ESRF) in Grenoble, France. For X-ray reflectivity, the sample chamber and beamline setup described in Ref. (30) is used; a schematic is shown in Fig. 1. The X-ray energy is 19.5 keV ($\lambda = 0.623$ Å) and sample chambers are mounted in horizontal scattering geometry. The incidental beam cross section is 20×200 μm^2 (vertical $\times$ horizontal). A small vertical post-sample aperture suppresses reflectivity from the thin top foil of the sample chamber. Air scattering is minimized by evacuated beam guides with Kapton windows positioned close to the sample chamber. The intensity is collected with a NaI detector. All reflectivity data are measured at room temperature and for each sample at least three different spots on the sample are recorded. Each spot is first characterized before reflectivity by fluorescence microscopy to verify complete surface coverage and homogeneity across the cross section area of the X-ray beam. Repeated reflectivity measurements on previously illuminated spots are avoided. In most cases, no variation is observed among the different spots. The presented reflectivity data are corrected for background,

sample illumination (footprint) and normalized to the Fresnel reflectivity (R/R_F), where

$$R_F = \left| \frac{1 - \sqrt{1 - (q_c/q_z)^2}}{1 + \sqrt{1 - (q_c/q_z)^2}} \right|^2 . \quad (1)$$

The momentum transfer normal to the interface is denoted as q_z and the momentum transfer at the critical angle of total reflection is q_c.
It should be noted that X-ray reflectivity laterally averages the electron density within the illuminated surface area. Thus these measurements do not distinguish between discrete and laterally segregated microscopic phases. This is governed by the experimental configuration where the X-ray beam impinges on the surface with typical grazing angles between 0.02° and 1.5° and therefore illuminates a large surface area of up to 2 mm $\times$ 0.2 mm.

X-ray data evaluation

A slab model is employed to evaluate the reflectivity data using the exact dynamical theory of Parratt (44). The slab model is smeared with an uniform overall roughness of 3 Å (45). Data fitting is performed by least-squares optimization and the electron densities and thicknesses of the slabs are varied independently for χ^2 minimization. The resulting profile represents the SLB structure normal to the surface. The spatial resolution is estimated as $L = \pi/q_{\text{max}} \sim 6$ Å, based on the dynamic range of the reflectivity data which extend up to $q_{\text{max}} = 0.5 - 0.6$ Å^{-1} (46).
Many of the the SLBs measured in this work have mixed components, such as cholesterol, which can be partially nested between lipid headgroups or lipids with acyl chains of different length. Thus, individual slabs of defined thickness and electron density represent the superposition of different molecular components and a subsequent analysis is employed to decompose different contributions. For a detailed analysis see Fig. 3 and the corresponding explanations in the Results section.

Fluorescence microscopy

Fluorescence microscopy is performed on-site at the ESRF using a transportable Axiotech Vario microscope from Carl Zeiss (Oberkochen, Germany), equipped with $10\times$ (NA 0.3) and long distance $63\times$ (NA 0.75) Plan-Neofluar objectives. Images are captured with an ORCA C4742-95 12NR CCD camera and WASABI imaging software from Hamamatsu Photonics (Tutzing, Germany). Lateral diffusion coefficients of the supported lipid bilayers are determined using continuous bleaching (22); the experimental technique and the procedure for data evaluation is described elsewhere in detail (29, 33). For these experiments, a mercury lamp is aligned to ensure homogeneous illumination of the sample. Continuous bleaching data are analyzed using MATLAB software from Mathworks (Cambridge, MA).

Results and Discussion

Structural impact of G_{M1} insertion into single component SLBs

The simplest model for the cell membrane is a single lipid bilayer of only one lipid component. The fluid SOPC bilayer ($T_m = 6°$C) provides a well-defined interface for understanding the structural influence of G_{M1} on lipid bilayers. Fig. 2*a* shows the reflectivity of a lipid bilayer of 99.5 mol % SOPC and the fluorescent probe 0.5 mol % TR-DPPE; the data curve is characteristic for a single lipid bilayer above a solid support (30, 31). After incubation for 4 h with excess G_{M1}, we again measure the reflectivity and small but significant changes in the reflectivity are apparent as seen in the normalized scan presented in Fig. 2*b*. The most prominent effect of G_{M1} incorporation into the membrane is a downward shift in the positions of the minima, from $q_z \sim 0.2$ to 0.18 Å^{-1} and from 0.34 to 0.3 Å^{-1}, qualitatively indicating a thickening of the bilayer.

We use the slab model to analyze the reflectivity. In our model for the SOPC bilayer without G_{M1}, each leaflet has 2 slabs representing the headgroups and 1 slab for the acyl chains and the region where the proximal and distal acyl chains meet is an additional slab; thus the whole bilayer comprises 7 slabs. To fit the SOPC layer after G_{M1} insertion, we add 1 slab to the distal headgroups to account for the large oligosaccharide headgroup of G_{M1} and use an 8 slab model. The electron density profiles extracted from fitting the slab model are presented as red curves in Fig. 3, *a* and *b*. The individual slabs are indicated by dashed lines. The green curves represent the subsequent decomposition of the profiles into sigmoidal error functions with a Gaussian roughness of 3 Å. Slabs of thickness > 6 Å are directly converted into symmetric Gaussians, whereas neighboring slabs < 6 Å are pooled together and represented as asymmetric sigmoidal functions. This parametrization indicates the location of the headgroup region, the acyl chains, and the region where the proximal and distal acyl chains meet. The parameters for the SOPC and SOPC/G_{M1} bilayers as determined following this procedure are listed in Table 1.

It is well established that water can penetrate into the lipid headgroups (47), which may complicate an exact definition of bilayer thickness based on X-ray data. However, we estimate this value from the sigmoidal peak corresponding to the distal headgroup, where we define the half-maximum position at the outermost slope as bilayer thickness, as shown in Fig. 3. Using this analysis, the SOPC bilayer has an overall thickness of 48 Å and appears highly symmetric. The thicknesses of the proximal and distal leaflets (headgroups and acyl chains) are 23 Å and 25 Å, respectively, and both headgroups are 10 Å. Upon insertion of G_{M1}, however, the bilayer structure becomes asymmetric and is significantly thickened (59 Å). The thickening effect is marginal in the proximal leaflet (26 Å), whereas the effect is primarily in the distal leaflet (33 Å). This increase in thickness of the distal leaflet originates mainly from the headgroup region, where a significant increase in electron density is observed upon G_{M1} insertion.

By comparing the thicknesses of the distal leaflet before (25 Å) and after (33 Å) G_{M1} insertion, we find that the G_{M1} headgroup protrudes a distance of 8 Å above the bilayer surface. Protrusion of the G_{M1} above the bilayer has been observed previously both with AFM (25) and X-ray diffraction (48), where it was shown that G_{M1} protrudes up to 12 Å above the surface of membranes in osmotically stretched stacked multibilayers. In the latter work, a full extension of the G_{M1} headgroup from the bilayer is reported, based on a comparison of the relative dimensions of G_{M1} and phosphatidylcholine headgroups. Assuming that G_{M1} headgroups in their fully extended conformation normal to the bilayer surface are 12 Å in height (48), our protrusion length of 8 Å (with experi-

mental uncertainty of ~ 2 Å) corresponds to an average headgroup tilt of $48 \pm 12^{\circ}$ with respect to the bilayer normal. Mismatch of acyl chains between G_{M1} and SOPC could also contribute to the thickening of the distal leaflet, however, this effect should be minimal as the ceramide chains of ovine G_{M1} (acyl chain abundance: 18:0-18:1, 70%; 20:1-18:0, 30 %) almost match the chains of SOPC (acyl chain abundance: 18:0-18:1).

The similarity of the profiles from Fig. 3 of SOPC and SOPC/G_{M1} in the proximal leaflet region of the SLB, contrasting the headgroup repositioning and density change in the distal leaflet, show that G_{M1} insertion only negligibly modifies the electron density profile of the proximal leaflet. This result suggests that G_{M1} inserts only into the distal leaflet of these supported membranes and does not flip into the bottom leaflet. By repeating our measurement of the reflectivity of the SOPC/G_{M1} membranes after 3 days, we verify that G_{M1} remains in the distal leaflet, as the reflectivity does not change over this time scale.

The electron density profiles show that the headgroups are in close proximity to the substrate, implying that no distinct water layer is present separating the membrane from the substrate. Or, if a lubricating water layer is present, its dimension is below our resolvable lengthscale. We propose that only few water molecules bound to the proximal headgroups are present, rather than a lubricating water layer of defined thickness.

We also investigate whether there are structural modifications in G_{M1} enriched lipid bilayers upon binding of cholera toxin. Cholera toxin can bind five G_{M1} receptors with its B subunit (CTB) and the resulting complex becomes the entry point for cholera toxin to enter the cell (8). Binding of Alexa488-CTB to the membrane is evidenced by fluorescence microscopy, as the membrane surface after incubation with Alexa488-CTB shows bright homogeneous fluorescence. We verify with fluorescence microscopy that there is no non-specific binding of Alexa488-CTB to SOPC bilayers lacking G_{M1} in a control experiment (data not shown). We find that the reflectivity of a SOPC/G_{M1} bilayer is unchanged after incubation with Alexa488-CTB (Fig. 4). We do not detect a modification of the lipid bilayer structure upon Alexa488-CTB binding, in contrast to previous reports of lipid monolayer systems (26). In general, lipid bilayers are more stable than monolayers and can resist collapse upon binding of large molecules to the membrane surface (29). We are also unable to resolve the formation of a Alexa488-CTB layer above the bilayer surface with reflectivity. CTB lacks the large subunit A of cholera toxin and it has a relatively hollow ring structure which can be easily penetrated by water (49–51). It is likely that a water-filled CTB layer on the membrane does not provide enough electron density contrast with respect to the excess water above the membrane.

Characterization of condensed (liquid-ordered) and non-condensed (liquid-disordered) SLBs

We next characterize the more complex system of lipid bilayers with multiple components capable of phase separation. Mixtures of cholesterol/DOPC/bSM can phase separate into liquid-disordered (L_d) and liquid-ordered (L_o) phases, modeling lipid rafts in cell membranes (20). This phase separation is readily observed with fluorescence microscopy in fluid lipid bilayer vesicles (20, 34). We choose lipid compositions corresponding to 100% L_d and 100% L_o phases in the lipid phase diagram established for giant unilamellar vesicles (GUVs) of cholesterol, DOPC, and sphingomyelin (34). We estimate these mixtures based on a tie line approximated from the similar GUV phase diagram of 1:1 DOPC/DPPC and 30 mol % cholesterol (35). According to our estimation, the fluid

L_d phase has an approximate composition of 15/65/20 (cholesterol/DOPC/bSM) and the L_o phase has an approximate composition of 29/6/65 (cholesterol/DOPC/bSM).
To elucidate structural differences between the L_d and L_o phase, we prepare separate SLBs with compositions of 15/65/19.5/0.5 (referred to as *LD*) and 29/6/64.5/0.5 (referred to as *LO*) mol % cholesterol/DOPC/bSM/TR-DPPE and measure them with reflectivity. The reflectivity data are shown in Fig. 5, the corresponding electron density profiles are plotted in Fig. 6, and the parameters extracted from fitting the data are summarized in Table 2. We show that the electron density profile of *LD* is similar to the profile of a fluid SOPC bilayer (compare Fig. 3*a* and Fig. 6*a*). In both of these SLBs, the acyl chain thicknesses in both leaflets are 14 Å and the electron density in the chain region is 0.28 $e^-/Å^3$. For the *LO* composition, the bilayer structure changes significantly and exhibits condensation. The *LO* bilayer is 10 Å thicker than the *LD* bilayer, as shown in Fig. 6*b*. Our measured height difference is consistent with AFM experiments, where a relative height difference between L_o and L_d phases of 8 Å has been measured on SLBs of molar composition 0.67:1:1 (cholesterol:DOPC:SM) (14). For the *LO* bilayer, we measure a higher electron density in the acyl chain regions of 0.33 $e^-/Å^3$, as compared to 0.28 $e^-/Å^3$ for the *LD* bilayer. In both cases, the distal headgroup regions appear broadened compared to the proximal headgroup regions, indicating that the membrane surface facing the water is not as smooth as the opposite surface facing the substrate. Here, the advantage of using X-ray reflectivity for structural characterization becomes clear because, in addition to height differences, we are able to resolve structural details along the full depth of the membrane.
Based on these results, we empirically define condensation of lipid bilayers in terms of the electron density and thickness of the acyl chains. In this scheme, both an electron density of 0.28 ± 0.01 $e^-/Å^3$ and chain thickness of 14 ± 1 Å are characteristic of a non-condensed bilayer leaflet, whereas an electron density of 0.33 ± 0.01 $e^-/Å^3$ and chain thickness of 17 ± 1 Å is representative of a condensed bilayer leaflet. This condensation effect is reflected in the corresponding sketches of the bilayer structure in Fig. 6, showing the *LO* bilayer as thickened with stretched and packed acyl chains as compared to the *LD* bilayer. The threshold values (non-condensed, condensed) for the electron density are graphically indicated as gray lines in Fig. 6.
We discuss the effect of cholesterol, which is present both in the *LD* and *LO* bilayers, by comparing the profiles of the *LD* bilayer (Fig. 6*a*) with the single component SOPC bilayer (Fig. 3*a*). In the *LD* bilayer, we find a higher electron density where the headgroups and acyl chains meet compared to the SOPC bilayer. This increase of electron density is also apparent in the *LO* profile (Fig. 6*b*). We can explain this effect by an accumulation of cholesterol below the lipid headgroups, which effectively contributes to the electron rich headgroup region. This nesting effect of cholesterol below headgroups is consistent with mechanisms proposed in modeling studies. Previous Monte Carlo simulations suggest that due to an unfavorable free energy of cholesterol in contact with water, nonpolar cholesterol is located underneath polar lipid headgroups in bilayers (52). It should be noted that the variety of lipid constituents with different chain length in natural brain sphingomyelin may additionally contribute to the measured broadening of the headgroups.

Model lipid raft SLBs and the asymmetric condensing effect of G_{M1}

After having separately characterized *LD* and *LO* bilayers, we now investigate SLBs with an equimolar lipid ratio of DOPC and bSM and varying amount of cholesterol. Three samples with SLBs of cholesterol/DOPC/bSM/TR-DPPE with molar percentages 20/40/39.5/0.5 (referred to as

20chol), 30/35/34.5/0.5 (*30chol*), 40/30/29.5/0.5 (*40chol*) are measured at room temperature. The compositions of these SLBs are capable of phase separation in fluid membranes according to the GUV phase diagram. The reflectivities are presented in Fig. 7*a* and the corresponding profiles are presented in Fig. 8*a*. Extracted parameters are listed in Table 3.

According to our definition of bilayer condensation from the *LO* and the *LD* bilayers, we are able to characterize the condensation state of these samples based exclusively on our X-ray analysis. In mixture *20chol*, we observe a high electron density of the acyl chains (0.33 $e^-/Å^3$) and a bilayer thickness of 58 Å, which shows strong structural similarity with the *LO* bilayer. This lipid composition is clearly in the L_o/L_d coexistence region of the GUV phase diagram at room temperature (37) and it is therefore possible that both L_o and L_d phases are present. By contrast, mixtures *30chol* and *40chol* show lower electron densities of the chain regions (0.30 and 0.29 $e^-/Å^3$, respectively). Although the electron density of the lipid chains is increased in the vicinity of the headgroups, possibly due to cholesterol accumulation, the overall chain density and bilayer thickness do not indicate a condensation and the bilayer structures of *30chol* and *40chol* are similar to the non-condensed *LD*-bilayer. In the GUV phase diagram, composition *30chol* is located at the onset of L_o/L_d coexistence at room temperature (37), and it is thus not necessarily expected that phase separation occurs in SLBs of the same composition. Composition *40chol* is clearly in the single phase region at room temperature in the GUV phase diagram (37).

We expect the effect of G_{M1} on membrane structure in lipid membranes of cholesterol, sphingomyelin and DOPC to be more complex than in homogeneous SLBs of only one component. The capability of G_{M1} to moderate lipid packing in cholesterol enriched lipid mixtures has been reported in previous studies (53, 54); moreover, an attractive electrostatic interaction between the sialic acid of G_{M1} and the positively-charged choline headgroups of DOPC and bSM has been observed in cholesterol/DOPC/bSM membranes containing G_{M1} (16). We use our protocol for G_{M1} incorporation into SLBs to assess the structural effect of asymmetric G_{M1} on the samples *20chol*, *30chol* and *40chol*. After G_{M1} insertion, these samples are subsequently referred to as *20chol*+G_{M1}, *30chol*+G_{M1} and *40chol*+G_{M1}. The reflectivity data from these samples are presented in Fig. 7*b* and the electron density profiles are plotted in Fig. 8*b*. Interestingly, the electron density profile of *20chol*+G_{M1} shows only minimal changes; namely, a slight increase in bilayer thickness of 3 Å due to a broader distal headgroup. More dramatic structural effects are observed for samples *30chol*+G_{M1} and *40chol*+G_{M1}, which were not condensed before G_{M1} insertion. Here, the electron density profiles show a thickening of the SLBs about 9 and 8 Å, respectively, and an increase in density of the distal headgroups from 0.41 to 0.48 $e^-/Å^3$ and from 0.40 to 0.49 $e^-/Å^3$, respectively. A condensation in the acyl chain region is only observed in the distal leaflet, indicated by an increase in thickness from 14 to 18 Å for *30chol*+G_{M1} and from 14 to 17 Å for *40chol*+G_{M1} and an increase in electron density from 0.30 to 0.33 $e^-/Å^3$ for *30chol*+G_{M1} and from 0.29 to 0.33 $e^-/Å^3$ for *40chol*+G_{M1}. As we observed in the measurements of the SOPC-bilayer, the proximal acyl chains remain relatively unaffected, although the electron density slightly increases from 0.30 to 0.31 $e^-/Å^3$ for *30chol*+G_{M1} and from 0.29 to 0.30 $e^-/Å^3$ for *40chol*+G_{M1}.

X-ray reflectivity allows us to confirm the expectation that G_{M1} modifies the structure of cholesterol-enriched SLBs and to precisely quantify these structural changes. Our results indicate that all three investigated lipid mixtures containing cholesterol, DOPC and bSM are in a condensed state after G_{M1} incorporation. With the exception of *20chol*+G_{M1}, which already showed condensation without G_{M1}, the condensation we observe in samples *30chol*+G_{M1} and *40chol*+G_{M1} is asymmetric, indicating that the structural effect of G_{M1} is restricted to the distal leaflet where it is exclusively

present.

Lipid diffusion and fluorescence microscopy

In addition to X-ray reflectivity, we image the SLBs with fluorescence microscopy to characterize microscopic features in the membranes and to measure the lateral lipid diffusion in the bilayers. The compact sample chambers that we use allow for fluorescence microscopy imaging on the same SLBs measured with X-ray reflectivity (30). Before incubation with G_{M1}, all of the SLBs have homogeneous fluorescence and we do not observe microscopic phase separation on the samples *20chol*, *30chol* and *40chol*. An example fluorescence micrograph of *20chol* is shown in Fig. 9*a*. Although this lipid mixture is known to separate into microscopic L_o and L_d phases at room temperature in GUVs, as visualized by partitioning of the dye into the L_d phase (37), our sample shows a uniform fluorescence. Whereas L_o/L_d coexistence in SLBs with sub-micron domains are reported by AFM studies on mica (14, 16, 55), surfaces with defined topography (56) and glass slides (57), we do not observe microscopic phases on the SiO_2 substrates (surface roughness 3 Å) that we use for reflectivity. It is possible that our model lipid raft mixtures have nanoscopic domains that do not grow to microscopic size in the vicinity of the solid interfaces (19).

However, we do observe microscopic features upon incorporation of G_{M1} into SLBs containing cholesterol, DOPC and sphingomyelin (samples *20chol+G_{M1}*, *30chol+G_{M1}* and *40chol+G_{M1}*). Dark spots ~ 3 μm in diameter appear which exclude TR-DPPE that are not present before G_{M1} incubation. Fig. 9*b* shows a micrograph of sample *20chol+G_{M1}*. The dark spots are also observed on the samples *30chol+G_{M1}* and *40chol+G_{M1}* (data not shown). In sample *20chol+G_{M1}*, we see gray spots (~ 3 μm) on the membrane surface in coexistence with the dark spots (Fig. 9*b*). To elucidate whether the spots are lipid domains or surface defects, we examine the temperature behavior of the SLBs. The dark spots persist upon heating and do not change in shape or size up to a temperature of 70°C (Fig. 9*c*). Qualitative reference to the GUV phase diagram show that our lipid mixtures do not exhibit lipid phase coexistence above 50°C (37). Thus, the stability of the dark spots, combined with their strong exclusion of the dye, suggest that they are micron-sized membrane defects such as pinned G_{M1} clusters or bare surface areas. Previous experiments show that membrane rupture and hole formation can be induced by increasing the tension in the membrane (38); attractive interactions of G_{M1} with adjacent lipids could also accommodate the local packing of lipids and promote the formation of pinholes in the membrane. Interestingly, the gray spots in sample *20chol+G_{M1}* disappear upon heating to 40°C and reappear upon cooling in the same positions (Fig. 9*d*). The gray spots thus may represent lateral lipid domains that exclude the fluorescent dye. Previous studies have demonstrated that lipid domains in SLBs lack the reversible phase behavior characteristic of fluid membranes and the domains can be pinned to the substrate (19, 58). The size of the gray spots is comparable to the size of the L_o phases recently reported by AFM measurements on SLBs of molar composition 0.67:1:1 (cholesterol:DOPC/bSM) (14), suggesting that microscopic L_o phases can form in the presence of the silicon oxide interface upon G_{M1} insertion.

To quantitatively assess if G_{M1} modifies the fluidity of the bilayer, we measure the lateral diffusion coefficients of TR-DPPE in the samples *20chol*, *30chol* and *40chol*, before and after insertion of G_{M1} using continuous bleaching. The continuous bleaching method allows diffusion constants to be measured with a standard fluorescent microscopy setup and does not require laser bleaching (22). The diffusion coefficients we measure with continuous bleaching represent the laterally aver-

aged lipid diffusion in a circular spot 180 μm diameter and it is therefore not possible to distinguish between separate diffusion coefficients in coexisting phases. Recent work using two-focus scanning fluorescence correlation spectroscopy reports separate diffusion constants of 3.5 ± 0.3 μm^2/s for the L_d phase and 0.1 ± 0.02 μm^2/s for the L_o phase in a SLB with 0.67:1:1 molar composition of cholesterol:DOPC:SM (14). We measure diffusion coefficients for samples *20chol*, *30chol* and *40chol* of (0.45 ± 0.03, 0.22 ± 0.01 and 0.12 ± 0.01) μm^2/s, respectively. Our diffusion data shows the general trend that diffusion is reduced as the concentration of cholesterol is increased. Our coefficients are between the two values reported for the L_d and L_o phase and it is possible that they represent averaged values of coexisting phases. After these samples are incubated with excess G_{M1}, we measure diffusion constants of (0.10 ± 0.02, 0.09 ± 0.01 and 0.03 ± 0.01) μm^2/s for samples *20chol+G_{M1}*, *30chol+G_{M1}* and *40chol+G_{M1}*, respectively. Thus, the addition of G_{M1} to the bilayer reduces the lipid fluidity by more than 50%. These results confirm that condensation of SLBs is accompanied by a reduced lipid diffusion. The reduction in the mobility of single component membranes after the addition of G_{M1} is well-established (23, 24, 59). In heterogeneous membranes, where G_{M1} can influence lipid phase separation (24, 53), lipid diffusion is more complicated. The condensing effect of G_{M1} can promote the formation of L_o domains and ordered lipid domains can also reduce the fluidity of the surrounding lipid bilayer as a function of area coverage by creating obstacles for lipid movement (60).

Conclusion

Structural studies of single SLBs with Ångstrøm resolution allow the effect of individual molecules on the condensation state of the SLB to be quantified. The incorporation of the membrane receptor G_{M1} into SLBs stretches the outer membrane leaflet and increases the lipid headgroup density, consistent with a structural effect of the G_{M1} headgroup protruding out from the membrane surface. We observe this effect in homogeneous SLBs of SOPC, where the asymmetry among both leaflets after insertion of G_{M1} can be resolved. With X-ray reflectivity, we are clearly able to distinguish condensed and fluid SLBs and determine how the individual regions of the SLB (headgroups, acyl chains) are affected by condensation. Our measurements also suggest the position of cholesterol within the bilayer as the electron density is increased in the region where headgroups and acyl chains meet, which is consistent with cholesterol nesting below the headgroups. Asymmetric inclusion of G_{M1} has a condensing effect on cholesterol-enriched membranes and this effect is restricted to the leaflet where G_{M1} is present. The condensing effect of G_{M1} is also evidenced by a reduced lipid diffusion of cholesterol-enriched membranes and we observe microscopic lipid domains introduced in the presence G_{M1}. Understanding the organization of molecules within biological membranes requires techniques that probe the structure of individual leaflets. Such high resolution can be obtained with X-ray reflectivity at solid-liquid interfaces and this technique may be applied to other complex membrane systems.

Acknowledgments

We acknowledge the European Synchrotron Radiation Facility for provision of synchrotron radiation facilities and we thank Till H. Metzger for assistance in using the beamline ID01 and

Harald Müller for assistance in the chemistry laboratory. We are grateful to Martin Huth for help with the synchrotron measurements. We thank the Alexander von Humboldt Foundation and the MIT Germany Program for travel funds. This work was funded in part through the Robert T. Haslam Chair at MIT and the German Federal Ministry of Education and Research (BMBF grant no. 03RA6LMU).

References

1. Janmey, P., and P. Kinnunen, 2006. Biophysical properties of lipids and dynamic membranes. *Trends Cell Biol.* 16:538–546.

2. Simons, K., and E. Ikonen, 1997. Functional rafts in cell membranes. *Nature* 387:569–572.

3. Brown, D. A., and E. London, 2000. Structure and Function of Sphingolipid- and Cholesterol-rich Membrane Rafts. *J. Biol. Chem.* 275:17221–17224.

4. Anderson, R. G. W., and K. Jacobson, 2002. A Role for Lipid Shells in Targeting Proteins to Caveolae, Rafts, and Other Lipid Domains. *Science* 296:1821–1825.

5. Simons, K., and E. Ikonen, 2000. How Cells Handle Cholesterol. *Science* 290:1721–1726.

6. Maxfield, F. R., and I. Tabas, 2005. Role of cholesterol and lipid organization in disease. *Nature* 438:612–621.

7. Sprong, H., P. van der Sluijs, and G. van Meer, 2001. How proteins move lipids and lipids move proteins. *Nat. Rev. Mol. Cell Biol.* 2:504–513.

8. Lencer, W. I., T. R. Hirst, and R. K. Holmes, 1999. Membrane traffic and the cellular uptake of cholera toxin. *Biochim. Biophys. Acta (BBA) - Molecular Cell Research* 1450:177–190.

9. Richter, R., and A. Brisson, 2003. Characterization of Lipid Bilayers and Protein Assemblies Supported on Rough Surfaces by Atomic Force Microscopy. *Langmuir* 19:1632–1640.

10. Salditt, T., 2005. Thermal fluctuations and stability of solid-supported lipid membranes. *J. Phys.: Condens. Matter* 17:R287–R314.

11. Braun, D., and P. Fromherz, 1998. Fluorescence Interferometry of Neuronal Cell Adhesion on Microstructured Silicon. *Phys. Rev. Lett.* 81:5241.

12. Axelrod, D., D. E. Koppel, J. Schlessinger, E. Elson, and W. W. Webb, 1976. Mobility Measurement by Analysis of Fluorescence Photobleaching Recovery Kinetics. *Biophys. J.* 16:1055.

13. Rädler, J., and E. Sackmann, 1993. Imaging optical thicknesses and separation distances of phospholipid vesicles at solid surfaces. *J. Phys. II France* 3:727–748.

14. Chiantia, S., J. Ries, N. Kahya, and P. Schwille, 2006. Combined AFM and Two-Focus SFCS Study of Raft-Exhibiting Model Membranes. *ChemPhysChem* 7:2409–2418.

15. Chiantia, S., N. Kahya, J. Ries, and P. Schwille, 2006. Effects of Ceramide on Liquid-Ordered Domains Investigated by Simultaneous AFM and FCS. *Biophys. J.* 90:4500–4508.

16. Yuan, C., J. Furlong, P. Burgos, and L. J. Johnston, 2002. The Size of Lipid Rafts: An Atomic Force Microscopy Study of Ganglioside GM1 Domains in Sphingomyelin/DOPC/Cholesterol Membranes. *Biophys. J.* 82:2526–2535.

17. Samsonov, A. V., I. Mihalyov, and F. S. Cohen, 2001. Characterization of Cholesterol-Sphingomyelin Domains and Their Dynamics in Bilayer Membranes. *Biophys. J.* 81:1486–1500.

18. Crane, J., V. Kiessling, and L. Tamm, 2005. Measuring Lipid Asymmetry in Planar Supported Bilayers by Fluorescence Interference Contrast Microscopy. *Langmuir* 21:1377–1388.

19. Garg, S., J. Ruhe, K. Ludtke, R. Jordan, and C. A. Naumann, 2007. Domain Registration in Raft-Mimicking Lipid Mixtures Studied Using Polymer-Tethered Lipid Bilayers. *Biophys. J.* 92:1263–1270.

20. Dietrich, C., L. A. Bagatolli, Z. N. Volovyk, N. L. Thompson, M. Levi, K. Jacobson, and E. Gratton, 2001. Lipid Rafts Reconstituted in Model Membranes. *Biophys. J.* 80:1417–1428.

21. Bagatolli, L. A., 2006. To see or not to see: Lateral organization of biological membranes and fluorescence microscopy. *Biochim. Biophys. Acta (BBA) - Biomembranes* 1758:1541–1556.

22. Dietrich, C., R. Merkel, and R. Tampe, 1997. Diffusion Measurement of Fluorescence-Labeled Amphiphilic Molecules with a Standard Fluorescence Microscope. *Biophys. J.* 72:1701–1710.

23. Weng, K. C., J. L. Kanter, W. H. Robinson, and C. W. Frank, 2006. Fluid supported lipid bilayers containing monosialoganglioside GM1: A QCM-D and FRAP study. *Colloids Surf. B. Biointerfaces* 50:76–84.

24. Yamazaki, V., O. Sirenko, R. Schafer, and J. Groves, 2005. Lipid Mobility and Molecular Binding in Fluid Lipid Membranes. *J. Am. Chem. Soc.* 127:2826–2827.

25. Yuan, C., and L. J. Johnston, 2001. Atomic Force Microscopy Studies of Ganglioside GM1 Domains in Phosphatidylcholine and Phosphatidylcholine/Cholesterol Bilayers. *Biophys. J.* 81:1059–1069.

26. Miller, C. E., J. Majewski, R. Faller, S. Satija, and T. L. Kuhl, 2004. Cholera Toxin Assault on Lipid Monolayers Containing Ganglioside GM1. *Biophys. J.* 86:3700–3708.

27. Almeida, P. F. F., W. L. C. Vaz, and T. E. Thompson, 1992. Lateral Diffusion and Percolation in Two-Phase, Two-Component Lipid Bilayers. Topology of the Solid-Phase Domains In-Plane and Across the Lipid Bilayer. *Biochemistry* 31:7198–7210.

28. Zhang, L., and S. Granick, 2005. Slaved diffusion in phospholipid bilayers. *Proc. Natl. Acad. Sci. USA* 102:9118–9121.

29. Horton, M. R., C. Reich, A. P. Gast, J. O. Rädler, and B. Nickel, 2007. Structure and Dynamics of Crystalline Protein Layers Bound to Supported Lipid Bilayers. *Langmuir* 23:6263–6269.

30. Reich, C., M. B. Hochrein, B. Krause, and B. Nickel, 2005. A microfluidic setup for studies of solid-liquid interfaces using x-ray reflectivity and fluorescence microscopy. *Rev. Sci. Instrum.* 76:095103.

31. Miller, C. E., J. Majewski, T. Gog, and T. L. Kuhl, 2005. Characterization of Biological Thin Films at the Solid-Liquid Interface by X-Ray Reflectivity. *Phys. Rev. Lett.* 94:238104.

32. Nováková, E., K. Giewekemeyer, and T. Salditt, 2006. Structure of two-component lipid membranes on solid support: An x-ray reflectivity study. *Phys. Rev. E* 74:051911.

33. Hochrein, M. B., C. Reich, B. Krause, J. O. Rädler, and B. Nickel, 2006. Structure and Mobility of Lipid Membranes on a Thermoplastic Substrate. *Langmuir* 22:538–545.

34. Veatch, S. L., and S. L. Keller, 2005. Miscibility phase diagrams of giant vesicles containing sphingomyelin. *Phys. Rev. Lett.* 94:148101.

35. Veatch, S. L., I. V. Polozov, K. Gawrisch, and S. L. Keller, 2004. Liquid Domains in Vesicles Investigated by NMR and Fluorescence Microscopy. *Biophys. J.* 86:2910–2922.

36. MacDonald, R. C., R. I. MacDonald, B. P. M. Menco, K. Takeshita, N. K. Subbarao, and L. Hu, 1991. Small-volume extrusion apparatus for preparation of large, unilamellar vesicles. *Biochim. Biophys. Acta (BBA) - Biomembranes* 1061:297–303.

37. Horton, M. R., J. Rädler, and A. P. Gast, 2006. Phase behavior and the partitioning of caveolin-1 scaffolding domain peptides in model lipid bilayers. *J. Colloid Interface Sci.* 304:67–76.

38. Tamm, L. K., and H. M. McConnell, 1985. Supported phospholipid bilayers. *Biophys. J.* 47:105–113.

39. Cantú, L., M. Corti, E. Del Favero, E. Muller, A. Raudino, and S. Sonnino, 1999. Thermal Hysteresis in Ganglioside Micelles Investigated by Differential Scanning Calorimetry and Light-Scattering. *Langmuir* 15:4975–4980.

40. Basu, A., and R. H. Glew, 1985. Characterization of the activation of rat liver beta-glucosidase by sialosylgangliotetraosylceramide. *J. Biol. Chem.* 260:13067–13073.

41. Bach, D., I. R. Miller, and B.-A. Sela, 1982. Calorimetric studies on various gangliosides and ganglioside-lipid interactions. *Biochim. Biophys. Acta (BBA) - Biomembranes* 686:233–239.

42. Spiegel, S., J. Schlessinger, and P. H. Fishman, 1984. Incorporation of fluorescent gangliosides into human fibroblasts: mobility, fate, and interaction with fibronectin. *J. Cell Biol.* 99:699–704.

43. Wang, R., J. Shi, A. N. Parikh, A. P. Shreve, L. Chen, and B. I. Swanson, 2004. Evidence for cholera aggregation on GM_1-decorated lipid bilayers. *Colloids Surf. B. Biointerfaces* 33:45–51.

44. Parratt, L. G., 1954. Surface Studies of Solids by Total Reflection of X-rays. *Phys. Rev.* 95:359.

45. Névot, L., and P. Croce, 1980. Characterization of surfaces by grazing x-ray reflection - Application to study of polishing of some silicate-glasses. *Revue de physique appliquée* 15:761.

46. Pershan, P. S., 1994. X-ray or neutron reflectivity: Limitations in the determination of interfacial profiles. *Phys. Rev. E* 50:2369–2372.

47. Wiener, M. C., G. I. King, and S. H. White, 1991. Structure of a fluid dioleoylphosphatidylcholine bilayer determined by joint refinement of x-ray and neutron diffraction data. I. Scaling of neutron data and the distributions of double bonds and water. *Biophys. J.* 60:568–576.

48. McIntosh, T. J., and S. A. Simon, 1994. Long- and Short-Range Interactions between Phospholipid/Ganglioside GM1 Bilayers. *Biochemistry* 33:10477–10486.

49. Zhang, R.-G., M. L. Westbrook, E. M. Westbrook, D. L. Scott, Z. Otwinowski, P. R. Maulik, R. A. Reed, and G. G. Shipley, 1995. The 2.4 A Crystal Structure of Cholera Toxin B Subunit Pentamer: Choleragenoid. *J. Mol. Biol.* 251:550–562.

50. Merritt, E. A., S. Sarfaty, F. V. D. Akker, C. L'Hoir, J. A. Martial, and W. G. Hol, 1994. Crystal structure of cholera toxin B-pentamer bound to receptor G(M1) pentasaccharide. *Protein Sci.* 3:166–175.

51. Ribi, H. O., D. S. Ludwig, K. L. Mercer, G. K. Schoolnik, and R. D. Kornberg, 1988. Three-dimensional structure of cholera toxin penetrating a lipid membrane. *Science* 239:1272–1276.

52. Huang, J., and G. W. Feigenson, 1999. A Microscopic Interaction Model of Maximum Solubility of Cholesterol in Lipid Bilayers. *Biophys. J.* 76:2142–2157.

53. Hammond, A. T., F. A. Heberle, T. Baumgart, D. Holowka, B. Baird, and G. W. Feigenson, 2005. Crosslinking a lipid raft component triggers liquid ordered-liquid disordered phase separation in model plasma membranes. *Proc. Natl. Acad. Sci. USA* 102:6320–6325.

54. Dietrich, C., Z. N. Volovyk, M. Levi, N. L. Thompson, and K. Jacobson, 2001. Partitioning of Thy-1, GM1, and cross-linked phospholipid analogs into lipid rafts reconstituted in supported model membrane monolayers. *Proc. Natl. Acad. Sci. USA* 98:10642–10647.

55. Lawrence, J. C., D. E. Saslowsky, J. M. Edwardson, and R. M. Henderson, 2003. Real-Time Analysis of the Effects of Cholesterol on Lipid Raft Behavior Using Atomic Force Microscopy. *Biophys. J.* 84:1827–1832.

56. Yoon, T.-Y., C. Jeong, S.-W. Lee, J. H. Kim, M. C. Choi, S.-J. Kim, M. W. Kim, and S.-D. Lee, 2006. Topographic control of lipid-raft reconstitution in model membranes. *Nature Materials* 5:281–285.

57. Seu, K. J., A. P. Pandey, F. Haque, E. A. Proctor, A. E. Ribbe, and J. S. Hovis, 2007. Effect of Surface Treatment on Diffusion and Domain Formation in Supported Lipid Bilayers. *Biophys. J.* 92:2445–2450.

58. Stottrup, B. L., S. L. Veatch, and S. L. Keller, 2004. Nonequilibrium Behavior in Supported Lipid Membranes Containing Cholesterol. *Biophys. J.* 86:2942–2950.

59. Goins, B., M. Masserini, B. G. Barisas, and E. Freire, 1986. Lateral diffusion of ganglioside GM1 in phospholipid bilayer membranes. *Biophys. J.* 49:849856.

60. Ratto, T. V., and M. L. Longo, 2002. Obstructed Diffusion in Phase-Separated Supported Lipid Bilayers: A Combined Atomic Force Microscopy and Fluorescence Recovery after Photobleaching Approach. *Biophys. J.* 83:3380–3392.

Sample	thickness of the bilayer [Å]	thickness proximal headgroup [Å]	thickness proximal acyl chains [Å]	thickness distal acyl chains [Å]	thickness distal headgroup [Å]	prox./dist. chain density [$e^-/Å^3$]	peak density of distal headgroup [$e^-/Å^3$]
SOPC	48	10	13	15	10	0.28/0.28	0.46
SOPC/G_{M1}	59	10	16	15	18	0.28/0.28	0.50

Table 1: Parameters extracted from analysis of the X-ray reflectivity data of SOPC and SOPC/G_{M1} SLBs.

Sample	thickness of the bilayer [Å]	thickness proximal headgroup [Å]	thickness proximal acyl chains [Å]	thickness distal acyl chains [Å]	thickness distal headgroup [Å]	prox./dist. chain density [$e^-/Å^3$]	peak density of distal headgroup [$e^-/Å^3$]
LD	54	11	14	14	15	0.28/0.28	0.44
LO	64	13	18	18	15	0.33/0.33	0.48

Table 2: Parameters extracted from analysis of the X-ray reflectivity data of the samples *LD* and *LO*.

Sample	thickness of the bilayer [Å]	thickness proximal headgroup [Å]	thickness proximal acyl chains [Å]	thickness distal acyl chains [Å]	thickness distal headgroup [Å]	prox./dist. chain density [$e^-/Å^3$]	peak density of distal headgroup [$e^-/Å^3$]
20chol	58	12	17	16	13	0.33/0.33	0.43
20chol+G_{M1}	61	12	16	16	17	0.33/0.33	0.43
30chol	56	12	13	14	17	0.30/0.30	0.41
30chol+G_{M1}	65	11	15	18	21	0.31/0.33	0.48
40chol	56	12	14	14	16	0.29/0.29	0.40
40chol+G_{M1}	64	11	14	17	22	0.30/0.33	0.49

Table 3: Parameters extracted from analysis of the X-ray reflectivity data of model lipid raft SLBs.

Figure Legends

Figure 1.

Schematic of the microfluidic sample chamber used for X-ray and fluorescence microscopy experiments.

Figure 2.

Normalized reflectivity scans with fits (*solid lines*) for SOPC before (*a*) and after (*b*) incubation with excess G_{M1}. Sketches illustrate the bilayer structure and asymmetric incorporation of G_{M1} into the distal leaflet.

Figure 3.

Decomposition of the electron density profiles (*red curves*) to determine the thicknesses of different bilayer regions. The slab model used for fitting the data is shown as a dotted line. The lipid headgroup region, alkyl chains and the space where the acyl chains meet are parameterized using sigmoidal functions (*green curves*). The excess water (or buffer) on top of the SLBs is indicated in blue. We define thickness as the Gaussian FWHM around the center of mass of the sigmoidal peaks. The thickness of each leaflet is separately indicated. The overall thickening of the SLB due to G_{M1} incorporation is 11 Å. By separate comparison of the thicknesses of the distal leaflets only before ($\sim$ 25 Å) and after ($\sim$ 33 Å) G_{M1} incorporation, we find that G_{M1} extends $\sim$ 8 Å from the membrane surface.

Figure 4.

No measurable changes in the reflectivity of SOPC/G_{M1} SLBs before (*top*) and after (*bottom*) incubation of CTB. The lines connecting the data points are drawn for clarity of presentation and do not represent a fit to the data.

Figure 5.

Normalized X-ray reflectivity of SLBs with compositions of 15/65/20 mol % (*LD*) and 29/6/65 mol % (*LO*) cholesterol/DOPC/bSM. Solid lines represent fits to the data.

Figure 6.

Electron density profiles of samples (*a*) *LD* and (*b*) *LO*. The sketches represent the molar compositions of cholesterol (*gray*), DOPC (*red*) and bSM (*green*) in the *LD* and *LO* bilayers and illustrate the differences in bilayer condensation and thickness. The gray lines represent the average electron density of the acyl chains, 0.28 $e^-/Å^3$ for the *LD* bilayer (*solid line*) and 0.33 $e^-/Å^3$ for the *LO* bilayer (*dotted line*). These values define thresholds for the state of the SLB (non-condensed and condensed, respectively), according to the empirical definition in the text.

Figure 7.

Normalized reflectivity of cholesterol/DOPC/bSM SLBs with equimolar composition of DOPC and bSM, before (a) and after (b) G_{M1} incorporation. Solid lines represent fits to the data.

Figure 8.

Electron density profiles of cholesterol/DOPC/bSM SLBs with equimolar composition of DOPC and bSM, before (a) and after (b) G_{M1} incorporation. The electron density axis is correct for *20chol* and *20chol+G_{M1}*; the profiles *30chol*, *30chol+G_{M1}* and *40chol*, *40chol+G_{M1}* are shifted for clarity. The lines indicate the lower (*solid lines*) and upper (*dotted lines*) threshold values for the electron density of the acyl chains, as defined in the text and illustrated in Fig. 6. The intermediate region between the lower value (0.28 $e^-/Å^3$, non-condensed) and the upper value (0.33 $e^-/Å^3$, condensed) is shaded for clarity of presentation.

Figure 9.

Fluorescence micrographs of cholesterol/DOPC/bSM SLBs. (*a*): Before G_{M1} addition, sample *20chol* shows uniform fluorescence. (*b*): Dark spots appear after 4 h incubation with excess G_{M1}. Sample *20chol+G_{M1}* shows gray and black domains at room temperature (25°C). (*c*): Upon increasing the temperature to 40°C, the gray domains vanish and the dark domains remain unchanged. (*d*): Close-up micrographs: The white circle is a guide to the eye and highlights a pinned gray domain. The temperature cycle (25°C→ 40°C→ 30°C) shows the gray domains reappearing at their former positions upon recooling.

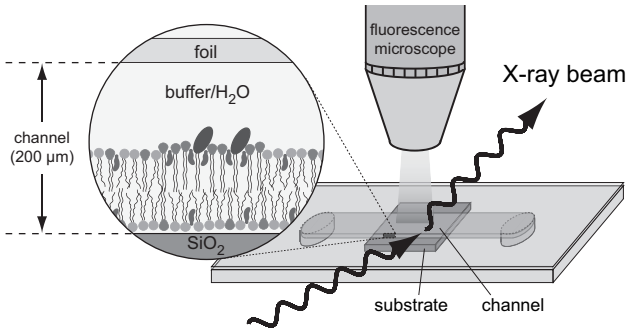
fluorescence
microscope
X-ray beam
foil
buffer/H_2O
channel
(200 µm)
SiO_2
substrate
channel

Figure 1:

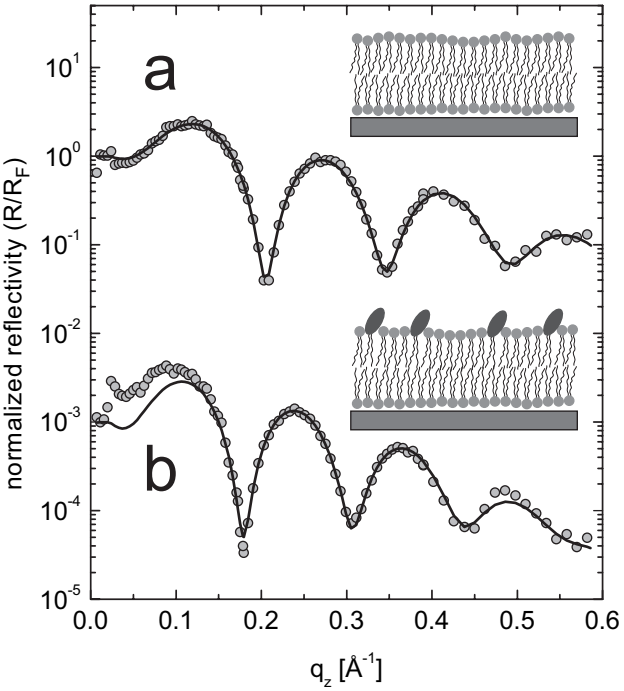
a
b
normalized reflectivity (R/R$_F$)
10^1
10^0
10^{-1}
10^{-2}
10^{-3}
10^{-4}
10^{-5}
0.0
0.1
0.2
0.3
0.4
0.5
0.6
q$_z$ [Å^{-1}]

Figure 2:

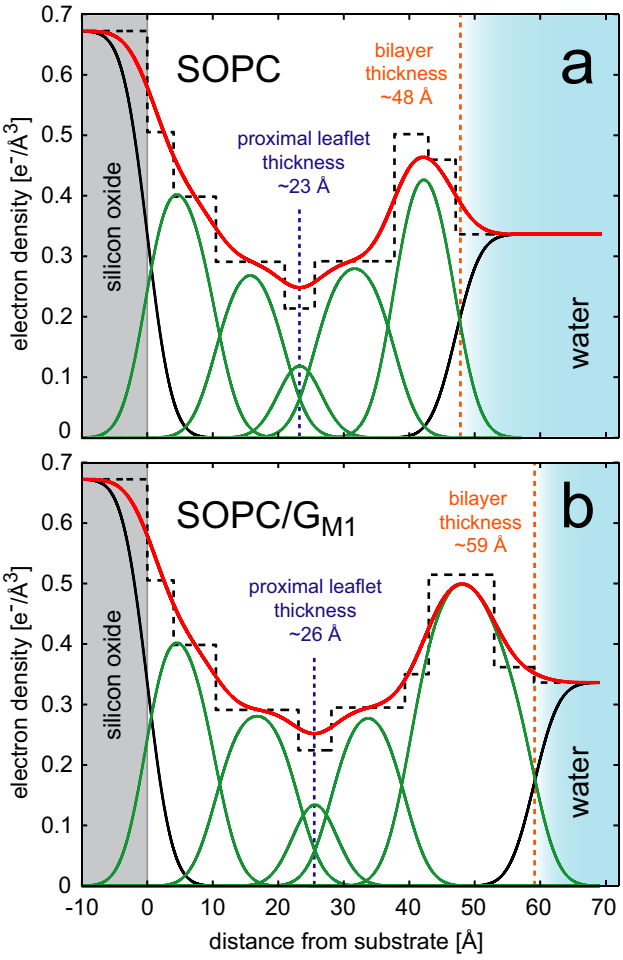
SOPC
bilayer thickness ~48 Å
proximal leaflet thickness ~23 Å
a
silicon oxide
water
electron density [e⁻/Å³]
SOPC/G_M1
bilayer thickness ~59 Å
proximal leaflet thickness ~26 Å
b
distance from substrate [Å]

Figure 3:

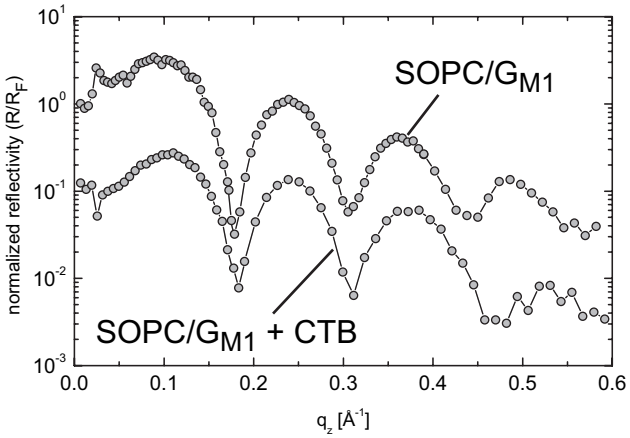
normalized reflectivity (R/R$_F$)
10^1
10^0
10^{-1}
10^{-2}
10^{-3}
0.0
0.1
0.2
0.3
0.4
0.5
0.6
q$_z$ [Å^{-1}]
SOPC/G$_{M1}$
SOPC/G$_{M1}$ + CTB

Figure 4:

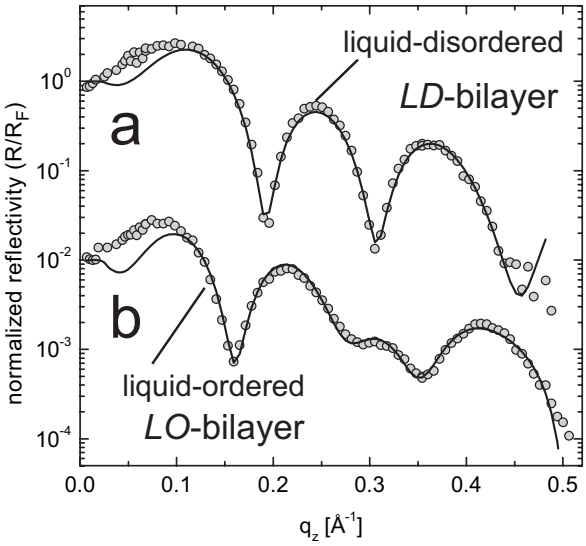
liquid-disordered
LD-bilayer
a
b
liquid-ordered
LO-bilayer
normalized reflectivity (R/R$_F$)
10^0
10^{-1}
10^{-2}
10^{-3}
10^{-4}
0.0
0.1
0.2
0.3
0.4
0.5
q$_z$ [Å^{-1}]

Figure 5:

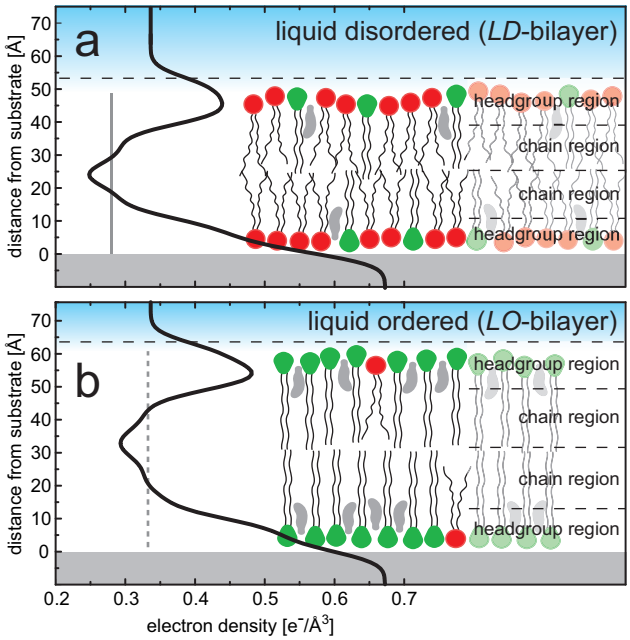
a
liquid disordered (LD-bilayer)
headgroup region
chain region
chain region
headgroup region
b
liquid ordered (LO-bilayer)
headgroup region
chain region
chain region
headgroup region
distance from substrate [Å]
0
10
20
30
40
50
60
70
0.2
0.3
0.4
0.5
0.6
0.7
electron density [e⁻/Å³]

Figure 6:

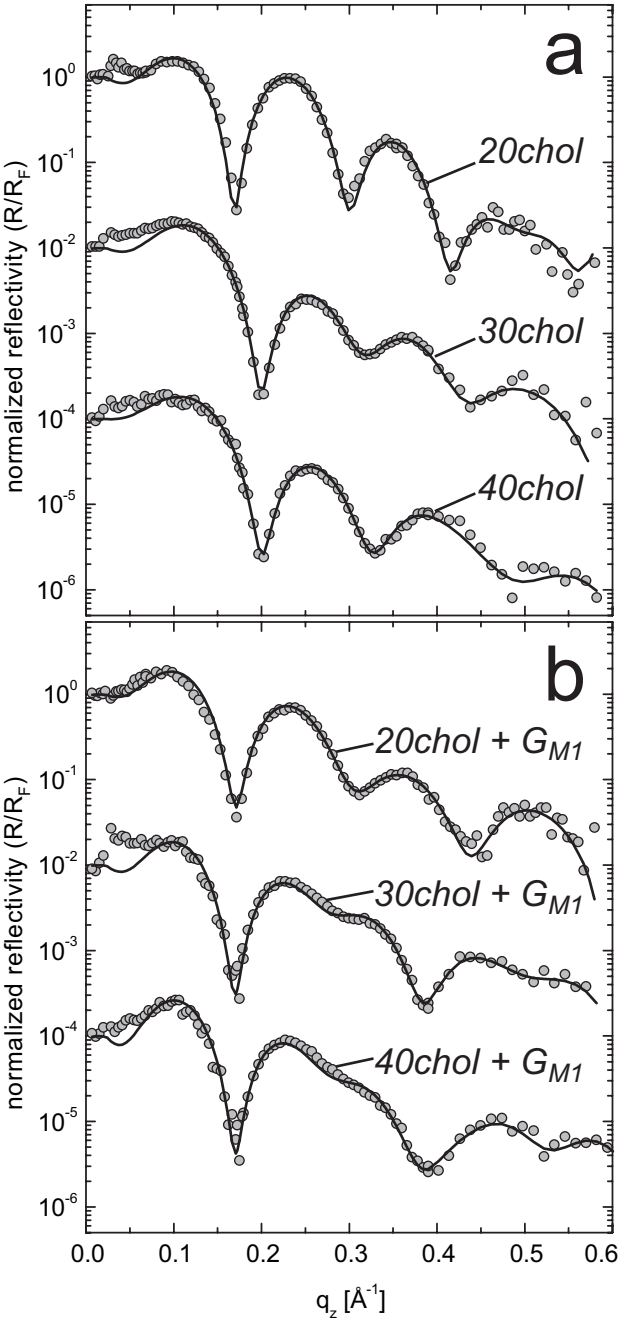
a
20chol
30chol
40chol
b
20chol + G_{M1}
30chol + G_{M1}
40chol + G_{M1}
normalized reflectivity (R/R_F)
10^{0}
10^{-1}
10^{-2}
10^{-3}
10^{-4}
10^{-5}
10^{-6}
0.0
0.1
0.2
0.3
0.4
0.5
0.6
q_z [Å^{-1}]

Figure 7:

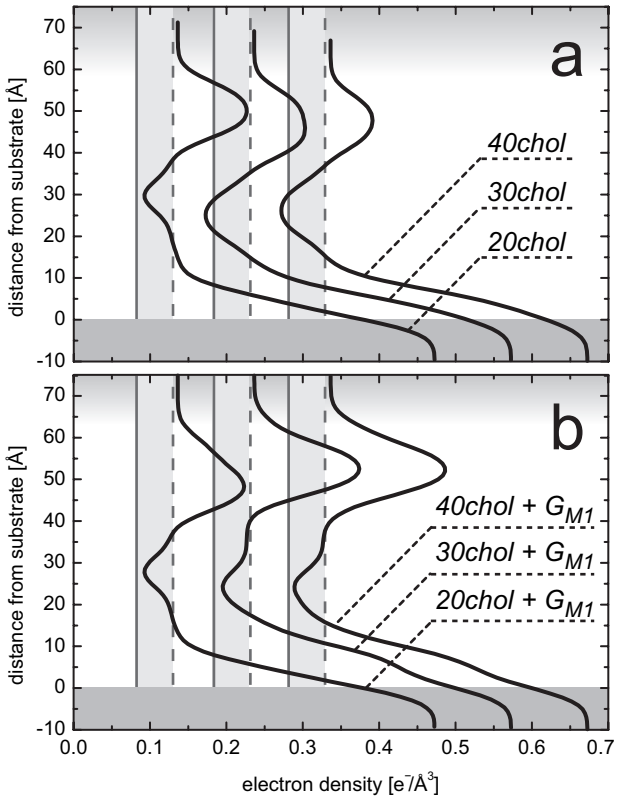
a
40chol
30chol
20chol
b
40chol + G_M1
30chol + G_M1
20chol + G_M1
distance from substrate [Å]
electron density [e⁻/Å³]
70
60
50
40
30
20
10
0
-10
0.0
0.1
0.2
0.3
0.4
0.5
0.6
0.7

Figure 8:

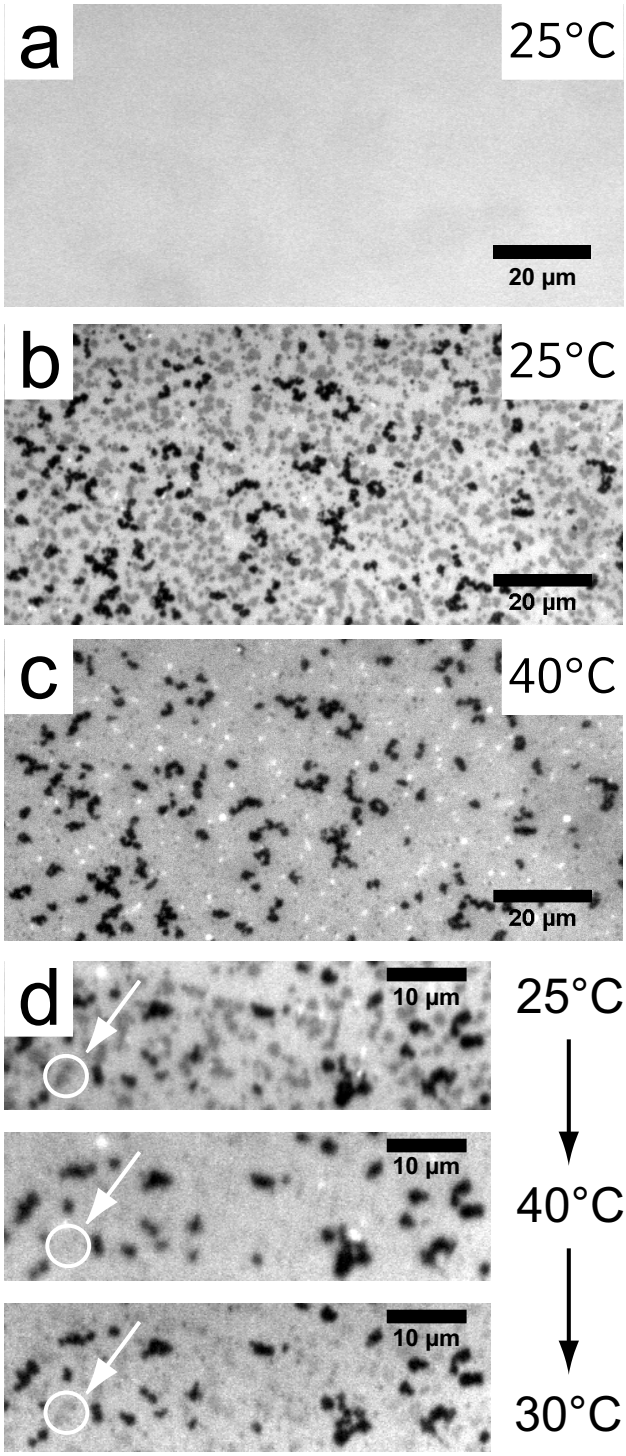

Figure 9:

Appendix B

Continuous bleaching: Data evaluation and program description

A program for analyzing and fitting of continuous bleaching data was written using MatLab v7.1 (Mathworks, Cambridge, MA). The theoretical basis for continuous bleaching was first established in Ref. [13]; detailed guidelines on experimental premises and how to collect continuous bleaching data are given in Ref. [2] and Ref. [4]. The program requires the following toolboxes:

- Optimization
- Image processing

and consists of the files

- cb.m, cb_2.m, cb_3.m
- cb.fig, cb_2.fig, cb_3.fig
- cbexp.m, cbcosh.m, cbbessel.m

The program is initialized by executing the command 'cb' in the MatLab console. This opens the graphical user interface in the figure file 'cb.fig'; the corresponding functions are defined in the procedure file 'cb.m'. Three subsequent panels guide the user through the steps for analyzing the data. In panel 1 (Fig. B.2), a single image can be loaded into the workspace and is displayed in a separate image window (Fig. B.1). Four elements are present in the image window. The blue line allows to choose a line profile in the image which represents the monoexponential decay of the fluorescence intensity at the rim (described by equation 3 in Ref. [4]). It should be chosen to span across the center, from one side of the illuminated area to the other, and should not protrude into the dark region. The yellow line should be chosen to represent the intensity decay at the rim of the illuminated spot (equation 3 in Ref. [13]). Two boxes allow to choose representative areas in the

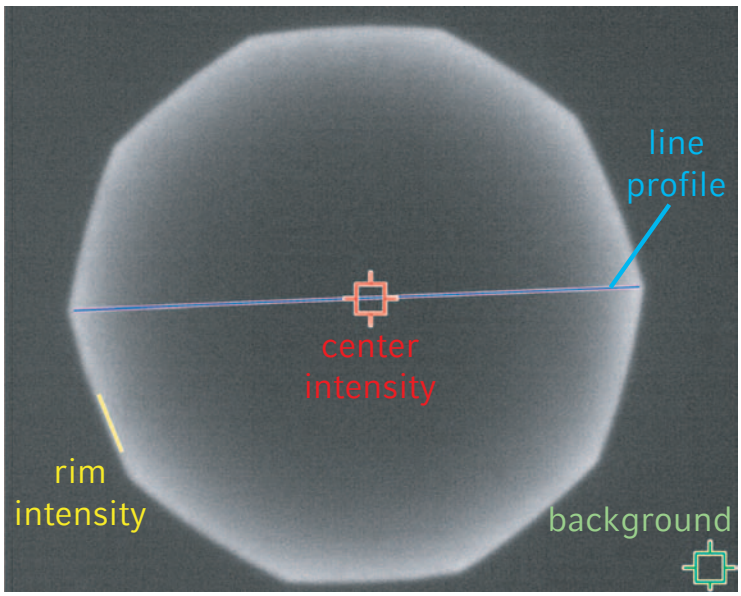

Figure B.1: Image window.

image for extraction of the background (green box) and the fluorescence intensity in the center of the bleached spot (red box).
The image data are extracted by pushing the 'Update' button in panel 1. The line profiles in the image are plotted into the axes of panel 1. A scale factor can be defined to convert properly pixels to μm and a switch allows to toggle between plotting either the blue line (default) or the yellow line. The values for background and center intensity are obtained by averaging the pixel values within the green and the red box, respectively. The size of the boxes can be defined in pixel units (default: 50×50 pixels).
In order to check whether the blue profile accurately shows a monoexponential decay, the blue profile can be simulated and fitted according to the equation

$$Y = b + a \cdot \cosh\left[(X - c)/l\right]. \tag{B.1}$$

This equation is equivalent to equation 3 in Ref. [4]. Start values for the simulation (magenta line) and fit (black line) should be selected within a reasonable range. The fit is performed using least-squares optimization. Fig. B.1 and B.2 show examples for a proper choice of a blue line profile.
Once satisfying line profiles and regions for background and center intensity are chosen, the whole image series can be processed as a batch. Pushing the button 'Extract' loads each image of the bleach series in the current directory into the workspace and extracts the line profiles and green and red box values. The syntax for the filenames must be '...123.TIF' and the first image filename must start with '...000.TIF'. Loading a large number of images may take some time. After the

data are extracted, pushing the button 'Go to next panel' proceeds to panel 2.
Panel 2 allows to extract the bleach rate B, either from the time-dependent intensity decay in the center of the image (upper axes) or from the time-dependent intensity decay at the rim (lower axes). The time lapse interval which was chosen in the continuous bleaching experiment has to be specified in order to properly display the time axis. The bleach rate can be calculate by fitting the exponential equation

$$Y = A \cdot \exp(-B \cdot t) \tag{B.2}$$

to the data in the upper axes, which represents the intensity in the center of the illuminated spot subtracted by the background intensity (red box - green box). Equation B.2 is equivalent to equation 2 in Ref. [4].
The bleach rate B can also be extracted from the time-dependent intensity decay at the rim, according to equation 3 in Ref. [13]. The data are corrected for background and fitted to the equation

$$Y = A \cdot \exp(-B \cdot t/2) \cdot I_0(B \cdot t/2) \tag{B.3}$$

where I_0 is the zeroth modified Bessel function of the first kind.
In panel 3, a selection of the extracted blue line profiles is plotted in the upper axes. For clarity of data presentation, a value can be specified which determines how many profiles are plotted at a time. A value of '1' plots every profile; a value of 20 plots only profiles with index 1, 21, 41, and so on. The 'Fit' button calls a batch procedure which fits all profiles to equation B.1 using least-squares minimization. The batch procedure starts with the last profile index (*n*, here: *n*=241) and uses the predefined parameters imported from panel 1 as start values for the fit. After fitting the *n*-th profile, the fit results for parameters a, l, b, c are taken as start values for fitting the profile *n*-1. This ensures that the fit does not diverge for small *n*, where the exponential decay at the rim is less pronounced. A diffusion coefficient D is extracted for each profile from the exponent $l = \sqrt{B/D}$ and plotted in the lower axes. Since equation B.1 is only applicable for $B \cdot t > 4$, the values for D at small times are usually not accurate [13]. Thus, boundary values for t can be set and the average diffusion coefficient is calculated within this region. The error is indicated as standard deviation.

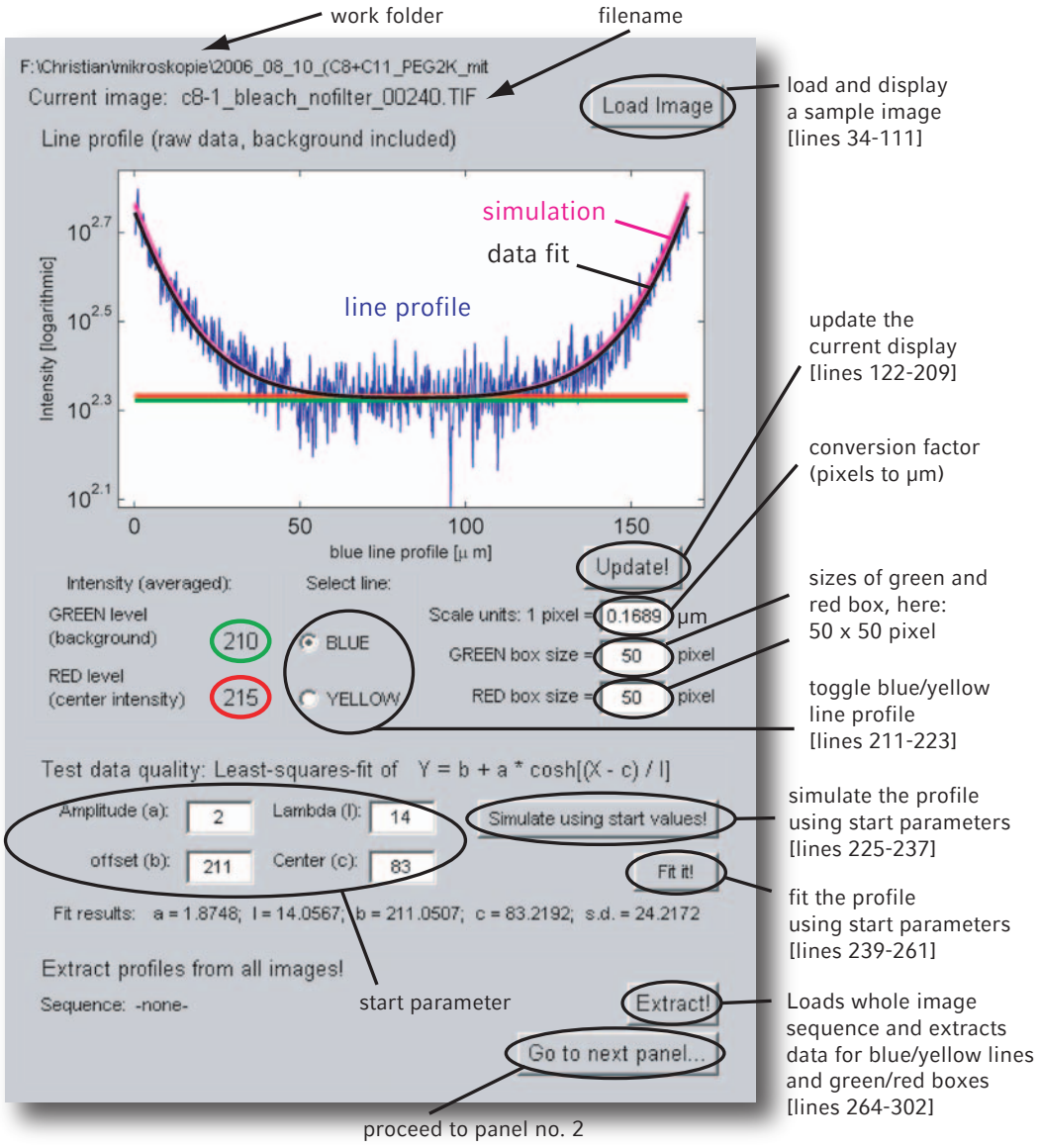

Figure B.2: This is the start interface (panel 1), stored in the figure file 'cb.fig'. Pushing a button calls the corresponding function in the MatLab procedure file 'cb.m'. The source code lines where the function is defined are indicated in brackets. For example, the 'Load image' button executes the source code lines [34-111] in the procedure file.

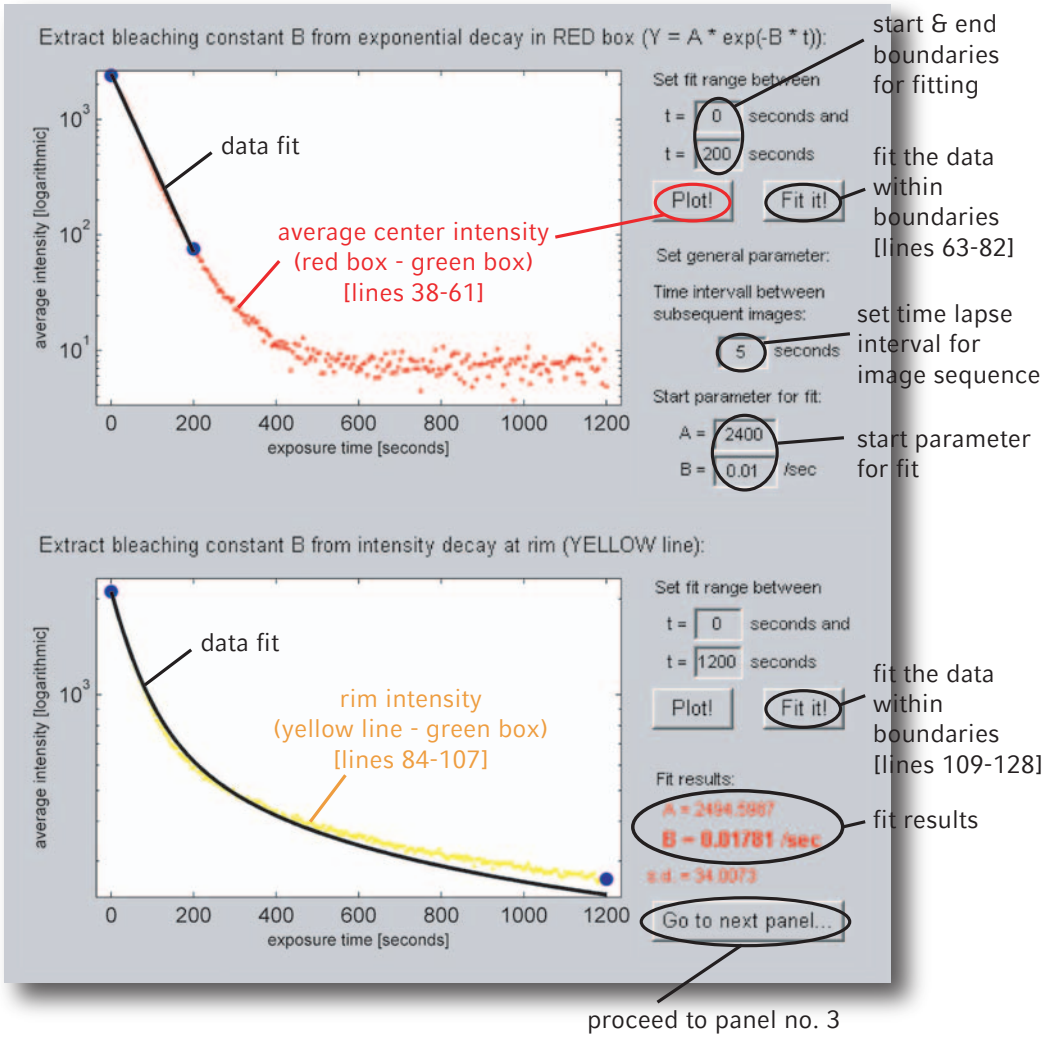

Figure B.3: Panel 2. This interface is called from within panel 1 and offers two independent possibilities for calculating the bleach rate B. The name of the figure file is 'cb_2.fig' and the procedure file is 'cb_2.m'.

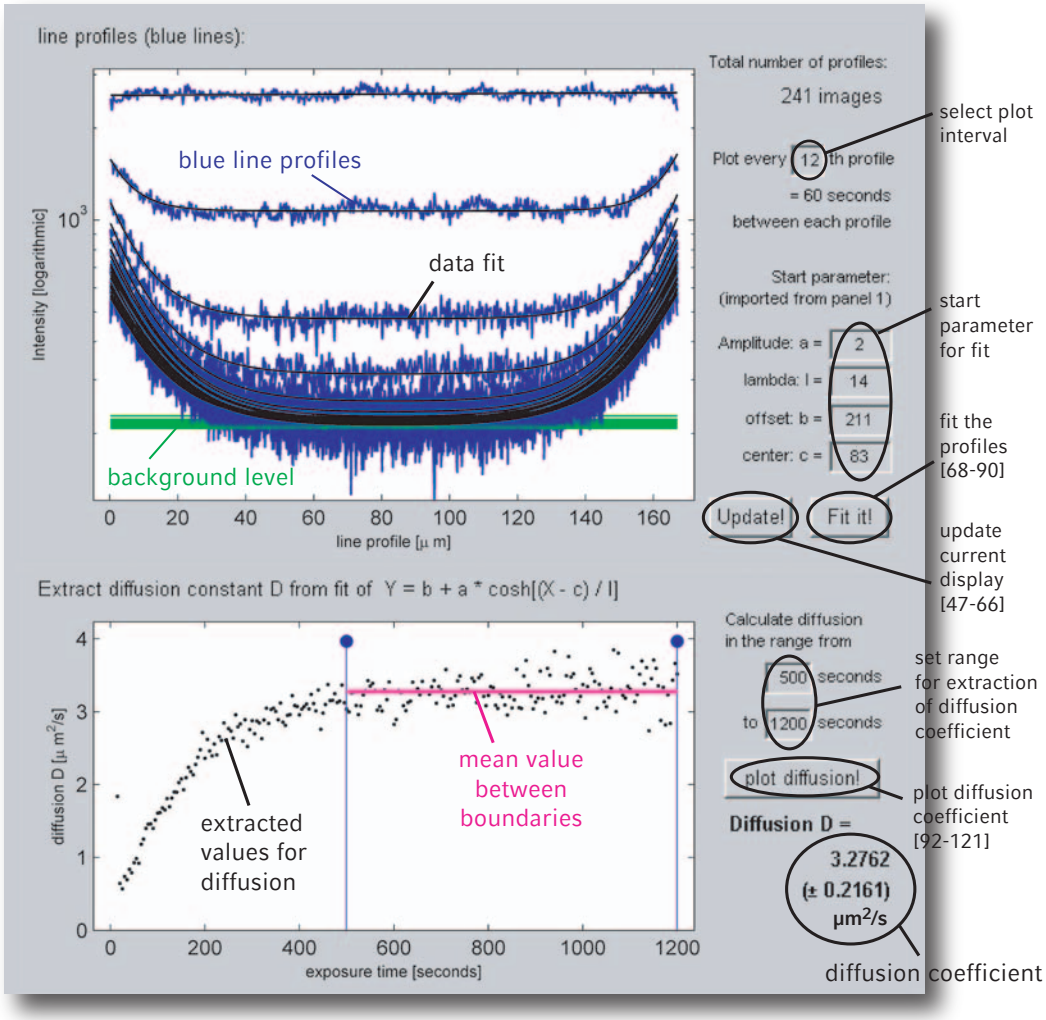

Figure B.4: Panel 3. This interface is called from within panel 2 and fits a series of line profiles. The diffusion coefficient D is subsequently extracted from the fit results. The name of the figure file is 'cb_3.fig' and the procedure file is 'cb_3.m'.

Bibliography

1. C. Reich, M. B. Hochrein, B. Krause, and B. Nickel. A microfluidic setup for studies of solid-liquid interfaces using x-ray reflectivity and fluorescence microscopy. *Rev. Sci. Instrum.*, 76(9):095103, 2005.

2. M. B. Hochrein, C. Reich, B. Krause, J. O. Rädler, and B. Nickel. Structure and mobility of lipid membranes on a thermoplastic substrate. *Langmuir*, 22 (2):538–545, 2006.

3. C. Reich, P. A. Neff, A. R. Bausch, J. O. Rädler, and B. Nickel. Supported membranes on polyelectrolyte layers studied by X-ray reflectometry. *physica status solidi (a)*, 203(14):3463–3467, 2006.

4. M. R. Horton, C. Reich, A. P. Gast, J. O. Rädler, and B. Nickel. Structure and dynamics of crystalline protein layers bound to supported lipid bilayers. *Langmuir*, 23(11):6263–6269, 2007.

5. C. Reich, M. R. Horton, B. Krause, A. P. Gast, J. O. Rädler, and B. Nickel. Condensation, stretching and asymmetry: GM1 and cholesterol in single supported lipid bilayers. *submitted*, May 2007.

6. S. J. Singer and G. L. Nicolson. The fluid mosaic model of the structure of cell membranes. *Science*, 175(23):720–31, 1972.

7. H. Sprong, P. van der Sluijs, and G. van Meer. How proteins move lipids and lipids move proteins. *Nat. Rev. Mol. Cell Biol.*, 2(7):504–513, 2001.

8. B. Alberts, A. Johnson, J. Lewis, M. Raff, K. Roberts, and P. Walter. *Molecular Biology of the Cell, 4th edition*. New York: Garland, 2002.

9. E. Sackmann. Supported Membranes: Scientific and Practical Applications. *Science*, 271:43–48, 1996.

10. I. Reviakine and A. Brisson. Formation of Supported Phospholipid Bilayers from Unilamellar Vesicles Investigated by Atomic Force Microscopy. *Langmuir*, 16(4):1806–1815, 2000.

11. R. P. Richter and A. Brisson. Characterization of lipid bilayers and protein assemblies supported on rough surfaces by atomic force microscopy. *Langmuir*, 19(5):1632–1640, 2003.

12. D. Axelrod, D. E. Koppel, J. Schlessinger, E. Elson, and W. W. Webb. Mobility Measurement by Analysis of Fluorescence Photobleaching Recovery Kinetics. *Biophys. J.*, 16:1055, 1976.

13. C. Dietrich, R. Merkel, and R. Tampé. Diffusion Measurement of Fluorescence-Labeled Amphiphilic Molecules with a Standard Fluorescence Microscope. *Biophys. J.*, 72:1701–1710, 1997.

14. T. Salditt. Thermal fluctuations and stability of solid-supported lipid membranes. *J. Phys.: Condens. Matter*, 17:R287–R314, 2005.

15. S. Krueger. Neutron reflection from interfaces with biological and biomimetic materials. *Curr. Opin. Colloid Interface Sci.*, 6:111–117, 2001.

16. R. K. Thomas. Neutron Reflection From Liquid Interfaces. *Annual Review of Physical Chemistry*, 55(1):391–426, 2004.

17. T. Baumgart, A. T. Hammond, P. Sengupta, S. T. Hess, D. A. Holowka, B. A. Baird, and W. W. Webb. Large-scale fluid/fluid phase separation of proteins and lipids in giant plasma membrane vesicles. *Proc. Natl. Acad. Sci. USA*, 104(9):3165–3170, 2007.

18. P. A. Janmey and P. K. J. Kinnunen. Biophysical properties of lipids and dynamic membranes. *Trends Cell Biol.*, 16(10):538–546, 2006.

19. K. Simons and E. Ikonen. Functional rafts in cell membranes. *Nature*, 387: 569–572, 1997.

20. D. A. Brown and E. London. Structure and Function of Sphingolipid- and Cholesterol-rich Membrane Rafts. *J. Biol. Chem.*, 275(23):17221–17224, 2000.

21. K. Simons and E. Ikonen. How Cells Handle Cholesterol. *Science*, 290(5497): 1721–1726, 2000.

22. F. R. Maxfield and I. Tabas. Role of cholesterol and lipid organization in disease. *Nature*, 438:612–621, 2005.

23. R. G. W. Anderson and K. Jacobson. A role for lipid shells in targeting proteins to caveolae, rafts, and other lipid domains. *Science*, 296:1821–1825, 2002.

24. B. Antonny. Membrane deformation by protein coats. *Curr. Opin. Cell. Biol.*, 18(4):386–394, 2006.

25. G. Khanarian. Optical properties of cyclic olefin copolymers. *Opt. Eng.*, 40 (6):1024–1029, 2001.

26. L. G. Parratt. Surface Studies of Solids by Total Reflection of X-rays. *Phys. Rev.*, 95(2):359, July 1954.

27. L. Névot and P. Croce. Characterization of surfaces by grazing x-ray reflection - Application to study of polishing of some silicate-glasses. *Revue de physique appliquée*, 15:761, 1980.

28. J. Als-Nielsen and D. McMorrow. *Elements of Modern X-ray Physics*. Wiley & Sons, Ltd., 2001.

29. B. L. Henke, E. M. Gullikson, and J. C. Davis. X-ray interactions: Photoabsorption, scattering, transmission, and reflection at E = 50-30,000 eV, Z = 1-92. *Atomic Data and Nuclear Data Tables*, 54(2):181–342, 1993.

30. M. Przybylo, J. Sykora, J. Humpolickova, A. Benda, A. Zan, and M. Hof. Lipid diffusion in giant unilamellar vesicles is more than 2 times faster than in supported phospholipid bilayers under identical conditions. *Langmuir*, 22(22): 9096–9099, 2006.

31. F. M. Menger, M. E. Chlebowski, A. L. Galloway, H. Lu, V. A. Seredyuk, J. L. Sorrells, and H. Zhang. A tribute to the phospholipid. *Langmuir*, 21(23): 10336–10341, 2005.

32. W. H. Binder, V. Barragan, and F. M. Menger. Domains and rafts in lipid membranes. *Angew. Chem. Int. Ed*, 42:5802–5827, 2003.

33. E. Kalb, S. Frey, and L. K. Tamm. Formation of supported planar bilayers by fusion of vesicles to supported phospholipid monolayers. *Biochim. Biophys. Acta*, 1103:307–316, 1992.

34. A. A. Brian and H. M. McConnell. Allogeneic stimulation of cytotoxic T cells by supported planar membranes. *Proc. Natl. Acad. Sci.*, 81:6159–6163, October 1984.

35. L. K. Tamm and H. M. McConnell. Supported phospholipid bilayers. *Biophys. J.*, 47(1):105–113, January 1985.

36. H. M. McConnell, T. H. Watts, R. M. Weis, and A. A. Brian. Supported planar membranes in studies of cell-cell recognition in the immune system. *Biochim. Biophys. Acta (BBA) - Reviews on Biomembranes*, 864(1):95–106, 1986.

37. U. Mennicke and T. Salditt. Preparation of solid-supported lipid bilayers by spin-coating. *Langmuir*, 18(21):8172–8177, 2002.

38. A. C. Simonsen and L. A. Bagatolli. Structure of spin-coated lipid films and domain formation in supported membranes formed by hydration. *Langmuir*, 20(22):9720–9728, 2004.

39. E. Reimhult, F. Hook, and B. Kasemo. Intact vesicle adsorption and supported biomembrane formation from vesicles in solution: Influence of surface chemistry, vesicle size, temperature, and osmotic pressure. *Langmuir*, 19(5): 1681–1691, 2003.

40. H. Schönherr, J. M. Johnson, P. Lenz, C. W. Frank, and S. G. Boxer. Vesicle Adsorption and Lipid Bilayer Formation on Glass Studied by Atomic Force Microscopy. *Langmuir*, 20(26):11600–11606, 2004.

41. R. P. Richter, R. Berat, and A. R. Brisson. Formation of Solid-Supported Lipid Bilayers: An Integrated View. *Langmuir*, 22(8):3497–3505, 2006.

42. C. Hamai, P. S. Cremer, and S. M. Musser. Single Giant Vesicle Rupture Events Reveal Multiple Mechanisms of Glass-Supported Bilayer Formation. *Biophys. J.*, 92(6):1988–1999, 2007.

43. U. Seifert. Configurations of fluid membranes and vesicles. *Advances in Physics*, 46(1):13–137, 1997.

44. A. Spaar and T. Salditt. Short range of hydrocarbon chains in fluid phospholipid bilayers studied by x-ray diffractions from highly oriented membranes. *Biophys. J.*, 85:1576–1584, 2003.

45. M. R. Horton, J. O. Rädler, and A. P. Gast. Phase behavior and the partitioning of caveolin-1 scaffolding domain peptides in model lipid bilayers. *J. Colloid Interface Sci.*, 304(1):67–76, 2006.

46. L. A. Bagatolli. To see or not to see: Lateral organization of biological membranes and fluorescence microscopy. *Biochim. Biophys. Acta (BBA) - Biomembranes*, 1758(10):1541–1556, 2006.

47. S. L. Veatch and S. L. Keller. Miscibility phase diagrams of giant vesicles containing sphingomyelin. *Phys. Rev. Lett.*, 94:148101, 2005.

48. E. Evans and E. Sackmann. Translational and rotational drag coefficients for a disk moving in a liquid membrane-associated with a rigid substrate. *Journal of Fluid Mechanics*, 194:553–561, 1988.

49. J. Rädler, H. Strey, and E. Sackmann. Phenomenology and Kinetics of Lipid Bilayer Spreading on Hydrophilic Surfaces. *Langmuir*, 11:4539–4548, 1995.

50. P. S. Cremer and S. G. Boxer. Formation and spreading of lipid bilayers on planar glass supports. *Journal of Physical Chemistry B*, 103(13):2554–2559, 1999.

51. S. Chiantia, J. Ries, N. Kahya, and P. Schwille. Combined AFM and Two-Focus SFCS Study of Raft-Exhibiting Model Membranes. *ChemPhysChem*, 7 (11):2409–2418, 2006.

52. P. Lenz, C. M. Ajo-Franklin, and S. G. Boxer. Patterned supported lipid bilayers and monolayers on poly(dimethylsiloxane). *Langmuir*, 20(25):11092–11099, 2004.

53. T. Nielsen, F. Bundgaard, P. Shi, P. Szabo, O. Geschke, and A. Kristensen. Nanoimprint lithography in the cyclic olefin, Topas, a highly UV-transparent and chemically resistant thermoplast. *Journal of vacuum Science and Technology B*, 22:1770–1775, 2004.

54. M. B. Hochrein, J. A. Leierseder, L. Golubovic, and J. O. Rädler. DNA Localization and Stretching on Periodically Microstructured Lipid Membranes. *Phys. Rev. Lett.*, 96(3):038103, 2006.

55. Y. Liu and J. F. Nagle. Diffuse scattering provides material parameters and electron density profiles of biomembranes. *Phys. Rev. E*, 69:040901, 2004.

56. G. Decher. Fuzzy Nanoassemblies: Toward Layered Polymeric Multicomposites. *Science*, 277:1232–1237, 1997.

57. P. A. Neff, A. Naji, C. Ecker, B. Nickel, R. v. Klitzing, and A. R. Bausch. Electrical detection of self-assembled polyelectrolyte multilayers by a thin film resistor. *Macromolecules*, 39(2):463–466, 2006.

58. P. A. Neff, B. K. Wunderlich, R. v. Klitzing, and A. R. Bausch. Formation and dielectric properties of polyelectrolyte multilayers studied by a silicon-on-insulator based thin film resistor. *Langmuir*, 23(7):4048–4052, 2007.

59. A. Plech, T. Salditt, C. Münster, and J. Peisl. Investigation of Structure and Growth of Self-Assembled Polyelectrolyte Layers by X-ray and Neutron Scattering under Grazing Angles. *J. Colloid Interface Sci.*, 223:74–82, 2000.

60. A. R. Sapuri, M. M. Baksh, and J. T. Groves. Electrostatically Targeted Intermembrane Lipid Exchange with Micropatterned Supported Membranes. *Langmuir*, 19:1606–1610, 2003.

61. O. G. Mouritsen, T. L. Andresen, A. Halperin, P. L. Hansen, A. F. Jakobsen, U. B. Jensen, M. Ø Jensen, K. Jørgensen, T. Kaasgaard, C. Leidy, A. C. Simonsen, G. H. Peters, and M. Weiss. Activation of interfacial enzymes at

membrane surfaces. *Journal of Physics: Condensed Matter*, 18(28):S1293–S1304, 2006.

62. V. M. Kaganer, H. Möhwald, and P. Dutta. Structure and phase transitions in Langmuir monolayers. *Reviews of Modern Physics*, 71(3):779–819, 1999.

63. C. E. Miller, J. Majewski, R. Faller, S. Satija, and T. L. Kuhl. Cholera Toxin Assault on Lipid Monolayers Containing Ganglioside GM1. *Biophys. J.*, 86(6): 3700–3708, 2004.

64. D. Vaknin, K. Kjaer, H. Ringsdorf, R. Blankenburg, M. Piepenstock, A. Diederich, and M. Loesche. X-ray and neutron reflectivity studies of a protein monolayer adsorbed to a functionalized aqueous surface. *Langmuir*, 9 (5):1171–1174, 1993.

65. P. Ratanabanangkoon, M. Gropper, R. Merkel, E. Sackmann, and A. P. Gast. Two-dimensional streptavidin crystals on giant lipid bilayer vesicles. *Langmuir*, 18:4270–4276, 2002.

66. T. L. Calvert and D. Leckband. Two-dimensional protein crystallization at solid-liquid interfaces. *Langmuir*, 13(25):6737–6745, 1997.

67. P. Ratanabanangkoon and A.P. Gast. Effect of ionic strength on two-dimensional streptavidin crystallization. *Langmuir*, 19(5):1794–1801, 2003.

68. Andrew C. Ku, Seth A. Darst, Roger D. Kornberg, Channing R. Robertson, and Alice P. Gast. Dendritic growth of two-dimensional protein crystals. *Langmuir*, 8(10):2357–2360, 1992.

69. C. Rosano, P. Arosio, and M. Bolognesi. The x-ray three-dimensional structure of avidin. *Biomolecular Engineering*, 16:5–12, 1999.

70. Th. M. Nieuwenhuizen, P. F. J. van Velthoven, and M. H. Ernst. Diffusion and long-time tails in a two-dimensional site-percolation model. *Phys. Rev. Lett.*, 57(20):2477–2480, Nov 1986.

71. M. J. Saxton. Anomalous diffusion due to obstacles: a Monte Carlo study. *Biophys. J.*, 66:394–401, 1994.

72. W. I. Lencer, T. R. Hirst, and R. K. Holmes. Membrane traffic and the cellular uptake of cholera toxin. *Biochim. Biophys. Acta (BBA) - Molecular Cell Research*, 1450(3):177–190, July 1999.

73. K. C. Weng, J. L. Kanter, W. H. Robinson, and C. W. Frank. Fluid supported lipid bilayers containing monosialoganglioside GM1: A QCM-D and FRAP study. *Colloids Surf. B. Biointerfaces*, 50(1):76–84, 2006.

74. R. Wang, J. Shi, A. N. Parikh, A. P. Shreve, L. Chen, and B. I. Swanson. Evidence for cholera aggregation on GM_1-decorated lipid bilayers. *Colloids Surf. B. Biointerfaces*, 33:45–51, 2004.

75. T. J. McIntosh and S. A. Simon. Long- and Short-Range Interactions between Phospholipid/Ganglioside GM1 Bilayers. *Biochemistry*, 33(34):10477–10486, 1994.

76. S. L. Veatch, I. V. Polozov, K. Gawrisch, and S. L. Keller. Liquid Domains in Vesicles Investigated by NMR and Fluorescence Microscopy. *Biophys. J.*, 86 (5):2910–2922, 2004.

77. A. T. Hammond, F. A. Heberle, T. Baumgart, D. Holowka, B. Baird, and G. W. Feigenson. Crosslinking a lipid raft component triggers liquid ordered-liquid disordered phase separation in model plasma membranes. *Proc. Natl. Acad. Sci. USA*, 102(18):6320–6325, 2005.

78. C. Dietrich, L. A. Bagatolli, Z. N. Volovyk, N. L. Thompson, M. Levi, K. Jacobson, and E. Gratton. Lipid rafts reconstituted in model membranes. *Biophys. J.*, 80:1417–1428, 2001.

Danksagung

Ich danke **Joachim O. Rädler** für die herzliche Aufnahme an seinem Institut und für die Bereitstellung eines Arbeitsumfeldes mit einer sehr guten Infrastruktur, ohne die diese Doktorarbeit nicht möglich gewesen wäre. Die Vielfältigkeit der Projekte am Lehrstuhl Rädler haben mir stets einen Überblick weit über den Horizont meiner eigenen Arbeit hinaus ermöglicht. **Bert Nickel** danke ich für die hervorragende Betreuung meiner Dissertation. Seine stets positive und pragmatische Herangehensweise an neue Frage- und Problemstellungen hat so manches Projekt meiner Doktorarbeit aus vermeintlichen Sackgassen erfolgreich herausgeführt.
Meinen Kollegen **Margaret Horton, Marion Hochrein, Luisa Andruzzi, Christian Daniel** und **Andreas Hohner** möchte ich ein besonderes Dankeschön aussprechen. Von Ihnen habe ich nicht nur unschätzbar viel über Lipide & Co. gelernt, sondern insbesondere wie man mit viel Ausdauer, Enthusiasmus und kritischem Hinterfragen von scheinbar Offensichtlichem auch gerade die etwas schwierigeren Projekte zum Erfolg führen kann. Ihnen und **Simon Keller, Daniel Hönig, Teresa Eichinger** und **Claudia Schmidt** danke ich für eine sehr angenehme und oftmals lustige Arbeitsatmosphäre am Lehrstuhl. **Bärbel Krause** möchte ich für Ihren unermüdlichen Einsatz bei unseren Synchrotronmessungen an der ESRF danken. Ein herzliches Dankeschön auch an **Gerlinde Schwake** und **Susi Kempter** für ihre grosse Hilfsbereitschaft und ihren Überblick im Labor, und an **Margarete Meixner** für die Unterstützung bei allen administrativen Fragen, sowie **allen anderen netten Leuten** am Lehrstuhl.

Ein ganz besonderer Dank gilt **meiner Familie**. Für Alles.